

Development and validation of parallel three-dimensional computational models of ultrasound propagation and tissue microstructure for preclinical cancer imaging

(Spine title: 3-D computational modeling for preclinical cancer imaging)
(Thesis format: Integrated-Article)

by

Mohammad Ibrahim Daoud

Graduate Program
in
Engineering Science
Electrical and Computer Engineering

Submitted in partial fulfillment
of the requirements for the degree of
Doctor of Philosophy

School of Graduate and Postdoctoral Studies
The University of Western Ontario
London, Ontario, Canada

August 2009

© Mohammad Ibrahim Daoud, 2009



Library and Archives
Canada

Published Heritage
Branch

395 Wellington Street
Ottawa ON K1A 0N4
Canada

Bibliothèque et
Archives Canada

Direction du
Patrimoine de l'édition

395, rue Wellington
Ottawa ON K1A 0N4
Canada

Your file *Votre référence*
ISBN: 978-0-494-54280-4
Our file *Notre référence*
ISBN: 978-0-494-54280-4

NOTICE:

The author has granted a non-exclusive license allowing Library and Archives Canada to reproduce, publish, archive, preserve, conserve, communicate to the public by telecommunication or on the Internet, loan, distribute and sell theses worldwide, for commercial or non-commercial purposes, in microform, paper, electronic and/or any other formats.

The author retains copyright ownership and moral rights in this thesis. Neither the thesis nor substantial extracts from it may be printed or otherwise reproduced without the author's permission.

In compliance with the Canadian Privacy Act some supporting forms may have been removed from this thesis.

While these forms may be included in the document page count, their removal does not represent any loss of content from the thesis.

AVIS:

L'auteur a accordé une licence non exclusive permettant à la Bibliothèque et Archives Canada de reproduire, publier, archiver, sauvegarder, conserver, transmettre au public par télécommunication ou par l'Internet, prêter, distribuer et vendre des thèses partout dans le monde, à des fins commerciales ou autres, sur support microforme, papier, électronique et/ou autres formats.

L'auteur conserve la propriété du droit d'auteur et des droits moraux qui protègent cette thèse. Ni la thèse ni des extraits substantiels de celle-ci ne doivent être imprimés ou autrement reproduits sans son autorisation.

Conformément à la loi canadienne sur la protection de la vie privée, quelques formulaires secondaires ont été enlevés de cette thèse.

Bien que ces formulaires aient inclus dans la pagination, il n'y aura aucun contenu manquant.


Canada

THE UNIVERSITY OF WESTERN ONTARIO
SCHOOL OF GRADUATE AND POSTDOCTORAL STUDIES

CERTIFICATE OF EXAMINATION

Chief Advisor

Dr. James C. Lacefield

Examining Board

Dr. Roy Eagleson

Advisory Committee

Dr. Terry M. Peters

Dr. Michael C. Kolios

Dr. Hanif M. Ladak

Dr. Jagath Samarabandu

Dr. Ian C. MacDonald

The thesis by

Mohammad Ibrahim Daoud

entitled

**Development and validation of parallel three-dimensional computational
models of ultrasound propagation and tissue microstructure for
preclinical cancer imaging**

is accepted in partial fulfillment of the
requirements for the degree of
Doctor of Philosophy

Chair of Examination Board

Dated this 5th day of August, 2009.

Dr. Michael Rieder

Abstract

High-frequency (20-60 MHz) ultrasound images are sensitive to variations in tissue microanatomy that accompany tumour growth, but the relationships between high-frequency ultrasound backscattering and tumour microstructure are incompletely understood. A parallel 3-D ultrasound simulator and a tissue microanatomical model are developed to investigate these relationships. The simulator runs on computer clusters and uses a 3-D formulation of a k -space method to compute wavefront propagation. An allocation algorithm is introduced to divide the computation of each scan line between a group of cluster nodes and employ multiple groups to compute individual lines concurrently. The simulator achieves an error as low as 0.57%. An aperture projection technique is introduced to simulate imaging with a focused transducer using reduced computation grids. This technique is applied to synthesize B-mode images of a tissue-mimicking phantom. The execution time of an image using 20 nodes is 18.6 hours, compared to a serial execution time of 357.5 hours.

The microanatomical model treats tissue as a population of stochastically positioned cells, where each cell is represented as a spherical nucleus surrounded by cytoplasm. The model is employed to represent the microstructure of healthy mouse liver and an experimental liver metastasis that are analyzed using DAPI- and H&E-stained histology specimens digitized at $20\times$ magnification. For each simulated tissue, the spatial organization of cells is controlled by a Gibbs-Markov point process tuned to reproduce the number density and distribution of centre-to-centre spacing of nuclei in the DAPI-stained slides of the corresponding experimental tissue specimen.

The ultrasound simulator is used to synthesize B-mode images of the simulated healthy and tumour tissues. The first-order speckle statistics of the images of each simulated tissue are compared with corresponding experimental images. The simulations show good matching between the images of the simulated healthy tissue and images of healthy liver. Moreover, good matching is achieved between the images of the simulated tumour and matching experimental images when acoustic properties

are used that are different from the values assumed for healthy tissue. These simulations suggest that changes in the first-order speckle statistics that accompany tumour progression are related to variations in tissue acoustic and microstructural properties.

Keywords: high-frequency ultrasound, imaging simulation, tissue microstructure, numerical methods, Gibbs-Markov point process, stereology, parallel computing, parallel speedup and efficiency, ultrasound speckle statistics, small animal imaging, cancer imaging

Acknowledgments

I would like to acknowledge all the people who inspired and encouraged me throughout my doctoral studies at Robarts Research Institute and University of Western Ontario.

I especially would like to thank my supervisor, James Lacefield, for his helpful criticisms, encouragement, and guidance. The door to James' office was always open whenever I had a question about my research.

I am thankful for my advisory committee, Terry Peters and Jagath Samarabandu, for their helpful suggestions and advice throughout the course of this thesis. In particular, I would like to thank Terry for his support and help to resolve some challenges that I faced during my research. Terry is also acknowledged for giving me access to the high-performance computing facilities of his lab.

All my colleagues at the Lacefield lab made my doctoral studies an interesting and exciting experience. Zamir Khan, Stephen Pinter, Ethan Shen, Adam Waspe, and Lauren Wirtzfeld shared with me both fun times and long nights of research. In particular, I am thankful for Stephen, whom I started and completed my studies with. Michael Bygrave is acknowledged for ultrasound scanning assistance.

I would like to thank Jason Townson, Ian MacDonald, and Ann Chambers for access to and preparation of the experimental metastasis models that I used in chapters 3 and 4 of my thesis. Mike Lizardo, Sheri Saunders, Carmen Simedrea, and Lisa MacKenzie are thanked for technical assistance with microscopy.

The simulations reported in this thesis were performed using the computing facilities of the Shared Hierarchical Academic Research Computing Network (SHARCNET) and the Virtual Augmentation and Simulation for Surgery and Therapy (VASST) laboratory. Ge Baolai and Chris Wedlake are acknowledged for technical assistance with using the computing facilities of SHARCNET and VASST, respectively.

I am thankful for the generous support from the funding sources. My studies were

funded by the Canadian Institutes of Health Research (CIHR)/University of Western Ontario Strategic Training Initiative in Cancer Research and Technology Transfer from 2006 to 2007 and Natural Sciences and Engineering Research Council (NSERC) postgraduate scholarship from 2007 to 2009.

My deepest gratitude goes to my family for their constant love and support throughout my life. This thesis is simply impossible without them. I am indebted to my parents, Ibrahim and Hana, my sister, Asma, and my brothers, Omar and Abdelhamid, for their care and love.

Contents

| | |
|--|-------------|
| Certificate of Examination | ii |
| Abstract | iii |
| Acknowledgements | v |
| List of Tables | x |
| List of Figures | xi |
| List of Symbols | xv |
| List of Acronyms & Abbreviations | xvii |
| 1 Introduction | 1 |
| 1.1 Overview | 1 |
| 1.2 The wave equation | 3 |
| 1.3 3-D simulation of ultrasound imaging | 6 |
| 1.4 Parallel Computing | 7 |
| 1.5 Quantifying tissue microstructure | 9 |
| 1.6 High-frequency ultrasound scattering models | 12 |
| 1.7 Hypothesis and objectives | 15 |
| 1.8 Thesis outline | 15 |
| 1.8.1 Chapter 2 | 15 |
| 1.8.2 Chapter 3 | 16 |
| 1.8.3 Chapter 4 | 17 |
| 1.8.4 Chapter 5 | 17 |
| References | 18 |
| 2 Distributed Three-Dimensional Simulation of B-mode Ultrasound Imaging Using a First-Order k-Space Method | 21 |
| 2.1 Introduction | 21 |

| | | |
|-------|--|----|
| 2.2 | Theory | 26 |
| 2.2.1 | 3-D first-order k -space method | 26 |
| 2.2.2 | Relaxation absorption and perfectly matched layers | 28 |
| 2.3 | Parallel implementation | 34 |
| 2.3.1 | Parallel simulation of a single scan line | 34 |
| 2.3.2 | Parallel simulation of multiple scan lines | 36 |
| 2.4 | Numerical methods | 38 |
| 2.4.1 | Analysis of numerical accuracy and computational complexity: Propagation calculations | 40 |
| 2.4.2 | Analysis of numerical accuracy and computational complexity: Attenuation calculations | 41 |
| 2.4.3 | Parallel simulation performance | 43 |
| 2.4.4 | B-mode imaging simulations | 44 |
| 2.4.5 | Computer cluster specifications | 46 |
| 2.5 | Numerical results | 46 |
| 2.5.1 | Analysis of numerical accuracy and computational complexity: Propagation calculations | 46 |
| 2.5.2 | Analysis of numerical accuracy and computational complexity: Attenuation calculations | 48 |
| 2.5.3 | Parallel simulation performance | 50 |
| 2.5.4 | B-mode imaging simulations | 52 |
| 2.6 | Discussion | 52 |
| 2.7 | Conclusion | 56 |
| | References | 57 |

| | | |
|----------|---|-----------|
| 3 | Stochastic Modeling of Normal and Tumour Tissue Microstructure for High-Frequency Ultrasound Imaging Simulations | 61 |
| 3.1 | Introduction | 61 |
| 3.2 | Materials and methods | 64 |
| 3.2.1 | Experimental characterization of tissue microstructure | 64 |
| 3.2.2 | Modeling the spatial arrangement of cells | 68 |
| 3.2.3 | Synthesis of simulated tissue | 70 |
| 3.2.4 | Tuning the model | 71 |
| 3.2.5 | Model scalability for imaging simulations | 73 |
| 3.3 | Results | 73 |
| 3.3.1 | Healthy mouse liver | 73 |
| 3.3.2 | Experimental liver metastasis | 76 |
| 3.4 | Discussion | 81 |
| 3.5 | Conclusion | 86 |
| | References | 88 |

| | | |
|-------------|---|------------|
| 4 | Three-Dimensional Computational Modeling of High-Frequency Ultrasound Imaging of a Mouse Liver Metastasis Model | 92 |
| 4.1 | Introduction | 92 |
| 4.2 | Methods | 97 |
| 4.2.1 | Experimental ultrasound imaging | 97 |
| 4.2.2 | Modeling tissue microstructure | 98 |
| 4.2.3 | Ultrasound imaging simulation | 99 |
| 4.2.4 | B-mode image analysis | 101 |
| 4.3 | Results | 102 |
| 4.3.1 | Healthy mouse liver | 102 |
| 4.3.2 | Experimental liver metastasis | 103 |
| 4.4 | Discussion | 107 |
| 4.5 | Conclusion | 110 |
| | References | 112 |
| 5 | Summary and Future Work | 117 |
| 5.1 | Summary | 117 |
| 5.1.1 | Chapter 2: Distributed three-dimensional simulation of B-mode ultrasound imaging using a first-order k -space method | 117 |
| 5.1.2 | Chapter 3: Stochastic modeling of normal and tumour tissue microstructure for high-frequency ultrasound imaging simulations | 118 |
| 5.1.3 | Chapter 4: Three-dimensional computational modeling of high-frequency ultrasound imaging of a mouse liver metastasis model | 119 |
| 5.2 | Future work | 120 |
| 5.3 | Closing | 122 |
| | References | 124 |
| A | Permissions to Reproduce Published Work | 126 |
| Vita | | 131 |

List of Tables

| | | |
|-----|--|----|
| 2.1 | Relaxation absorption parameters to model frequency-dependent absorption | 42 |
| 2.2 | Speedup values of B-mode image simulations | 52 |

List of Figures

| | | |
|-----|--|----|
| 1.1 | Plane wave propagating in a fluid medium along the x axis and a small cubic particle in the medium. The pressure, p , and velocity, u , fields are shown at the two faces of the particle perpendicular to the axis of propagation. The size of the particle is exaggerated to facilitate visualization. | 3 |
| 1.2 | A 2-D plane through a cubic tissue volume of length l . The nuclear area fraction of the plane is the sum of the areas of intersection between the nuclei in the tissue volume and the 2-D plane divided by the area of the plane. The nuclear area fraction of the plane varies as a function of the position, z , of the plane relative to one of the two parallel faces of the tissue volume. | 10 |
| 2.1 | The simulation grid divided into two parts showing the configuration of the dispersionless attenuation parameters, where L_x , L_y , and L_z are the dimensions of the simulation grid including the propagation medium and the PML region, and M_x , M_y , and M_z are the dimensions of the PML region. | 30 |
| 2.2 | (a) Staggered-space and (b) staggered-time sampling configuration of the total pressure and velocity fields. | 33 |
| 2.3 | An algorithm for distributing the scan lines between the nodes of a cluster. The $\lfloor \cdot \rfloor$ operator denotes rounding down to the nearest integer. | 37 |
| 2.4 | A schematic representation of a tissue-mimicking phantom composed of an infinite-length cylinder of diameter 1.7 mm with acoustic properties of connective tissue containing two internal spheres of diameters 0.5 and 0.4 mm with acoustic properties of fat and is surrounded by a background medium with acoustic properties of water at body temperature. The orientation of the x , y , and z axes are as shown in the figure, but the origin is located inside the phantom as described in the text. | 44 |

| | | |
|-----|--|----|
| 2.5 | Frequency-domain L^2 error of the 3-D k -space method as a function of normalized computational complexity when (a) the CFL number is varied between 0.1 and 1.3 and the spatial step is set to 4 points per minimum wavelength, and (b) the CFL number is set to 0.5 and the spatial step is varied between 2 and 12 points per minimum wavelength. | 47 |
| 2.6 | Difference between the desired linear frequency-dependent absorption and the analytical and simulated relaxation absorptions for (a) liver, (b) kidney, (c) myocardium, and (d) whole cells with acoustic properties given in Table 2.1. | 49 |
| 2.7 | Performance results achieved by partitioning the simulation grid of a single scan line. Speedup (dashed lines) and efficiency (solid lines) as functions of (a) the number of grid points along the z -axis with $N_x = N_y = 512$ using 16 nodes, and (b) the number of nodes for a $512 \times 512 \times 512$ grid. | 50 |
| 2.8 | Simulated B-mode images of a 3-D tissue mimicking phantom containing two spherical lesions of diameters 0.5 and 0.4 mm acquired when the focus of the transducer is located at $x = 0$, $y = 0$, and (a) $z = 0$, (b) $z = 0.05$, (c) $z = 0.10$, (d) $z = 0.15$, (e) $z = 0.20$, (f) $z = 0.25$, (g) $z = 0.30$, and (h) $z = 0.35$ mm. Panels (e) and (f) contain a shadow region with reduced brightness indicated with a white arrow. Scale bar = 0.5 mm. | 53 |
| 3.1 | Digitized images at $20\times$ magnification of healthy mouse liver stained with (a) DAPI and (b) H&E. Scale bar = $30 \mu\text{m}$ | 66 |
| 3.2 | Comparison of experimental and simulated microstructures of healthy mouse liver. (a) Histogram of the measured nuclear size distribution of healthy mouse liver; (b)-(d) 2-D descriptors of the spatial arrangement of nuclei centres in healthy murine liver slides and simulated healthy tissue slabs: (b) K-function, $k(r)$, (c) radial distribution function, $g(r)$, and (d) the probability density function $p(r)dr$ associated with the nearest neighbour distribution function, $p(r)$, are plotted as functions of distance, r , from an arbitrary nucleus centre. Error bars indicate mean \pm standard deviation of curves measured in thirteen digitized micrographs of the healthy liver specimen. | 74 |
| 3.3 | (a) A $250 \mu\text{m} \times 250 \mu\text{m} \times 3 \mu\text{m}$ slab through the simulated liver tissue showing nuclei sections and (b) a comparable digitized DAPI-stained histology slide of a healthy mouse liver. The dark blue circles in (a) represent the size and positions of cell nuclei in the simulated tissue. Scale bar = $30 \mu\text{m}$ | 76 |

| | | |
|-----|--|-----|
| 3.4 | Variability of experimental and simulated microstructures of healthy mouse liver. Standard deviation of the (a) K-function, $k(r)$, (b) radial distribution function, $g(r)$, and (c) nearest neighbour distribution function, $p(r)$, computed on thirteen digitized micrographs of the healthy liver specimen and ten simulated healthy tissue slabs are plotted as functions of distance, r , from an arbitrary nucleus centre. | 77 |
| 3.5 | Comparison of experimental and simulated microstructures of a murine B16F1 liver metastasis. (a) Histogram of the measured nuclear size distribution of the experimental liver metastasis; (b)-(d) 2-D descriptors of the spatial arrangement of nuclei centres in liver metastasis micrographs and simulated tumour slabs: (b) K-function, $k(r)$, (c) radial distribution function, $g(r)$, and (d) the probability density function $p(r)dr$ associated with the nearest neighbour distribution function, $p(r)$, are plotted as functions of distance, r , from an arbitrary nucleus centre. Error bars indicate mean \pm standard deviation of curves measured in five digitized micrographs of the liver metastasis specimen. | 78 |
| 3.6 | (a) A $250 \mu\text{m} \times 250 \mu\text{m} \times 3 \mu\text{m}$ slab through the simulated tumour tissue showing nuclei sections such that each nucleus is represented as a dark blue circle, (b) a comparable digitized DAPI-stained histology slide from the interior of an experimental B16F1 metastasis in mouse liver, and (c) a schematic representation of the DAPI image in (b) such that each nucleus is modeled as a circle with the same centre coordinates as the nuclei in the DAPI image and an area equal to the product of the nucleus area in the DAPI image and a scaling factor to correct for DAPI blurring. Scale bar = $30 \mu\text{m}$ | 79 |
| 3.7 | Variability of experimental and simulated microstructures of a murine B16F1 liver metastasis. Standard deviation of the (a) K-function, $k(r)$, (b) radial distribution function, $g(r)$, and (c) nearest neighbour distribution function, $p(r)$, computed on five digitized micrographs of the liver metastasis specimen and ten simulated tumour tissue slabs are plotted as functions of distance, r , from an arbitrary nucleus centre. . | 81 |
| 4.1 | Comparison of experimental B-modes images of healthy murine liver tissue and synthesized B-mode images of simulated healthy tissue. (a) Gray level histograms of six B-mode images of healthy liver tissue and four synthesized B-mode images of simulated healthy tissue; (b) an experimental B-mode image of healthy liver; (c) a synthesized B-mode image of simulated healthy tissue. Error bars indicate mean \pm standard deviation of the gray level histograms of the six experimental B-mode images. Scale bar = $94 \mu\text{m}$ | 104 |

- 4.2 Comparison of experimental B-modes images of a liver metastasis and simulated B-mode images synthesized for a simulated tumour with the nucleus sound speed and mass density values assumed for healthy tissue. (a) Gray level histograms of four B-mode images of an experimental liver metastasis and four B-mode images synthesized for a simulated tumour using the acoustic properties assumed for healthy tissue; (b) an experimental B-mode image of an experimental liver metastasis; (c) a B-mode image synthesized for a simulated tumour using the acoustic properties assumed for healthy tissue. Error bars indicate mean \pm standard deviation of the gray level histograms of the four experimental B-mode images. Scale bar = 94 μm 105
- 4.3 Comparison of experimental B-modes images of a liver metastasis and simulated B-mode images synthesized for a simulated tumour using nucleus sound speed and mass density of 1527 m/s and 1140.5 kg/m³ that are different from the values assumed for healthy tissue. (a) Gray level histograms of four B-mode images of an experimental liver metastasis and four B-mode images synthesized for a simulated tumour using nucleus acoustic properties different from the values assumed for healthy tissue; (b) an experimental B-mode image of an experimental liver metastasis; (c) a B-mode image synthesized for a simulated tumour using nucleus acoustic properties different from the values assumed for healthy tissue. Error bars indicate mean \pm standard deviation of the gray level histograms of the four experimental B-mode images. Scale bar = 94 μm 106

List of Symbols

| | |
|---------------|---|
| α | attenuation coefficient (ultrasound simulation) |
| α | the ratio of the attractive zone to nucleus diameter (tissue model) |
| β_{max} | the maximum ratio of cell to nucleus diameter |
| Δt | time step |
| Δx | spatial step along the x -coordinate |
| Δy | spatial step along the y -coordinate |
| Δz | spatial step along the z -coordinate |
| η | minimum number of nodes per scan line |
| θ | pair potential function |
| κ | compressibility |
| κ_i | modulus for the i th-order relaxation process |
| λ | wavelength at the centre frequency |
| ξ | total number of scan lines |
| ρ | mass density |
| τ_i | relaxation time for the i th-order relaxation process |
| ψ | number of discrete groups of nuclei diameters |
| c | sound speed |
| c_0 | sound speed of the background medium |
| D_{max} | maximum diameter of the nuclei sections in histology slides |
| f | temporal frequency |
| \mathcal{F} | three-dimensional spatial Fourier transform |

| | |
|--------------------|--|
| \mathcal{F}^{-1} | three-dimensional inverse spatial Fourier transform |
| g | radial distribution function |
| k | spatial frequency (ultrasound simulation) |
| k | K-function (tissue model) |
| M | number of cells |
| $N_a(i)$ | number of nuclei sections of diameters between $(i - 1)\frac{D_{max}}{\psi}$ and $i\frac{D_{max}}{\psi}$ per unit area |
| $N_a(i, j)$ | number of nuclei sections of diameters between $(i - 1)\frac{D_{max}}{\psi}$ and $i\frac{D_{max}}{\psi}$ per unit area produced by nuclei of diameter $j\frac{D_{max}}{\psi}$ |
| $N_v(j)$ | number of nuclei of diameter $j\frac{D_{max}}{\psi}$ per unit volume of tissue |
| p | total pressure field (ultrasound simulation) |
| p | nearest neighbour distribution function (tissue model) |
| r | three-dimensional spatial vector (ultrasound simulation) |
| r | distance from an arbitrary nucleus centre (tissue model) |
| t | time |
| u | velocity field |
| V_{att} | maximum attractive energy between two cells with overlapping attractive zones |
| V_{rep} | maximum repulsive energy between two overlapping cells |
| V_v | nuclear volume fraction |
| x | lateral direction (perpendicular to the propagation axis) |
| y | axial direction (along the propagation axis) |
| z | elevation (out of plane) direction |
| \pm | plus or minus |
| \sim | approximately |
| $*$ | temporal convolution |

List of Acronyms & Abbreviations

| | |
|--------|---------------------------------------|
| 1-D | one-dimensional or one dimension |
| 2-D | two-dimensional or two dimensions |
| 3-D | three-dimensional or three dimensions |
| CFL | Courant-Friedrichs-Lewy number |
| DAPI | 4',6-diamidino-2-phenylindole |
| DOF | depth of field |
| FFT | fast Fourier transform |
| H&E | hematoxylin and eosin |
| LR | lateral resolution |
| MPI | Message Passing Interface |
| OpenMP | Open Multi-Processing |
| PML | perfectly matched layer |

Chapter 1

Introduction

1.1 Overview

High-frequency (20-60 MHz) ultrasound imaging is an attractive modality to non-invasively study cancer biology and anti-cancer therapy in preclinical models. Substantial progress has been made toward using high-frequency ultrasound scanners to track tumour growth and treatment response in small animal research. However, the relationships between high-frequency ultrasound backscattering and tissue microanatomy are complex and incompletely understood. Investigating these relationships would extend the use of high-frequency ultrasound imaging to provide information about tumour microstructure that complement conventional metrics such as tumour size and shape.

This thesis presents a three-dimensional (3-D) parallel ultrasound simulator and a 3-D computational model of tissue microanatomy to contribute to research to relate high-frequency ultrasound backscattering to tissue acoustic and microstructural properties. To develop the 3-D ultrasound simulator, a two-dimensional (2-D) numerical method, called the k -space method, that computes acoustic propagation in a fluid medium is extended to support 3-D computations. The 3-D simulator is implemented to run on a cluster of computers to enable high-frequency ultrasound imaging sim-

ulations with short running time. The tissue model describes tissue microstructural properties that are hypothesized to be major determinants of high-frequency ultrasound scattering. Accurate estimates of these properties are obtained for a healthy mouse liver and an experimental mouse liver metastasis specimen using stereological techniques adopted from materials science. The tissue model, which is also run on a computer cluster, is configured to produce simulated healthy and tumour tissues with microstructural properties that match the values estimated for the healthy and cancerous liver specimens. The parallel 3-D simulator is used to synthesize ultrasound images of the simulated healthy and tumour tissues when the acoustic properties assigned for the simulated tumour are and are not the same as the values assumed for healthy tissue. The first-order speckle statistics of the synthesized images of the simulated healthy and tumour tissues are compared with matching experimental images.

To provide background for the material present in the thesis, this chapter first reviews the first-order wave equations that describe one-dimensional (1-D) linear acoustic propagation in a lossless homogeneous fluid medium, which is a simplified form of the 3-D linear acoustic propagation in an inhomogeneous fluid medium with frequency-dependent absorption solved by the proposed 3-D ultrasound simulator. Existing 3-D ultrasound simulators many of which use simplifying assumptions to reduce the simulation complexity, are reviewed for comparison with the k -space simulator. Parallel computing technology employed by the proposed 3-D ultrasound simulator and the tissue model to enable full 3-D imaging simulations is discussed including parallel computing systems and programming models. The stereological techniques used to estimate the morphological properties included in the tissue model for the healthy and cancerous liver specimens are summarized. Previous studies of high-frequency ultrasound scattering are reviewed. The thesis hypothesis and objectives are stated, followed by an outline of the subsequent thesis chapters.

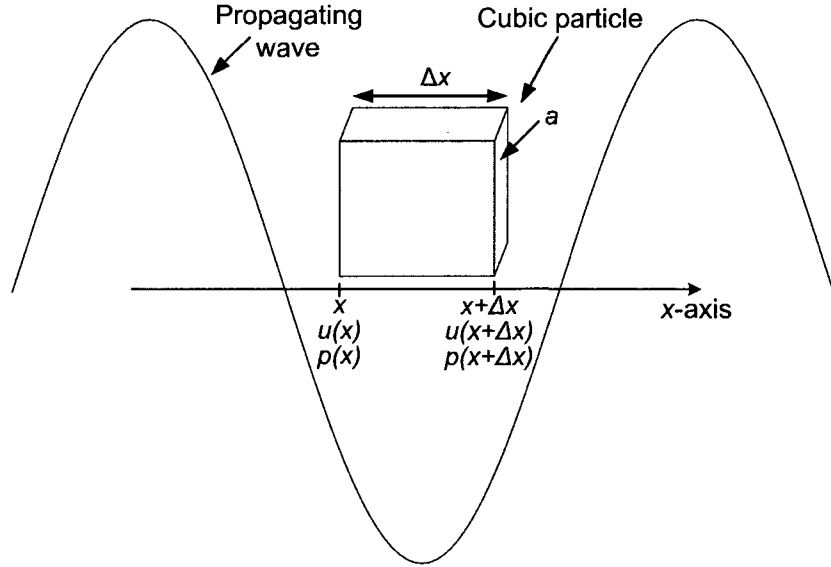


Fig. 1.1: Plane wave propagating in a fluid medium along the x axis and a small cubic particle in the medium. The pressure, p , and velocity, u , fields are shown at the two faces of the particle perpendicular to the axis of propagation. The size of the particle is exaggerated to facilitate visualization.

1.2 The wave equation

A derivation of the one-dimensional (1-D) linear acoustic wave equation in a lossless homogeneous fluid medium is presented based on the formulation given in [1]. Since longitudinal propagation is the most significant type of acoustic propagation in soft tissue at mega-Hertz frequencies, shear propagation is not included in the derivation.

Consider a 1-D wave in a fluid medium propagating along the x axis and a cubic particle in the medium aligned such that two of its faces are perpendicular to the propagation axis. The particle has a length Δx , a face area a , and dimensions much smaller than the wavelength of the propagating wave. A schematic representation of the 1-D wave and the particle is given in Fig. 1.1, where the size of the particle is exaggerated to facilitate visualization.

The conservation of mass law states that the time rate of change of the particle

mass is equal to the net mass per unit time entering the particle. The mass per unit time leaving the particle through a small surface element is equal to the product of the mass density, $\rho(x)$, at the centre of the element, the area of the element, and the dot product of the outward normal unit vector of the element and the local velocity of the medium particles, $u(x)$, at the centre of the element [2]. The net mass leaving the particle per unit time is accordingly equal to the integral over the particle surface of the mass per unit time leaving through a small surface element. Since the wave is propagating along the x axis, variations in the spatially varying quantities, including $u(x)$ and $\rho(x)$, are only considered along the propagation axis. Therefore, the net mass per unit time entering the particle can be written as $-a[(\rho(x + \Delta x)u(x + \Delta x) - \rho(x)u(x))]$, where x and $x + \Delta x$ are the x coordinates at the two faces of the particle perpendicular to the propagation axis. The conservation of mass law applied to the particle can be written as:

$$-a[(\rho(x + \Delta x)u(x + \Delta x) - \rho(x)u(x))] = \frac{\Delta m}{\Delta t} \quad (1.1)$$

where m is the mass of the particle and t is time. Eq. 1.1 can be written as a partial differential equation by expressing the particle mass as the product of the particle volume and mass density, dividing both sides by the volume of the particle, and taking the limit as Δx and Δt approach 0 to obtain:

$$\frac{\partial(\rho u)}{\partial x} = -\frac{\partial \rho}{\partial t} \quad (1.2)$$

The propagation of the wave produces perturbation to the steady state value of the mass density in the absence of the wave. Therefore, the mass density can be expressed as $\rho = \rho_0 + \rho_1$, where ρ_0 and ρ_1 are the steady state value of the mass density and the time-varying acoustic contribution to the density, respectively. The value of ρ_1 is equal to $\rho_0 \kappa p$, where the constant κ is the compressibility of the fluid medium and p is the pressure field produced by the acoustic wave above the steady state value of the pressure in the absence of the wave. For imaging applications, the

amplitude of the acoustic waves is small, and hence the perturbations of p , u , and ρ are small. A linear approximation neglects the second- and higher-order terms that include products of two or more instances of ρ_1 , p , u , $\partial u/\partial x$, or $\partial u/\partial t$. By expressing ρ as the sum of ρ_0 and ρ_1 and using the linear approximation, Eq. 1.2 can be written as:

$$\frac{\partial u}{\partial x} = -\kappa \frac{\partial p}{\partial t} \quad (1.3)$$

For a plane wave in a fluid, the compressibility of the medium is related to the longitudinal speed, c , of the wave by $\kappa = \frac{1}{\rho_0 c^2}$. Therefore, the conservation of mass law of Eq. 1.3 can be expressed as:

$$\frac{\partial u}{\partial x} = -\frac{1}{\rho_0 c^2} \frac{\partial p}{\partial t} \quad (1.4)$$

Newton's second law requires the net force, F , acting on the particle to be equal to the time rate of change of the particle momentum, $\frac{d(mu)}{dt}$. Since the dimensions of the particle are much smaller than the wavelength, variations in the mass density within the particle are small, and hence the density within the particle can be approximated as a single time-varying quantity, ρ . By evaluating the time rate of change of the particle momentum using the chain rule for differentiation, substituting the particle velocity, u , for the partial derivative of the particle position with respect to time, and expressing the particle mass as the product of the particle volume and mass density, Newton's second law can be written as:

$$F = \rho a \Delta x \left(\frac{du}{dt} + u \frac{\partial u}{\partial x} \right) \quad (1.5)$$

The net force acting on the particle is equal to the difference between the forces applied on the two particle faces perpendicular to the propagation axis. Since the magnitude of the force per unit area is equal to the pressure, the net force acting on the particle can be expressed as $F = a(p(x) - p(x + \Delta x))$. Newton's force law can be written as a partial differential equation by expressing the net force, F , in Eq. 1.5 in terms of a and $p(x)$, dividing both sides by the volume of the particle, and taking

the limit as Δx approaches 0:

$$-\frac{\partial p}{\partial x} = \rho \left(\frac{\partial u}{\partial t} + u \frac{\partial u}{\partial x} \right) \quad (1.6)$$

Using the linear approximation employed in Eq. 1.3, Eq. 1.6 can be written as:

$$\frac{\partial p}{\partial x} = -\rho_0 \frac{\partial u}{\partial t} \quad (1.7)$$

Eq. 1.4 and Eq. 1.7 are called the coupled 1-D first-order linear acoustic wave equations in a homogeneous lossless fluid medium and they explicitly describe the coupling between the pressure and particle velocity fields. The mathematical formulation of these equations is similar to the coupled 3-D first-order linear acoustic wave equations in a lossless fluid medium with spatially varying sound speed and mass density used in chapter 2 to extend the k -space method to enable 3-D computations.

The 1-D second-order wave equation can be derived by taking the partial temporal derivative of Eq. 1.4 and the partial spatial derivative of Eq. 1.7, and then combining the two equations to obtain a second-order partial differential equation that describes pressure field propagation:

$$\frac{\partial^2 p}{\partial x^2} - \frac{1}{c^2} \frac{\partial^2 p}{\partial t^2} = 0 \quad (1.8)$$

Eq. 1.8 is the 1-D second-order linear acoustic wave equation commonly used in engineering and applied physics literature.

1.3 3-D simulation of ultrasound imaging

Realistic 3-D ultrasound imaging studies involve computing large-scale simulations with propagation volumes on order of hundreds of wavelengths. Computing full 3-D simulations with such propagation volumes require extensive processing and memory resources that exceed the capabilities of contemporary serial computers. To reduce the computational complexity of the simulation, many 3-D ultrasound simulators employ simplifying assumptions such as axisymmetric propagation and the Born approximation [3]. Axisymmetric propagation assumes a symmetric propagation medium and

ultrasound source. This assumption is used in a commercial software package, called Wave2500* [4], in which the properties of the propagation medium are not allowed to change as a function of the angular dimension of the cylindrical coordinate system when the radial and height dimensions are fixed. Moreover, the ultrasound source is assumed to be symmetric with respect to the angular dimension.

In the Born approximation, the scattered field is assumed to be weak compared to the incident field, and hence an echo signal can be computed as a linear superposition of echoes from independent scatterers. This approximation is valid for a weakly scattering medium that contains scatterers of small size compared to the incident wavelength and mass density and compressibility close to the background. The Born approximation is used in [5, 6] to compute 3-D scattered fields.

The use of simplifying assumptions in 3-D ultrasound simulators might restrict the application of these simulators to a specific set of problems that satisfies the assumptions. To enable fast and accurate 3-D large-scale simulations without simplifying assumptions, it is necessary to combine efficient numerical methods, which obtain high accuracy and stability using minimal computational resources, with the use of parallel and distributed systems.

1.4 Parallel Computing

Preclinical imaging problems intended to be studied using the software tools developed in this thesis involve using the stochastic tissue model to create simulated tissue volumes on the order of tens or hundreds of wavelengths and computing acoustic propagation in these volumes using the 3-D ultrasound simulator. The running time of such studies on serial computers varies between a few weeks and a few months. The long running time limits the use of this software in imaging research.

*The axisymmetric simplifying assumption has been relaxed in a newer version of this software called Wave3000 (<http://www.cyberlogic.org>).

To overcome this problem, parallel and distributed systems offer powerful computing resources to run the proposed tissue model and ultrasound simulator to carry out imaging simulations with short running time. Two important classes of parallel and distributed systems are symmetric multiprocessing (SMP) systems and distributed-memory computer clusters. A SMP system is a group of processors that share the same computer bus and global memory. The processors of a SMP system run identical operating system copies and collaborate to execute parallel applications. The shared address space of a SMP system enables the processors to communicate by writing to and reading from the shared memory [7, 8]. Parallel applications can be developed for SMP systems using programming standards that support shared address space such as the Open Multi-Processing (OpenMP) [9] standard. In this thesis, the term shared-memory computer clusters refers to the SMP systems.

A distributed-memory computer cluster is a group of independent computers that communicate with each other via a high-speed communication network or networks. The computers have their own processors and local memories and they work together as a single system to execute parallel applications [7]. The interactions between the computers of a distributed-memory cluster are accomplished using the message passing model [10]. In this model, computational tasks running on different computers communicate by sending and receiving messages. The transfer of messages between tasks requires cooperative operations to be performed by each task, *i.e.*, a send operation on the sending computer must have a matching receive operation on the receiving computer. One programming standard that supports the message passing model is the Message Passing Interface (MPI) [11] standard that provides a rich set of messaging primitives to develop parallel programs for distributed-memory clusters. Since the intra-computer bus speed is much higher than the speed of the interconnection network, obtaining high performance on a distributed-memory cluster requires consideration of the inter-computer communication overhead that occurs when tasks allocated to different computers exchange data. Hence, there is a tradeoff between

the speedup gained through parallelization and the overhead of inter-computer communication.

Developing parallel applications for distributed-memory clusters, in which each processing node has its own address space, is more difficult than shared-memory clusters. On the other hand, the number of processors supported by distributed-memory clusters is more scalable than shared-memory clusters. Distributed-memory clusters have good performance-to-cost ratio and provide a low-cost alternative to dedicated parallel machines such as shared-memory clusters [12]. In this thesis, the ultrasound simulator is implemented to run on distributed-memory clusters and the tissue model is run on shared-memory clusters.

1.5 Quantifying tissue microstructure

Several studies have suggested that cell nuclei are significant determinants of high-frequency ultrasound scattering in tissue [13–15]. Therefore, accurate estimation of the volume fraction and sizes of the nuclei in the tissue is crucial for developing tissue computational models for high-frequency ultrasound simulations. Stereology, defined as estimating features of a 3-D structure using random 2-D sections or projections [16], provides techniques to quantify the volume fraction and size distribution of the nuclei based on tissue histology slides.

The nuclear volume fraction is defined as the sum of all nuclei volumes in the tissue divided by the total tissue volume. The volume fraction of the nuclei can be related to the nuclear area fraction in a random 2-D plane through the tissue using the stereological method presented in [17]. To derive the relationship between the volume and area fractions, consider a cubic volume in the tissue with a length l and a random parallel plane through the volume (Fig. 1.2). Assume that z is the spacing between the plane and one of the two faces of the tissue volume parallel to the plane. The nuclear area fraction of the plane at spacing z can be written as $\frac{A(z)}{l^2}$, where $A(z)$

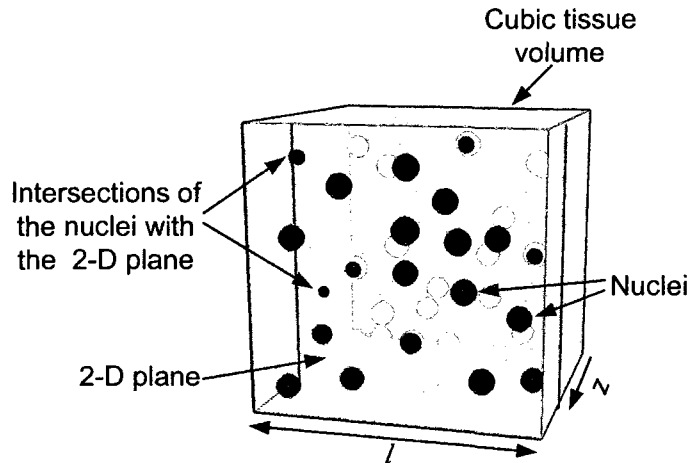


Fig. 1.2: A 2-D plane through a cubic tissue volume of length l . The nuclear area fraction of the plane is the sum of the areas of intersection between the nuclei in the tissue volume and the 2-D plane divided by the area of the plane. The nuclear area fraction of the plane varies as a function of the position, z , of the plane relative to one of the two parallel faces of the tissue volume.

is the total area of intersection between the plane and the nuclei. If the position, z , of the plane is chosen from a uniform distribution between 0 and l , then the expected value, $\overline{A_{(a)}}$, of the nuclear area fraction of the plane computed over the entire domain of z can be written as:

$$\overline{A_{(a)}} = \int_0^l \frac{A(z)}{l^2} \frac{1}{l} dz \quad (1.9)$$

where $\frac{dz}{l}$ is the probability of choosing a plane with a position between z and $z + dz$. Since the integration $\int_0^l A(z) dz$ is equal to the sum of nuclei volumes in the tissue cube, the expected value, $\overline{A_{(a)}}$, of the nuclear area fraction in a random plane through the tissue cube is equal to the nuclear volume fraction of the tissue cube. Therefore, the nuclear volume fraction of the tissue is equal to the average nuclear area fraction computed from random 2-D planes through the tissue.

The average nuclear area fraction can be estimated using randomly chosen histology slides from the tissue. However, the total area of the nuclei measured with the microscope from a tissue histology slide of a finite thickness is based on a planar

projection of nuclei sections within the slide, which overestimates the intersection between the nuclei and the 2-D surface of the slide. This artefact is called Holmes effect [18]. The Holmes effect can be corrected by employing histology slides of small thickness and applying a correction factor that depends on the average nucleus diameter and the thickness of the slides.

The distribution of the nuclei sizes in the tissue can be estimated from the sizes of the nuclei sections observed in the tissue histology slides using the Schwartz-Saltykov method [19]. The Schwartz-Saltykov method is briefly described here based on detailed mathematical formulation presented in [19]. To apply the Schwartz-Saltykov method, the nuclei are assumed to have spherical shape and be randomly distributed in the tissue. Moreover, the nuclei are assumed to have ψ discrete diameter values between $\frac{D_{max}}{\psi}$ and D_{max} , with an increment of $\frac{D_{max}}{\psi}$, where D_{max} is the measured maximum diameter of the nuclei sections in the histology slides. The value of ψ is usually between 7 and 15 depending on the required estimation accuracy. The nuclei sections are classified into ψ groups such that the i^{th} group includes nuclei sections of diameters between $(i - 1)\frac{D_{max}}{\psi}$ and $i\frac{D_{max}}{\psi}$. Since the nuclei sections from the i^{th} group can only be produced by nuclei of diameters greater than or equal to $i\frac{D_{max}}{\psi}$, the measured number of nuclei sections from the i^{th} group per unit area, denoted as $N_a(i)$, can be written as:

$$N_a(i) = \sum_{j=i}^{\psi} N_a(i, j) \quad (1.10)$$

where $N_a(i, j)$ is the number of nuclei sections from the i^{th} group per unit area produced by nuclei of diameter $j\frac{D_{max}}{\psi}$. It can be shown that a nucleus section from the i^{th} group in a tissue slab can be produced by a nucleus of diameter $j\frac{D_{max}}{\psi}$ only when the perpendicular distance between the centre of the nucleus and the 2-D surface of the tissue slab is between $\frac{D_{max}}{2\psi}\sqrt{j^2 - (i - 1)^2}$ and $\frac{D_{max}}{2\psi}\sqrt{j^2 - i^2}$ on both sides of the slab. Hence, the total tissue volume containing the centres of the nuclei of diameter $j\frac{D_{max}}{\psi}$ that produce nuclei sections from the i^{th} group in one unit area of the histology

slide is equal to $\frac{D_{max}}{\psi}(\sqrt{j^2 - (i-1)^2} - \sqrt{j^2 - i^2})$. If $N_v(j)$ is the number of nuclei of diameter $j \frac{D_{max}}{\psi}$ per unit volume of tissue, then $N_a(i, j)$ can be expressed as:

$$N_a(i, j) = N_v(j) \frac{D_{max}}{\psi} (\sqrt{j^2 - (i-1)^2} - \sqrt{j^2 - i^2}) \quad (1.11)$$

Varying i in Eq. 1.10 between 1 and ψ and substituting Eq. 1.11 for $N_a(i, j)$ lead to ψ independent equations with ψ unknowns, $N_v(1), N_v(2), \dots, N_v(\psi)$, and ψ measured quantities, $N_a(1), N_a(2), \dots, N_a(\psi)$. Hence, the distribution of nuclei diameters per unit volume of tissue can be estimated from the measured distribution of nuclei sections per unit area of the histology slides.

More recent methods have been developed to estimate the size distribution of particles with non-spherical shapes such as [20]. In this thesis, the nuclei are assumed to be approximately spherical, and hence the nuclear size distribution is quantified using the Schwartz-Saltykov method.

1.6 High-frequency ultrasound scattering models

High-frequency ultrasound scattering in tissue has been studied by numerous research groups who suggested various approaches to model ultrasound backscattering. For example, Mamou *et al.* [21] proposed a 3-D computational model of tissue microstructure derived from histology data to estimate ultrasound scattering sources. The model was constructed by mapping tissue microscopic structures to corresponding acoustic impedance values. The mapping process was achieved by fixing, slicing, and staining a tissue volume to obtain a group of adjacent 2-D histology slides in which each colour corresponds to a specific tissue type. The 2-D histology slides were digitized, aligned, and processed to construct a 3-D impedance matrix of the tissue volume. The model was used to estimate the mean scatterer size and acoustic concentration, defined as the product of the number density of scatterers and the square of the difference between the impedance of the scatterer and the surrounding medium,

of two mammary tumours. The estimation is carried out by deriving an analytical formula to compute the backscattered intensity based on the impedance-based model, and then fitting a form factor to the power spectrum of the medium computed by dividing the backscattered intensity by the fourth power of the wave number. The form factor is a model that represents the frequency-dependent backscattered intensity from a medium that contains an ensemble of identical scatterers. Comparisons with experimental ultrasound data showed good matching between the scatterer size estimated from the 3-D impedance-based model and the scatterer size estimated from experimentally measured ultrasound echoes. However, significant deviation was observed between the acoustic concentration estimated from the impedance-based model and the acoustic concentration obtained with ultrasound data.

Other studies suggested simulation-based scattering models that emphasized cells and nuclei as dominant scattering sites at high frequency. This approach is used by Hunt *et al.* [22], who proposed idealized 1-D and 2-D scattering models to study high-frequency ultrasound scattering in a homogeneous medium containing identical point-like cells configured to produce various regular and random spatial arrangements. Simulations performed with these models predicted significant correlation between high-frequency ultrasound backscattering and the randomization of cell positions. The assumption that high-frequency ultrasound scattering is correlated with the structural properties of cellular-scale features agrees with the empirical study by Czarnota *et al.* [13], which indicated that the significant change in the amplitude of high-frequency ultrasound backscattered signals that accompanies apoptosis in cell ensembles and tissue is related to condensation and fragmentation of the nucleus. To study the change of ultrasound backscattering associated with apoptosis, the 2-D model of [22] was extended in [14] to include nucleus morphology by representing each cell as a group of scatterers that approximate the nucleus structure. The extended 2-D model was used to carry out high-frequency ultrasound scattering simulations using different configurations that mimic the cell and nucleus structural variations that

occur during different stages of apoptosis. The simulations suggested that the change in ultrasound backscattering during apoptosis is dominated by the morphology and spatial arrangement of the nucleus.

The concept that cells and nuclei are dominant scattering sites at high-frequency was employed by Doyle *et al.* [15], who presented a 3-D simulation scattering model that treats tissue microstructure as a group of spherical cells embedded in an extracellular matrix, where each cell is represented as a spherical nucleus surrounded with homogeneous cytoplasm. High-frequency ultrasound scattering simulations were performed using the 3-D model with several hundred cells configured to produce a variable ratio of cell to nucleus diameter and various spatial arrangements including configurations that mimic single cells and tissue microstructural variations associated with malignant processes. In these simulations, 3-D acoustic propagation was computed using a multiple-scattering method [23] without incorporating attenuation. The simulations suggested that high-frequency ultrasound scattering from single cells is dominated by the size of the nuclei, which agrees with the empirical results reported by Taggart *et al.* [24], who studied ultrasound backscattering from cells and isolated nuclei. Moreover, the simulations suggested that both cellular- and tissue-scale microstructural variations associated with malignant processes produce significant changes in the spectra of high frequency ultrasound backscattered signals.

Oelze and O'Brien [25] presented a scattering model that treats the cell as a nucleus surrounded with cytoskeleton. The model, which is distinguished by including scattering from the cell cytoplasm, was used to estimate the average scatterer size of two tumours derived from different cell lines. The estimated scatterer size of both tumours suggested that high-frequency ultrasound scattering is dominated by cells or microstructures on the order of cell size.

1.7 Hypothesis and objectives

The hypothesis of this thesis is that simulations of high-frequency ultrasound imaging can be used in combination with a computational model of tissue microstructure to relate variations in tissue acoustic and microstructural properties to characteristics of high-frequency ultrasound images of healthy tissue and experimental tumours. Three research objectives are defined to investigate this hypothesis:

1. Develop and evaluate a parallel ultrasound simulator that enables 3-D high-frequency ultrasound imaging simulations with short running time.
2. Develop and evaluate a 3-D computational model that describes tissue microstructure based on stereological analyses of histology data.
3. Employ the ultrasound simulator and the tissue model to relate acoustic and microstructural properties of healthy and cancerous murine tissues to experimentally measured first-order speckle statistics of high-frequency ultrasound images.

1.8 Thesis outline

The thesis objectives defined above are presented separately in the following three chapters. These chapters are followed by a conclusion chapter that briefly discusses possible future directions for the research project presented in this thesis. A summary of each chapter is presented below.

1.8.1 Chapter 2

Chapter 2 describes the development and testing of a parallel 3-D simulator for B-mode ultrasound imaging simulations. The simulator is developed based on a 3-D formulation of a 2-D numerical method that computes acoustic propagation in a fluid

medium. The 3-D simulator, which computes the propagation of a single wavefront, is implemented to run on distributed-memory computer clusters. An allocation algorithm is introduced to divide the computation of each scan line among a group of cluster nodes and use multiple groups to compute independent lines concurrently. The accuracy of the simulator is analyzed using example calculations of ultrasonic propagation and attenuation in the 30-50 MHz band. The parallel efficiency of the simulator is evaluated for various combinations of number of scan lines and number of cluster nodes. An aperture-projection technique is introduced to simulate imaging with a focused transducer using reduced computation grids. The feasibility of 3-D imaging simulations using parallel computing is demonstrated by carrying out a B-mode imaging simulation with a tissue-mimicking phantom.

1.8.2 Chapter 3

Chapter 3 introduces a 3-D computational model of tissue microanatomy for high-frequency ultrasound imaging simulations. The model treats tissue microstructure as a group of stochastically positioned spherical cells embedded in a homogeneous extracellular matrix, where each cell consists of a spherical nucleus surrounded by homogeneous cytoplasm. The model is separately used to represent the microstructure of a healthy mouse liver and an experimental mouse liver metastasis specimen that are analyzed using stereological techniques to estimate the nuclear volume fraction and size distribution. The spatial organization of cells in the model is controlled by a stochastic point process. The parameters of the stochastic process are tuned to accurately reproduce the average number density and distribution of centre-to-centre spacing of nuclei in the histology slides of the corresponding experimental tissue specimen. The structural properties included in the model are hypothesized to be the most significant determinants of high-frequency ultrasound backscattering.

1.8.3 Chapter 4

The parallel 3-D ultrasound simulator is employed to synthesize high-frequency ultrasound B-mode images of simulated healthy and tumour tissues configured using the tissue model to reproduce the microstructure of healthy mouse liver and an experimental mouse liver metastasis, respectively. Ultrasound propagation is computed in the simulated healthy tissue using acoustic properties of tissue microanatomy reported in previous studies. Since tumour growth is expected to change the acoustic properties of tissue microstructure, various combinations of sound speed and mass density values are tested for the simulated tumour, where one of these combinations match the values assumed for healthy tissue. The first-order speckle statistics of the B-mode images synthesized for each simulated tissue are compared with matching experimental B-mode images.

1.8.4 Chapter 5

Chapter 5 contains a summary of the materials covered in chapters 2 through 4, discusses future directions for the research presented in the thesis, and concludes the thesis.

References

- [1] D. A. Christensen, “The wave equation and its solutions,” in *Ultrasonic Bioinstrumentation*, chapter 2. John Wiley & Sons, Hoboken, N.J., 1988.
- [2] A. D. Pierce, “The wave theory of sound,” in *Acoustics : An Introduction to Its Physical Principles and Applications*, chapter 1. Acoustical Society of America, Woodbury, N.Y., 2 edition, 1989.
- [3] R. K. Saha and S. K. Sharma, “Validity of a modified born approximation for a pulsed plane wave in acoustic scattering problems,” *Phys. Med. Biol.*, vol. 50, no. 12, pp. 2823–36, 2005.
- [4] J. J. Kaufman, G. Luo, and R. S. Siffert, “Ultrasound simulation for 3D-axisymmetric models,” in *Proc. IEEE Ultrason. Symp.*, 2003, vol. 2, pp. 2065–68.
- [5] S. J. Norton and M. Linzer, “Ultrasonic reflectivity imaging in three dimensions: exact inverse scattering solutions for plane,cylindrical, and spherical apertures,” *IEEE Trans. Biomed. Eng.*, vol. 28, no. 2, pp. 202–220, 1981.
- [6] B. G. Teh and G. Cloutier, “Modeling and analysis of ultrasound backscattering by spherical aggregates and rouleaux of red blood cells,” *IEEE Trans. Ultrason. Ferroelectr. Freq. Control*, vol. 47, no. 4, pp. 1025–35, 2000.
- [7] M. Baker and R. Buyya, “Cluster computing at a glance,” in *High Performance Cluster Computing*, R. Buyya, Ed., vol. 1, chapter 1. Prentice Hall PTR, Upper Saddle River, N.J., 1999.
- [8] S. Kumar, “Introduction of operating system,” in *Encyclopaedia of Operating System*, chapter 1. Anmol Publications PVT. LTD., New Delhi, India, 2004.
- [9] OpenMP Architecture Review Board, “OpenMP application program interface version 3.0,” <http://openmp.org/wp/openmp-specifications>.

- [10] D. B. Skillicorn and D. Talia, “Models and languages for parallel computation,” *ACM Comput. Surv.*, vol. 30, no. 2, pp. 123–169, 1998.
- [11] Message Passing Interface Forum, “MPI: A message-passing interface standard version 2.1,” Tech. Rep., University of Tennessee, Knoxville, TN, 2008.
- [12] A. Sulistio, C. S. Yeo, and R. Buyya, “A taxonomy of computer-based simulations and its mapping to parallel and distributed systems simulation tools,” *Softw. Pract. Exper.*, vol. 34, no. 7, pp. 653–673, 2004.
- [13] G. J. Czarnota, M. C. Kolios, J. Abraham, M. Portnoy, F. P. Ottensmeyer, J. W. Hunt, and M. D. Sherar, “Ultrasound imaging of apoptosis: high-resolution non-invasive monitoring of programmed cell death in vitro, in situ and in vivo,” *Br. J. Cancer*, vol. 81, no. 3, pp. 520–7, 1999.
- [14] J. W. Hunt, A. E. Worthington, A. Xuan, M. C. Kolios, G. J. Czarnota, and M. D. Sherar, “A model based upon pseudo regular spacing of cells combined with the randomisation of the nuclei can explain the significant changes in high-frequency ultrasound signals during apoptosis,” *Ultrasound Med. Biol.*, vol. 28, pp. 217–26, 2002.
- [15] T. E. Doyle, K. H. Warnick, and B. L. Carruth, “Histology-based simulations for the ultrasonic detection of microscopic cancer in vivo,” *J. Acoust. Soc. Am.*, vol. 122, pp. EL210–6, 2007.
- [16] A. Baddeley and E. B. Vedel Jensen, “Introduction,” in *Stereology for Statisticians*, chapter 1. Chapman & Hall/CRC, Boca Raton, F.L., 2005.
- [17] R. T. DeHoff and F. N. Rhines, “Measurement of volume in volume,” in *Quantitative Microscopy*, chapter 3. McGraw-Hill, New York, 1968.
- [18] A. H. Holmes, *Petrographic Methods and Calculations*, Murby and Company, London, 1927.

- [19] R. T. DeHoff and F. N. Rhines, "Particle size distribution," in *Quantitative Microscopy*, chapter 6. McGraw-Hill, New York, 1968.
- [20] R. T. DeHoff, "The determination of the size distribution of ellipsoidal particles from measurements made on random plane sections," *Trans. Met. Soc. AIME*, vol. 224, pp. 474–477, 1962.
- [21] J. Mamou, M. L. Oelze, W. D. O'Brien Jr., and J. F. Zachary, "Identifying ultrasonic scattering sites from three-dimensional impedance maps," *J. Acoust. Soc. Am.*, vol. 117, pp. 413–23, 2005.
- [22] J. W. Hunt, A. E. Worthington, and A. T. Kerr, "The subtleties of ultrasound images of an ensemble of cells: simulation from regular and more random distributions of scatterers," *Ultrasound Med. Biol.*, vol. 21, pp. 329–41, 1995.
- [23] T. E. Doyle, "Iterative simulation of elastic wave scattering in arbitrary dispersions of spherical particles," *J. Acoust. Soc. Am.*, vol. 119, pp. 2599–2610, 2006.
- [24] L. R. Taggart, R. E. Baddour, A. Giles, G. J. Czarnota, and M. C. Kolios, "Ultrasonic characterization of whole cells and isolated nuclei," *Ultrasound Med. Biol.*, vol. 33, pp. 389–401, 2007.
- [25] M. L. Oelze and W. D. O'Brien Jr, "Application of three scattering models to characterization of solid tumors in mice," *Ultrason. Imaging*, vol. 28, no. 2, pp. 83–96, 2006.

Chapter 2

Distributed Three-Dimensional Simulation of B-mode Ultrasound Imaging Using a First-Order k -Space Method

*A shortened version of this chapter has been accepted for publication in *Physics in Medicine and Biology** with author list M. I. Daoud and J. C. Lacefield.*

2.1 Introduction

Many ambitious applications have been identified for detailed simulations of ultrasound image formation [1–3]. For example, simulations have the potential to suggest new insights into the physical interactions of ultrasound and tissue, leading to improved methods of tissue characterization and automated image analysis and enabling

*© 2009 Institute of Physics. Reprinted, with permission, from *Physics in Medicine and Biology* (<http://www.iop.org/journals/PMB>), “Distributed Three-Dimensional Simulation of B-mode Ultrasound Imaging Using a First-Order k -Space Method” by M. I. Daoud and J. C. Lacefield.

correlations to be identified between the morphological and functional information depicted in medical images and the underlying biological processes. It has even been suggested that such computations could be employed to perform “patient-specific imaging” [3], in which information gleaned from medical images is integrated with other clinical data from a patient to improve the sensitivity and specificity of medical diagnosis. However, relatively limited progress has been made toward this vision [3].

Computational complexity remains a major barrier to this type of research, because ultrasound imaging problems involve large-scale simulations with propagation distances on the order of hundreds of wavelengths, and hence require extensive computational resources and long running times. Therefore, many ultrasound simulators employ techniques to reduce the complexity of a simulation, such as computing two-dimensional (2-D) propagation only or using simplifying assumptions to carry out three-dimensional (3-D) simulations. The simulator used most commonly for medical ultrasound research is Field II [4], which computes B-mode images by superimposing spatial impulse responses to a population of point scatterers. A 3-D imaging simulation can be completed in a few hours using Field II [5], but the spatial impulse responses are computed using the Rayleigh integral and so assume propagation through a homogeneous medium. To perform accurate and fast 3-D simulations without simplifying assumptions, it is necessary to combine efficient numerical methods, which attain high accuracy and stability using minimal computational resources, with the use of parallel and distributed systems. Efficient parallel computation is especially crucial in view of the number of pulse-echo acquisitions that must be simulated to synthesize an image.

The majority of ultrasound simulation methods can be classified into four main groups: finite-difference methods, finite-element methods, pseudospectral methods, and k -space methods [6, 7]. In finite-difference and finite-element methods, the computations to propagate the acoustic field at each point involve only nearby points. Pseudospectral and k -space methods, which are both considered spatial-frequency

spectral methods, use points from the entire computation grid to propagate the acoustic field. Pseudospectral methods approximate temporal derivatives using numerical techniques such as finite-difference methods, which introduce numerical dispersion errors. The k -space methods are distinguished from pseudospectral methods by the inclusion of a temporal correction term that minimizes the numerical dispersion. The combination of these two features permits k -space methods to achieve high numerical accuracy with much coarser spatial grids and time steps than are needed for finite-difference or finite-element computations [6, 7]. Use of coarse spatial grids does require low-pass filtering of the medium, in which case any high-spatial-frequency components of scattering will not be included in the computation.

One formulation of a k -space method is the algorithm developed by Mast *et al.* [6] based on second-order wave equations. Two-dimensional [6] and 3-D [8] simulations have been demonstrated using the second-order k -space method. The second-order method was subsequently extended to a formulation based on coupled first-order equations [9] that has been used for 2-D simulations of focus aberration [10] and photoacoustics [7]. Neglecting errors introduced by discrete evaluation of the Fourier transform and the limits imposed by machine precision, both k -space methods are essentially exact for homogeneous propagation media and provide high accuracy and stability for weakly inhomogeneous media, such as soft tissue. The advantages of the first-order k -space method relative to the second-order method are that the first-order method includes frequency-dependent attenuation and supports the use of perfectly matched layer (PML) absorbing boundary conditions. The perfectly matched layers reduce the wrap-around artefacts that occur in the second-order formulation as a result of the periodic boundary conditions imposed by the discrete spectral evaluation of spatial derivatives. The PML boundary conditions enable the use of smaller computation grids, because otherwise the grid must be much larger than the region of interest to avoid wrap-around artefacts. The ability to minimize the size of the computation grid is crucial for large imaging simulations involving computation of many

scan lines. In this thesis, the first-order k -space method is extended to compute 3-D propagation of total pressure [11]. A 3-D formulation of the first-order k -space method was developed separately to calculate scattered pressure propagation [12]. The 3-D total-pressure solver is employed in all simulations presented in this thesis.

Although the k -space methods achieve high accuracy using coarse temporal and spatial steps, they still require large memory and processing resources as well as long running times to carry out large-scale imaging simulations that involve multiple scan lines. For example, a typical B-mode imaging problem would involve computation of 128 scan lines, where in each scan line an ultrasound pulse with a Gaussian envelope, a centre frequency of f_c , and -6 -dB bandwidth of $0.6f_c$, is propagated in a 3-D medium with a background sound speed c_0 and a volume of $250\lambda \times 250\lambda \times 250\lambda$, where λ is the wavelength at the centre frequency. Assume that the pulse is transmitted from a transducer located on the top of the medium, and the simulation is run until the scattered waves from the entire medium are received by the transducer. The k -space methods described above require 4 grid points per minimum wavelength to ensure a reasonable accuracy. For a pulse with a Gaussian envelope and -6 -dB bandwidth of $0.6f_c$, the maximum frequency, which is used to calculate the 4 grid points per minimum wavelength spatial step, is assumed to be $1.773f_c$ corresponding to the upper -40 -dB frequency of the pulse spectrum. Therefore, each scan line requires a 3-D computation grid of 5.57×10^9 points. Using a time step size of $0.071 \frac{\lambda}{c_0}$, which corresponds to a Courant-Friedrichs-Lewy (CFL) number [13] of 0.5, the simulation requires around 7100 time steps, or 3.95×10^{13} grid-point evaluations, to compute each scan line. Assuming that the computation to update each grid point requires 40 floating-point operations, then the simulation involves 2.02×10^{17} floating-point operations. Hence, the running time of this simulation on serial computers, with typical performance of several Gflops, is on the order of hundreds of days. Moreover, the simulation of each line requires the storage of multiple memory buffers, each with a size on the order of gigabytes for single-precision computations.

A computation of this size demands the use of parallel and distributed systems. One approach to parallel computation is to use dedicated parallel machines that usually employ fine-grained partitions, meaning the computation is spread over many processors. A low cost alternative to dedicated parallel machines is to use computer clusters [14]. In general, computer clusters have a good performance-to-cost ratio, and therefore tend to be a more accessible method of high-performance computing for most users. Therefore, this chapter presents a parallel 3-D implementation of the first-order k -space method that runs on a distributed-memory computer cluster. The challenge of using a distributed-memory cluster is that the communication overhead between the nodes of a cluster is usually higher than that of dedicated parallel machines. Hence, efficient parallelization on computer clusters requires minimizing the communication overhead by assigning coarse partitions of dependent computations to a relatively small number of processors.

In the following sections, the first-order k -space method is extended to compute three-dimensional propagation of the total pressure field. Moreover, this chapter presents an analysis of the computational resources necessary for a single 3-D k -space computation, including the trade-off between numerical accuracy and computational complexity in simulating acoustic propagation and linear frequency-dependent attenuation over a broad bandwidth, and the parallel efficiency and speedup gained by using different numbers of processors in a cluster. For imaging simulations that require computation of many scan lines, it is more efficient to distribute the scan lines between cluster nodes rather than partitioning the simulation grid of individual scan lines. Multiple scan lines can then be computed concurrently [15]. However, when simulations are extended to three dimensions, the memory requirements quickly become too large to permit a scan line to be computed using a single processor on contemporary parallel systems. Therefore, this chapter also introduces an allocation algorithm to most efficiently divide the computation of each scan line among groups of processors of close communication and use multiple groups of processors to compute

independent scan lines concurrently. To further economize computational resources, an aperture-projection algorithm is presented that permits the computations to be limited to a small field of view around the region of interest. Finally, an imaging simulation is conducted to demonstrate the feasibility of large-scale 3-D simulations using parallel computing. Images are synthesized in reasonable running times by minimizing the grid size using the aperture-projection technique and the results of the accuracy analysis and then distributing the computational tasks between the processors using the allocation algorithm. The imaging simulation demonstrates that the effects of computing 3-D, rather than 2-D, propagation can be recognized in B-mode images synthesized using this approach.

2.2 Theory

2.2.1 3-D first-order k -space method

In this section, the first-order k -space method is reviewed and formalized to compute three-dimensional propagation of the total pressure field based on the derivation scheme employed in [9] for the 2-D first-order k -space method.

The first-order k -space method solves coupled first-order linear acoustic wave equations in a lossless fluid medium with spatially variable sound speed and mass density, which are given by [16]:

$$\nabla p(r, t) = -\rho(r) \frac{\partial u(r, t)}{\partial t} \tag{2.1}$$

$$\nabla \cdot u(r, t) = -\frac{1}{\rho(r)c(r)^2} \frac{\partial p(r, t)}{\partial t}$$

where $p(r, t)$ is the total pressure field, $u(r, t)$ is the velocity field, $\rho(r)$ is the spatially dependent mass density, $c(r)$ is the spatially dependent sound speed, and r represents a 3-D spatial vector coordinate (x, y, z) .

The spatial derivatives in Eq. 2.1 can be evaluated accurately using the Fourier transform [17]:

$$\frac{\partial\Phi(r,t)}{\partial\zeta} = \mathcal{F}^{-1}\{ik_\zeta\mathcal{F}\{\Phi(r,t)\}\} \quad (2.2)$$

where ζ denotes x , y , or z , the function $\Phi(r,t)$ can be any bandlimited signal, \mathcal{F} is the 3-D spatial Fourier transform, \mathcal{F}^{-1} is the inverse spatial Fourier transform, and (k_x, k_y, k_z) are the 3-D components of the spatial frequency k that are defined such that $k^2 = k_x^2 + k_y^2 + k_z^2$. The assumption of bandlimited acoustic fields is justified since typical ultrasound pulses have bandlimited spectra. The temporal derivatives in Eq. 2.1 can be approximated using a finite-difference scheme:

$$\frac{\partial\Phi(r,t)}{\partial t} \approx \frac{\Phi(r,t + \Delta t/2) - \Phi(r,t - \Delta t/2)}{\Delta t} \quad (2.3)$$

where Δt is the time step. However, this finite-difference approximation of temporal derivatives introduces significant dispersion errors.

Since each equation in Eq. 2.1 evaluates coupled temporal and spatial derivatives, the first-order k -space method uses Eq. 2.3 to evaluate the temporal derivative and employs a set of operators, called the first-order k -space operators, to both accurately evaluate the spatial derivative using the Fourier transform and correct for the error introduced by the discrete evaluation of the temporal derivative. Following the derivation scheme in [9], it can be shown that the 3-D first-order k -space operators can be expressed as:

$$\frac{\partial\Phi(r,t)}{\partial(c_0\Delta t)^+\zeta} \equiv \mathcal{F}^{-1}\{ik_\zeta e^{ik_\zeta\Delta\zeta/2} \text{sinc}(c_0\Delta tk/2)\mathcal{F}\{\Phi(r,t)\}\} \quad (2.4)$$

$$\frac{\partial\Phi(r,t)}{\partial(c_0\Delta t)^-\zeta} \equiv \mathcal{F}^{-1}\{ik_\zeta e^{-ik_\zeta\Delta\zeta/2} \text{sinc}(c_0\Delta tk/2)\mathcal{F}\{\Phi(r,t)\}\}$$

where ζ denotes x , y , or z , $\Delta\zeta$ is the spatial step along the ζ -coordinate, $\text{sinc}(x) = \sin(x)/x$, c_0 is the sound speed in the background medium, and $\text{sinc}(c_0\Delta tk/2)$ is the temporal correction term. The exponential coefficients in Eq. 2.4 indicate

that the first-order k -space operators shift the function $\Phi(r, t)$ by half spatial steps before evaluating the spatial derivatives and applying the temporal correction terms. For instance, the operator $\partial\Phi(r, t)/\partial^{(c_0\Delta t)^-} x$ evaluates the derivative of $\Phi(r, t)$ with respect to x and applies the temporal correction term after performing a spatial shift of $-\Delta x/2$. Hence, the $(c_0\Delta t)^-$ and $(c_0\Delta t)^+$ operators must be combined in a way that cancels out the introduced spatial shifts.

Using Eq. 2.3 and Eq. 2.4, the first-order k -space method equivalent to Eq. 2.1 can be written as:

$$\frac{u_\zeta(r^\zeta, t^+) - u_\zeta(r^\zeta, t^-)}{\Delta t} = -\frac{1}{\rho(r^\zeta)} \frac{\partial p(r, t)}{\partial^{(c_0\Delta t)^+} \zeta}, \forall \zeta = \{x, y, z\} \quad (2.5)$$

$$\frac{p(r, t + \Delta t) - p(r, t)}{\Delta t} = -\rho(r)c(r)^2 \sum_{\zeta=\{x,y,z\}} \frac{\partial u_\zeta(r^\zeta, t^+)}{\partial^{(c_0\Delta t)^-} \zeta}$$

where $u_x(r, t)$, $u_y(r, t)$, and $u_z(r, t)$ are the x , y , and z components of the velocity field, $r^x = (x + \Delta x/2, y, z)$, $r^y = (x, y + \Delta y/2, z)$, and $r^z = (x, y, z + \Delta z/2)$, and $t^+ = t + \Delta t/2$ and $t^- = t - \Delta t/2$. As discussed in [9], this k -space method is not subject to any dispersion error for the case of a homogeneous medium, i.e. $\rho(r)=\rho_0$ and $c(r)=c_0$, and provides high accuracy for weakly scattering media.

2.2.2 Relaxation absorption and perfectly matched layers

Frequency-dependent attenuation and perfectly matched layer (PML) boundary conditions are incorporated into the 2-D first-order k -space method [9] based on the procedure presented in [18] for a finite-difference method. The frequency-dependent attenuation is accurately modeled using an N th-order relaxation model in which the compressibility is written as [19]:

$$\kappa(r, t) = \kappa_\infty(r)\delta(t) + \sum_{i=1}^N \frac{\kappa_i(r)}{\tau_i(r)} e^{-t/\tau_i(r)} H(t) \quad (2.6)$$

where $\kappa_\infty(r)$ is the compressibility as frequency approaches infinity and is equal to $1/[\rho(r)c(r)^2]$, $\delta(t)$ is the Dirac delta function, and $H(t)$ is the Heaviside step function. To obtain a specific value of the attenuation coefficient, appropriate values must be selected for $\tau_i(r)$, the relaxation time for the i th-order relaxation process, and $\kappa_i(r)$, the modulus for the i th-order relaxation process.

The PML medium, which is an artificial region that surrounds the propagation medium to provide absorbing boundary conditions, is incorporated in the first-order k -space method using nonphysical equations that introduce large direction-dependent attenuation in the PML region without producing significant reflections from the PML medium [20]. Direction-dependent attenuation is modeled by decomposing the total pressure field into artificial components associated with each spatial dimension.

The resulting 3-D acoustic field equations that incorporate relaxation absorption and PML boundary conditions are given by [9, 18]:

$$\rho(r) \left(\frac{\partial u_\zeta(r, t)}{\partial t} + \alpha_\zeta(r) u_\zeta(r, t) \right) = -\frac{\partial p(r, t)}{\partial \zeta} \quad (2.7)$$

$$\kappa(r, t) * \left(\frac{\partial p_\zeta(r, t)}{\partial t} + \alpha_\zeta(r) p_\zeta(r, t) \right) = -\frac{\partial u_\zeta(r, t)}{\partial \zeta} \quad (2.8)$$

Separately substituting each of the three spatial dimension variables for ζ yields six coupled first-order propagation equations. In Eq. 2.8, $p(r, t) = p_x(r, t) + p_y(r, t) + p_z(r, t)$ is an artificial decomposition of the scalar $p(r, t)$ into x , y , and z components, respectively, $\kappa(r, t)$ is the compressibility given in Eq. 2.6, $*$ denotes the convolution in time, and $\alpha_x(r)$, $\alpha_y(r)$, and $\alpha_z(r)$ are dispersionless attenuation parameters introduced to produce nonphysical attenuation in the PML region.

The values of the dispersionless attenuation parameters $\alpha_x(r)$, $\alpha_y(r)$, and $\alpha_z(r)$ are computed using:

$$\alpha_\zeta(r) = \begin{cases} f_\zeta(r), & \text{for } \zeta < M_\zeta \\ f_\zeta(r), & \text{for } \zeta > L_\zeta - M_\zeta \\ 0, & \text{otherwise} \end{cases} \quad (2.9)$$

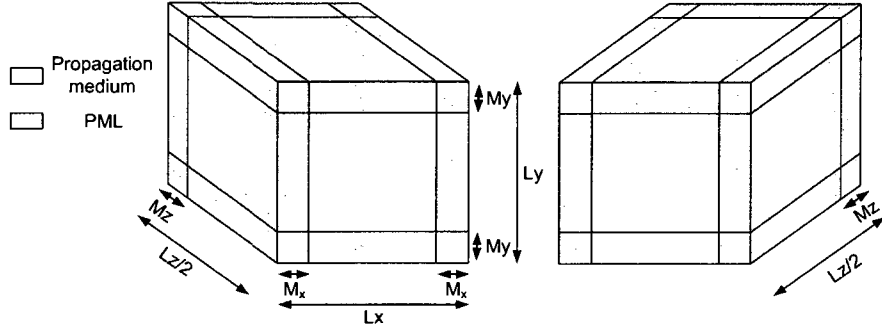


Fig. 2.1: The simulation grid divided into two parts showing the configuration of the dispersionless attenuation parameters, where L_x , L_y , and L_z are the dimensions of the simulation grid including the propagation medium and the PML region, and M_x , M_y , and M_z are the dimensions of the PML region.

where the functions f_x , f_y , and f_z return the values of $\alpha_x(r)$, $\alpha_y(r)$, and $\alpha_z(r)$, respectively, within the PML region and M_x , M_y , and M_z are the dimensions of the PML region as shown in Fig. 2.1. The dispersionless attenuation parameters are set to zero within the physical propagation medium, so the propagation equations constructed using Eq. 2.7 and Eq. 2.8 can describe the acoustic propagation in the PML region and the propagation medium.

The explicit evaluation of the temporal convolution in Eq. 2.8 leads to an inefficient algorithm. Following the simplifying procedure used in [18] and [9], the equations that involve temporal convolution can be converted to a system of simultaneous differential equations that do not include convolution. The simplification is achieved by introducing an artificial state variable for each relaxation process. The state variable that corresponds to the i th-order relaxation process is given by [9]:

$$S_i^\zeta(r, t) = \left(\frac{e^{-t/\tau_i(r)}}{\tau_i(r)} H(t) \right) * p_\zeta(r, t) \quad (2.10)$$

The equation that describes the dynamics of the state variables can be written as [18]:

$$\frac{\partial S_i^\zeta(r, t)}{\partial t} + \frac{1}{\tau_i(r)} S_i^\zeta(r, t) = \frac{p_\zeta(r, t)}{\tau_i(r)} \quad (2.11)$$

Based on the simplifying procedure described in [9], Eq. 2.8 can be expressed as:

$$\frac{\partial p_\zeta(r, t)}{\partial t} + \mu_\zeta(r)p_\zeta(r, t) = -\frac{1}{\kappa_\infty(r)} \left(\frac{\partial u_\zeta(r, t)}{\partial \zeta} - \sum_{i=1}^N \nu_i^\zeta(r) S_i^\zeta(r, t) \right) \quad (2.12)$$

where

$$\mu_\zeta(r) = \frac{1}{\kappa_\infty(r)} \sum_{i=1}^N \frac{\kappa_i(r)}{\tau_i(r)} + \alpha_\zeta(r) \quad (2.13)$$

and

$$\nu_i^\zeta(r) = \frac{\kappa_i(r)}{\tau_i(r)} - \kappa_i(r)\alpha_\zeta(r) \quad (2.14)$$

The continuous field equations of the 3-D first-order k -space method can be constructed from Eq. 2.7, Eq. 2.11, and Eq. 2.12 that advance the velocity, state variable, and total pressure fields, respectively. Discrete formulation of these equations can be achieved by using the time-staggered discretization procedure given in [9], which is based on the procedure presented in [18] for the finite-difference method, and employing the first-order k -space operators, given in Eq. 2.4, to evaluate the spatial derivatives and apply the temporal correction terms. Hence, the discrete field equations are given by:

$$\begin{aligned} u_x(r^x, t^+) &= e^{-\alpha_x(r^x)\Delta t/2} [e^{-\alpha_x(r^x)\Delta t/2} u_x(r^x, t^-) \\ &\quad - \frac{\Delta t}{\rho(r^x)} \left(\frac{\partial(p_x(r, t) + p_y(r, t) + p_z(r, t))}{\partial(c_0\Delta t)^+ x} \right)] \\ u_y(r^y, t^+) &= e^{-\alpha_y(r^y)\Delta t/2} [e^{-\alpha_y(r^y)\Delta t/2} u_y(r^y, t^-) \\ &\quad - \frac{\Delta t}{\rho(r^y)} \left(\frac{\partial(p_x(r, t) + p_y(r, t) + p_z(r, t))}{\partial(c_0\Delta t)^+ y} \right)] \\ u_z(r^z, t^+) &= e^{-\alpha_z(r^z)\Delta t/2} [e^{-\alpha_z(r^z)\Delta t/2} u_z(r^z, t^-) \\ &\quad - \frac{\Delta t}{\rho(r^z)} \left(\frac{\partial(p_x(r, t) + p_y(r, t) + p_z(r, t))}{\partial(c_0\Delta t)^+ z} \right)] \end{aligned} \quad (2.15a)$$

$$\begin{aligned}
p_x(r, t + \Delta t) &= e^{-\mu_x(r)\Delta t/2} [e^{-\mu_x(r)\Delta t/2} p_x(r, t) \\
&\quad - \frac{\Delta t}{\kappa_\infty(r)} \left\{ \frac{\partial u_x(r^x, t^+)}{\partial (c_0 \Delta t)^{-x}} - \sum_{i=1}^N \nu_i^x(r) S_i^x(r, t^+) \right\}] \\
p_y(r, t + \Delta t) &= e^{-\mu_y(r)\Delta t/2} [e^{-\mu_y(r)\Delta t/2} p_y(r, t) \\
&\quad - \frac{\Delta t}{\kappa_\infty(r)} \left\{ \frac{\partial u_y(r^y, t^+)}{\partial (c_0 \Delta t)^{-y}} - \sum_{i=1}^N \nu_i^y(r) S_i^y(r, t^+) \right\}] \\
p_z(r, t + \Delta t) &= e^{-\mu_z(r)\Delta t/2} [e^{-\mu_z(r)\Delta t/2} p_z(r, t) \\
&\quad - \frac{\Delta t}{\kappa_\infty(r)} \left\{ \frac{\partial u_z(r^z, t^+)}{\partial (c_0 \Delta t)^{-z}} - \sum_{i=1}^N \nu_i^z(r) S_i^z(r, t^+) \right\}]
\end{aligned} \tag{2.15b}$$

$$\begin{aligned}
S_i^x(r, t^+) &= e^{-\frac{\Delta t}{2\tau_i(r)}} [e^{-\frac{\Delta t}{2\tau_i(r)}} S_i^x(r, t^-) + \frac{\Delta t}{\tau_i(r)} p_x(r, t)] \\
S_i^y(r, t^+) &= e^{-\frac{\Delta t}{2\tau_i(r)}} [e^{-\frac{\Delta t}{2\tau_i(r)}} S_i^y(r, t^-) + \frac{\Delta t}{\tau_i(r)} p_y(r, t)] \\
S_i^z(r, t^+) &= e^{-\frac{\Delta t}{2\tau_i(r)}} [e^{-\frac{\Delta t}{2\tau_i(r)}} S_i^z(r, t^-) + \frac{\Delta t}{\tau_i(r)} p_z(r, t)]
\end{aligned} \tag{2.15c}$$

Equation 2.15 employs 3-D staggered-space and staggered-time schemes in which the temporal and spatial sampling of the total pressure and velocity fields are configured as shown in Fig. 2.2. The state variables are evaluated using staggered-time and regular-spatial schemes similar to that of the velocity and total pressure fields, respectively. This 3-D staggered scheme is equivalent to the 2-D staggered scheme

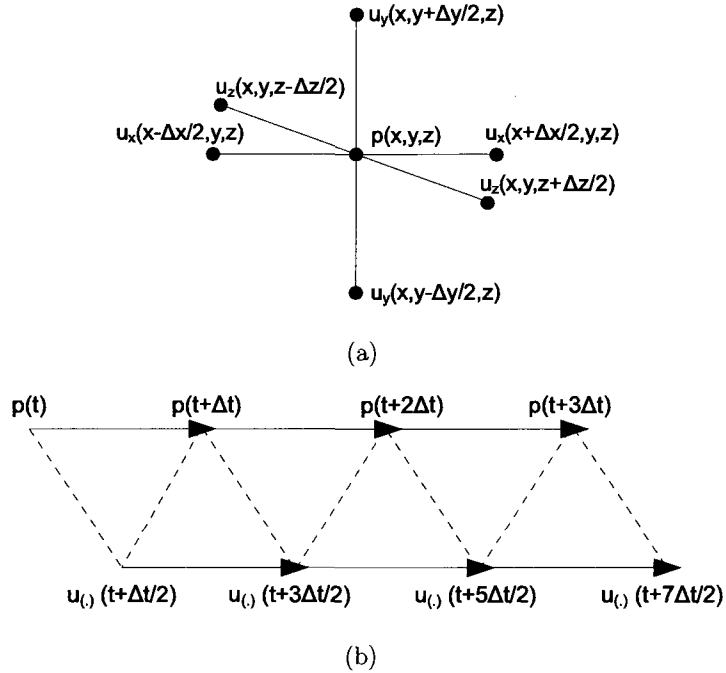


Fig. 2.2: (a) Staggered-space and (b) staggered-time sampling configuration of the total pressure and velocity fields.

used in [9]. The $(c_0\Delta t)^-$ and $(c_0\Delta t)^+$ operators are combined in a way that satisfies the sampling layout of the acoustic fields.

The use of the staggered-space and staggered-time configurations along with the temporal correction factor improve the stability and accuracy of the first-order k -space method given in Eq. 2.15. This k -space method enables an exact temporal iteration without dispersion for homogenous propagation media, and provides high accuracy for weakly scattering media, such as soft tissue. Moreover, this method provides unconditional numerical stability for media with $c(r) \leq c_0$, where c_0 is the sound speed used to compute the temporal correction factor [9].

Equation 2.15 requires evaluation of 4 forward and 6 inverse spatial Fourier transforms at each time step. The 3-D spatial Fourier transform is therefore the most significant computational task in a 3-D k -space simulation. The algorithm also re-

quires sufficient memory to store 12 field variables (i.e., 3-D pressure and particle velocity fields plus state variables for relaxation absorption) and about 15 acoustic parameters (e.g., density and compressibility plus parameters for relaxation absorption and perfectly matched boundary layers) at each point on the computation grid.

2.3 Parallel implementation

A distributed-memory computer cluster is a group of m nodes, where each node has its own processor and memory. The nodes are connected by an interconnection network and are assumed to have comparable performance. In this chapter, the phrase *computer clusters* refers specifically to distributed-memory clusters.

Executing an application on a computer cluster requires decomposing the application into a set of parallel tasks and assigning each task to one of the nodes in the cluster. Typically, the interactions between tasks are accomplished using the message passing model [21], in which tasks running on different nodes communicate by sending and receiving messages. Since the intra-node bus speed is much higher than the speed of the interconnection network, there is a tradeoff between the speedup gained through parallelization and the inter-node communication overhead that occurs when tasks allocated to different nodes exchange data. An efficient distribution of the tasks of a parallel application between the nodes of a computer cluster is one that minimizes the total running time, or parallel execution time, of the application.

2.3.1 Parallel simulation of a single scan line

Temporal propagation of the acoustic fields using Eq. 2.15 depends upon the local values of the fields and the values returned by the k -space operators at each grid point. Computing the k -space operators given in Eq. 2.4 involves computing the 3-D spatial Fourier transform of the acoustic fields, updating the transformed fields at each spatial frequency, and computing the 3-D inverse spatial Fourier transform of the updated

fields. All computations of the first-order k -space method, except the transforms between the spatial domain and the spatial frequency domain, are performed locally at each grid point without interacting with other points. Local evaluation in the spatial frequency domain is possible under the assumption of linear propagation, such that the pressure and velocity fields at a particular spatial frequency depend only the properties of the medium and the histories of the fields at that frequency. Global evaluation of the wave equation on the entire computation grid is enabled using the 3-D spatial Fourier transforms such that each point in the spatial frequency domain includes contributions from all grid points in the spatial domain, and vice versa.

Our parallel implementation of the first-order k -space method partitions the 3-D simulation grid evenly along one of the spatial dimensions and assigns each partition to one of the nodes in the cluster. Partitioning the grid enables large-scale simulations by employing the memory and processing resources of multiple nodes, and even distribution of the grid among nodes improves the computation efficiency by reducing the idle time of the nodes. One-dimensional (1-D) decomposition simplifies coarse partitioning of the grid, compared to 2-D and 3-D decompositions, and therefore helps minimize inter-node communications that take place during spatial Fourier transforms. The 3-D spatial Fourier transforms are evaluated using a parallel implementation of a fast Fourier transform (FFT) library, FFTW [22], that runs on computer clusters using the Message Passing Interface (MPI) [23] standard. The FFTW library uses 1-D decomposition. The number of grid partitions must be less than or equal to the number of available nodes. Given the grid sizes of realistic imaging simulations and the number of nodes of typical clusters, it is worth noting that running a single scan line on multiple nodes should always reduce the running time of the simulation.

2.3.2 Parallel simulation of multiple scan lines

In ultrasound imaging simulations that require computation of many scan lines, an efficient parallelization is achieved by computing multiple scan lines concurrently. However, a fixed number of nodes in a cluster produces a tradeoff between the number of nodes allocated to a single scan line and the number of scan lines run concurrently. Since the scan lines are independent from each other, running multiple scan lines concurrently does not introduce additional communication overhead, and hence improves the efficiency of the simulation. On the other hand, assigning multiple nodes to a single scan line reduces the simulation efficiency because data transfer operations between nodes take place at each simulation step. Allocation of multiple nodes to run single scan lines is required when the simulation involves large computation grids in order to ensure sufficient memory and processing resources. In the unusual case where the number of available nodes is greater than the number of scan lines, allocation of multiple nodes to single scan lines reduces the total running time of the simulation.

The dynamic scan-line allocation algorithm outlined in Fig. 2.3 was developed to achieve efficient parallel imaging simulations. The inputs of the algorithm are η , ξ , and β , which are the minimum number of nodes to be allocated for a single scan line, the total number of scan lines, and the number of grid points along the direction of 1-D decomposition, respectively. The value of η is chosen based on the memory and processing requirements of simulating a single scan line and should be an integer factor of the computation grid size along the decomposition dimension. The buffer Q stores a group of scan lines. The functions used in the algorithm are:

- **Number_Of_Available_Nodes()**: a function that returns the number of available nodes in the cluster.
- **Load_Scan_Lines(n)**: a function that returns n scan lines from the pool of unexecuted scan lines.
- **Find_Integer_Multiple($n1, n2$)**: a function that returns the largest integer

```

Distribute_Scan_Lines ( $\xi, \eta, \beta$ )
 $\xi' = \xi$ 
while  $\xi' > 0$  and Number_Of_Available_Nodes()  $\geq \eta$  do
   $m' = \text{Number\_Of\_Available\_Nodes}()$ 
  if  $\lfloor \frac{m'}{\eta} \rfloor \leq \xi'$  then
     $Q = \text{Load\_Scan\_Lines}(\lfloor \frac{m'}{\eta} \rfloor)$ 
     $\gamma = \text{remainder}\{\frac{m'}{\eta}\}$ 
    while Size( $Q$ )  $> 0$  do
       $\vartheta = \text{Find\_Integer\_Multiple}(\beta, \eta + \gamma)$ 
       $\gamma = \eta + \gamma - \vartheta$ 
      Assign_Nodes( $Q, \vartheta$ )
    end while
     $\xi' = \xi' - \lfloor \frac{m'}{\eta} \rfloor$ 
  else
     $Q = \text{Load\_Scan\_Lines}(\xi')$ 
     $\gamma = \text{remainder}\{\frac{m'}{\xi'}\}$ 
    while Size( $Q$ )  $> 0$  do
       $\vartheta = \text{Find\_Integer\_Multiple}(\beta, \lfloor \frac{m'}{\xi'} \rfloor + \gamma)$ 
       $\gamma = \lfloor \frac{m'}{\xi'} \rfloor + \gamma - \vartheta$ 
      Assign_Nodes( $Q, \vartheta$ )
    end while
     $\xi' = 0$ 
  end if
end while

```

Fig. 2.3: An algorithm for distributing the scan lines between the nodes of a cluster. The $\lfloor \cdot \rfloor$ operator denotes rounding down to the nearest integer.

that is smaller than n_2 and divides n_1 evenly.

- **Assign_Nodes**(Q, n): a function that assigns n nodes to execute one scan line in Q . The executed scan line is removed from Q .

This allocation algorithm assigns the largest possible number of scan lines to the available nodes in a way that satisfies the constraint of a user-specified minimum number of nodes per single scan line and reduces the idle time of the nodes. The computation gird of each scan line is distributed equally between its assigned group

of nodes. When nodes become available, the algorithm iteratively allocates new scan lines to the available nodes. Therefore, this algorithm enables efficient scheduling of scan lines on a cluster for all combinations of number of scan lines, number of cluster nodes, and minimum number of nodes per scan line.

Consider an example imaging simulation with six scan lines run on a cluster of eight nodes, and assume that the simulation grid size of each scan line is $512 \times 512 \times 512$ points and the minimum number of nodes per scan line is two. At the beginning of the simulation, the allocation algorithm loads four scan lines for simulation and assigns two nodes to run each scan line. When the simulation of the first four scan lines is completed, the algorithm assigns four nodes to run each of the two remaining scan lines.

2.4 Numerical methods

Test computations were carried out to identify the best combination of spatial and time step sizes to achieve accurate B-mode imaging simulations while also reducing the computational complexity. An important finding in [9] is that the 2-D first-order k -space method achieves accurate computations using a grid spacing of four points per minimum wavelength and a time step chosen such that the CFL number [13], defined as $CFL = \frac{c_0 \Delta t}{\Delta x}$, is equal to 0.5. The example computations described in the following sections evaluate whether those guidelines for choosing a grid spacing and time step, which are hereafter referred to as the typical k -space configuration, remain applicable when the k -space method is used to compute 3-D propagation of the total pressure in the high-frequency band and a Gaussian spatial filter, rather than the half-band filter employed in [9], is used to smooth the acoustic properties of the medium. These example computations provide a framework for analyzing the computational complexity of a realistic B-mode imaging simulation based on a consideration of the complexity of a single k -space simulation. Additional calculations are then performed

to determine the most efficient allocation of parallel computing resources for B-mode imaging simulations. Moreover, an aperture-projection algorithm is presented that permits the computations to be limited to a small field of view around the focus. An example imaging simulation is performed to demonstrate the feasibility of fast 3-D imaging simulations using the aperture-projection algorithm and parallel computing.

A 3-D Gaussian filter provides a practical means, compared to the half-band filter, for smoothing the propagation media of imaging simulations in order to reduce numerical artefacts that can result from applying the k -space method to a medium that contains discontinuities. In this chapter, spatially-dependent sound speed and mass density are smoothed using the Gaussian filter given by:

$$\Psi(k) = e^{-\sigma^2 k^2} \quad (2.16)$$

This filter, which is applied in the spatial frequency domain, reduces numerical errors associated with medium discontinuities without introducing significant blurring artefacts when $\sigma = \frac{3\Delta x}{2\pi}$.

The incident pulse used in sections 2.4.1, 2.4.2, and 2.4.3 is a plane wave with a Gaussian envelope, a centre frequency of 40 MHz, and -6 -dB bandwidth of 24 MHz. This is a typical frequency spectrum used for the focused pulses employed for small-animal imaging in preclinical research. The maximum frequency of the incident pulse, which is used to calculate the size of the spatial step, is taken as 70.9 MHz, corresponding to the upper -40 -dB frequency of the pulse spectrum.

The dispersionless attenuation parameters of the PML boundary conditions are set to increase smoothly from the inner surface to the outer surface of the PML region using equation (27) in [9]. The maximum PML absorption per grid point is fixed at 3 Np and the thickness of the PML region is set to 10 points. These settings produce boundary reflection and transmission coefficients less than -100 dB for normally incident waves.

2.4.1 Analysis of numerical accuracy and computational complexity: Propagation calculations

A benchmark calculation is performed in which the total field after forward scattering from a fluid sphere of diameter 0.24 mm ($\sim 6\lambda$) is computed and compared with an analytical solution [24]. The sphere, which is located at the origin, has the acoustic properties of fat ($c = 1.478$ mm/ μ s and $\rho = 0.950$ g/cm³) [25] and is embedded in a water background at body temperature ($c = 1.524$ mm/ μ s and $\rho = 0.993$ g/cm³) [25]. The size of the sphere is comparable to the size of the smallest tumour detectable using 3-D high-frequency ultrasound imaging [26]. The centre of the incident pulse is initially located at $y_0 = -0.3$ mm and the pulse is propagated along the positive y (axial) direction. The total pressure field is recorded at 45 observation points extending 0.48 mm along the x (lateral) coordinate, with the central point placed at $x = 0$, $y = 0.24$, and $z = 0$ mm.

The accuracy of the simulation is evaluated using the frequency-domain L^2 error given by:

$$\epsilon = \frac{\|\hat{p}_{num} - p_{exact}\|}{\|p_{exact}\|} \quad (2.17)$$

where $\|\cdot\|$ is the L^2 norm of a matrix [27] and \hat{p}_{num} and p_{exact} are matrices composed of all computed frequency components of the total pressure recorded at the observation points using the k -space method and the analytical solution, respectively.

The results are presented as graphs of L^2 error as a function of the computational complexity of the simulation. Two graphs are constructed. One graph shows the effect of varying the grid spacing from 2 to 12 points per minimum wavelength, incrementing by multiples of 2, while also adjusting the time step to maintain a fixed CFL number of 0.5. The second graph shows the effect of varying the time step such that the CFL number ranges from 0.1 to 1.3 in increments of 0.1, while maintaining a fixed spatial step of 4 points per minimum wavelength. The computational complexity is normalized by the complexity of a simulation using the typical choices of spatial and

time steps for the first-order k -space method. Therefore, the normalized complexity is directly proportional to the total number of points in the 3-D grid multiplied by the number of temporal iterations. The analysis thus shows the joint effect on accuracy and computational complexity of deviating from the typical recommended grid spacing and time step. For all results reported in this chapter, an isotropic spatial step is used, *i.e.* $\Delta x = \Delta y = \Delta z$. For the range of CFL numbers examined in this study, the k -space method did not suffer from any numerical instability, which agrees with the theoretical unconditional stability of this method for a medium with $c(r) \leq c_0$ [6, 9].

2.4.2 Analysis of numerical accuracy and computational complexity: Attenuation calculations

Computational complexity is also analyzed by studying the effect of the complexity on the fidelity with which the relaxation absorption model simulates linear frequency dependence of attenuation in the high-frequency band. Four attenuation coefficients are modeled: 0.695, 0.869, 1.040, and 0.805 dB/cm/MHz, which match the acoustic attenuation of bovine liver, myocardium, and kidney [28], and whole cells [29], respectively in the high-frequency band. For each attenuation coefficient, the incident pulse is propagated in a homogeneous medium with the sound speed and mass density of water at body temperature. Other sound speeds and densities are not examined since their values do not affect the attenuation results.

Linear frequency dependence of attenuation is approximated using the relaxation absorption model with two processes. The parameters of the relaxation processes are determined using a curve fitting procedure that minimizes the mean squared error between the desired linear frequency-dependent absorption and the analytical relaxation absorption as a function of frequency given by [19]:

Table 2.1: Relaxation absorption parameters to model frequency-dependent absorption

| | α (dB/cm/MHz) | τ_1 (ns) | τ_2 (ns) | κ_1 ($\times 10^{-4}\kappa_\infty$) | κ_2 ($\times 10^{-4}\kappa_\infty$) | $c(f)^*$ (mm/ μ s) |
|-------------|-------------------------|------------------|------------------|---|---|---------------------------|
| Liver | 0.695 | 2.1 | 21 | 62 | 73 | [1.5171, 1.5214] |
| Myocardium | 1.040 | 2.2 | 22 | 93 | 108 | [1.5139, 1.5203] |
| Kidney | 0.869 | 2.1 | 21 | 77 | 91 | [1.5154, 1.5208] |
| Whole Cells | 0.805 | 2.1 | 21 | 71 | 84 | [1.5161, 1.5210] |

* The values of $c(f)$ are shown as a closed interval with the lower and upper endpoints computed at 9.1 and 70.9 MHz, respectively.

$$\alpha_{abs}(f) = (2\pi f) \sqrt{\frac{\rho(r)}{2}} \left\{ -\kappa_\infty(r) - \sum_{i=1}^N \frac{\kappa_i(r)}{1 + \tau_i^2(r)(2\pi f)^2} + [(\kappa_\infty(r) + \sum_{i=1}^N \frac{\kappa_i(r)}{1 + \tau_i^2(r)(2\pi f)^2})^2 + (\sum_{i=1}^N \frac{2\pi f \kappa_i(r) \tau_i(r)}{1 + \tau_i^2(r)(2\pi f)^2})^2]^{0.5} \right\}^{0.5} \quad (2.18)$$

The curve fitting procedure is run over all frequency components within -40 dB from the centre frequency in the pulse spectrum. The values of the relaxation parameters for each medium are listed in Table 2.1. The range of the analytical frequency-dependent sound speed [19], $c(f)$, of each medium is computed for all frequency components within -40 dB from the centre frequency in the pulse spectrum and is also presented in Table 2.1. Within this frequency range, $c(f)$ is a monotonically increasing function of frequency.

The incident pulse is propagated using a spatial step size of four points per minimum wavelength and two CFL numbers, 0.5 and 0.25, which correspond to the typical computational complexity defined in section 2.4.1 and double the typical complexity, respectively. The simulated relaxation absorption is measured by computing the ratio of pressure spectra received at ten observation points located along the propagation axis, where the distance between two successive points is 0.054 mm. The analytical (equation 2.18) and simulated relaxation absorptions are compared with the desired linear frequency-dependent absorption by plotting the difference between the desired

absorption and the relaxation absorptions as a function of frequency.

2.4.3 Parallel simulation performance

The reduction of execution time achieved by distributing the computational tasks of the k -space method between a group of cluster nodes is evaluated. This evaluation uses fixed spatial and time steps corresponding to the typical configuration of CFL number equal to 0.5 and 4 grid points per minimum wavelength. The spatial and time steps are set to $5.21 \mu\text{m}$ and 1.71 ns , respectively.

To evaluate the performance of computing a single scan line in parallel, the incident pulse is propagated along the y direction in a homogeneous medium with the acoustic properties of fat. The simulation is run for 1000 time steps, which allows the pulse to travel 2.5 mm. The 3-D computation grid is composed of $N_x \times N_y \times N_z$ points, where N_x , N_y , and N_z are the number of grid points along the x , y , and z directions. In this test, the values of N_x and N_y are fixed at 512 points and the value of N_z is varied between 16 and 512 points, incrementing by multiples of two. The number of nodes used is varied from 1 to 64, incrementing by multiples of two. The execution times of the parallel and serial simulations are reported as means of four simulation trials.

The measured execution times for single scan lines are used to compute the serial and parallel execution times of B-mode simulations with the number of scan lines varied from 4 to 512, incrementing by multiples of two, and the minimum number of nodes per scan line set to 1, 2, 4, 8, or 16. Parallel execution times are computed assuming 64 nodes are available, each scan line uses a $512 \times 512 \times 512$ grid, and the scan lines are allocated according to the algorithm introduced in section 2.3.2.

The speedup and efficiency [30] are used to evaluate the performance of parallel computing. The speedup is the ratio of the execution time of the serial simulation to that of the parallel simulation. The efficiency is the ratio of the speedup to the number of nodes used.

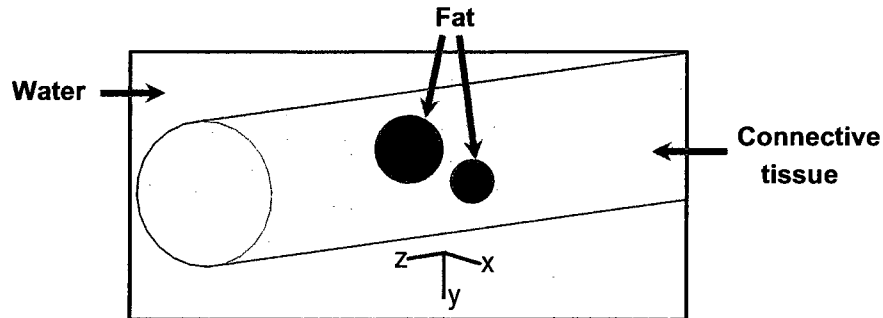


Fig. 2.4: A schematic representation of a tissue-mimicking phantom composed of an infinite-length cylinder of diameter 1.7 mm with acoustic properties of connective tissue containing two internal spheres of diameters 0.5 and 0.4 mm with acoustic properties of fat and is surrounded by a background medium with acoustic properties of water at body temperature. The orientation of the x , y , and z axes are as shown in the figure, but the origin is located inside the phantom as described in the text.

2.4.4 B-mode imaging simulations

An example B-mode imaging simulation of a tissue-mimicking phantom is carried out to demonstrate the feasibility of 3-D imaging studies using parallel computing. The phantom (Fig. 2.4) is composed of an infinite-length cylinder of diameter 1.7 mm with acoustic properties of connective tissue ($c = 1.550 \text{ mm}/\mu\text{s}$ and $\rho = 1.040 \text{ g}/\text{cm}^3$) [31] containing two internal spheres of diameters 0.5 and 0.4 mm with acoustic properties of fat. The cylinder is surrounded by a background medium with acoustic properties of water at body temperature. The axis of the cylinder is aligned along the z -axis (elevation) and the centres of the spheres are located on the xy plane ($z = 0$). Random scatterers are added to the cylinder and the spheres as random fluctuations in compressibility using a Gaussian random variable with rms amplitude of 1% and 5% of their compressibility, respectively. Attenuation is ignored in this simulation.

We wish to simulate imaging with a highly focused circular transducer with a 2.3-mm diameter, a 6.0-mm focal distance, a 40-MHz centre frequency, and -6 -dB bandwidth of 24 MHz, which are similar to the specifications of the VisualSonics

RMV706 transducer (VisualSonics Inc., Toronto, Canada). Calculating propagation from the transducer to the focal zone would require a very large grid. The grid size can be reduced as follows by determining an equivalent aperture near the focal zone of the transducer and restricting the k -space simulation to a field of view around the focus. The lateral resolution (LR) and depth of field (DOF) of a transducer can be approximated by [32, 33]:

$$LR = \lambda \frac{F}{D} \quad (2.19)$$

$$DOF = 3\lambda \left(\frac{F}{D}\right)^2 \quad (2.20)$$

where F is the focal distance of the transducer and D is the transducer diameter. These equations can be used to specify a smaller aperture with a shorter focal distance that provides the same spatial resolution and depth of field as the modeled transducer. In this thesis, this approach is referred to as *aperture projection*. Equations 2.19 and 2.20 indicate that aperture projection involves simply matching the f -number ($\frac{F}{D}$) of the modeled transducer and the wavelength of the transmitted pulse. Therefore, the B-mode imaging simulations are performed using a projected aperture with a 0.47 mm diameter, a 1.23 mm focal distance, and the same centre frequency as the previous simulations. The projected aperture is located in a plane at $y = -1.23$ mm so the focus will be on the long axis of the cylindrical phantom. The focus is located on the xz plane ($y = 0$) and the pulse bandwidth is also the same as the previous simulations.

A set of parallel B-mode image planes are obtained at various z coordinates. Each image is composed of 65 scan lines that are equally-spaced by 40 μm along the x direction. The simulation of each scan line is carried out using a computation grid of $128 \times 512 \times 128$ points, a spatial step of 5 μm , and a time step of 1.64 ns (CFL = 0.5). Each B-mode image is computed using 20 nodes, such that the first 60 scan lines are simulated by allocating two nodes for each scan line, while the simulation of the last five scan lines is performed using four nodes for each scan line.

2.4.5 Computer cluster specifications

The serial and parallel ultrasound simulations presented in this study are run on a computer cluster in SHARCNET (<http://www.sharcnet.ca>). Each node has an Opteron single core 2.4 GHz processor, 32 GB memory, Quadrics Elan4 interconnects, and runs the HP XC 3.1 Linux-based system. Groups of four processor nodes are in close communication, so computations using four or fewer nodes have minimal inter-node communication overhead.

2.5 Numerical results

2.5.1 Analysis of numerical accuracy and computational complexity: Propagation calculations

Accuracy results of the fluid sphere benchmark problem are presented in Fig. 2.5 as a function of the computational complexity normalized by the complexity of a simulation using the typical k -space configuration of CFL number equal to 0.5 with 4 grid points per minimum wavelength. Fig. 2.5(a) shows the joint effect on the L^2 error and the computational complexity when the spatial step is fixed at 4 points per minimum wavelength and the time step is varied. The complexity is inversely proportional to the time step because Δx is held constant. The L^2 error at a normalized complexity of 1 is 2.6%, which is judged to be sufficient accuracy for B-mode imaging simulations. The L^2 error increases rapidly when a time step coarser than the typical configuration, corresponding to normalized complexity less than 1, is used. On the other hand, the additional reduction in L^2 error achieved by using finer time steps than the typical configuration is small relative the corresponding increase in the complexity.

Fig. 2.5(b) shows the joint effect on the L^2 error and the computational complexity when the spatial step is varied from the typical configuration of 4 grid points per

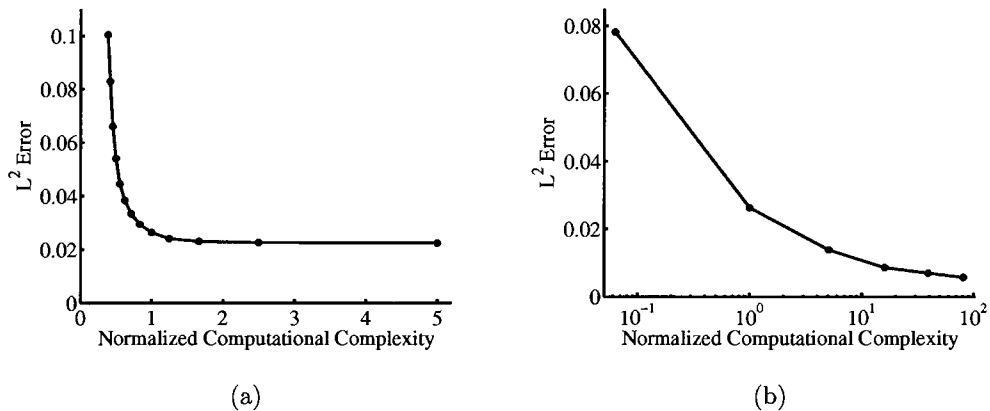


Fig. 2.5: Frequency-domain L^2 error of the 3-D k -space method as a function of normalized computational complexity when (a) the CFL number is varied between 0.1 and 1.3 and the spatial step is set to 4 points per minimum wavelength, and (b) the CFL number is set to 0.5 and the spatial step is varied between 2 and 12 points per minimum wavelength.

minimum wavelength while also adjusting the time step to maintain CFL number equal to 0.5. Normalized complexity is plotted using a logarithmic scale in Fig. 2.5(b) for ease of visualization of the data points. Since the CFL number is proportional to $\frac{\Delta t}{\Delta x}$, to hold CFL constant when the spatial step is increased by a factor of a , the time step must also be scaled by a , which scales the number of temporal iterations by $\frac{1}{a}$. Since an isotropic spatial step is used, the number of spatial grid points is inversely proportional to $(\Delta x)^3$, so a large range of complexity values are covered in Fig. 2.5(b) because the complexity is effectively proportional to $(\Delta x)^{-4}$. Again, the L^2 error increases rapidly when the normalized complexity is reduced below 1. Note that the minimum normalized complexity for a homogeneous medium is $\frac{1}{16}$, which corresponds to 2 grid points per minimum wavelength. The additional reduction in L^2 error achieved by using finer spatial sampling than the typical configuration is very small relative to the corresponding increase in the complexity. Since the memory requirements also increase proportionally to $\frac{1}{(\Delta x)^3}$, the use of finer spatial sampling may also be limited by the available memory resources of the cluster. If a spatial

step finer than 4 points per minimum wavelength is required to preserve the features of the medium that otherwise will be lost during the discretization process, then the k -space method achieves a very small L^2 error when sufficient memory resources are available. For example, an error value of 0.57% is achieved using 12 points per minimum wavelength and a CFL number of 0.5, which corresponds to a normalized complexity of 81.

The relationship between the numerical accuracy of the 3-D first-order k -space method and spatial and time steps that can be induced from Fig. 2.5 agrees with Figs. 3 and 4 in [9] and Figs. 2 and 3 in [6] that characterize the numerical accuracy of computing scattering from a fluid cylinder using the 2-D first-order k -space method and the second-order k -space method, respectively. The three methods achieve a low error value on the order of 3% using a CFL number of 0.5 and four points per minimum wavelength.

2.5.2 Analysis of numerical accuracy and computational complexity: Attenuation calculations

The difference between the desired linear frequency-dependent absorption and the analytical (equation 2.18) and simulated relaxation absorptions is shown in Fig. 2.6 for liver, kidney, myocardium, and whole cells with acoustic properties given in Table 2.1. The analytical curves show that the second-order relaxation absorption model does not produce exactly linear frequency dependence of absorption, so the simulated absorption obtained in a k -space computation should not be expected to exhibit perfectly linear frequency dependence either. The curves for CFL numbers of 0.25, which correspond to computational complexity two times greater than the typical k -space configuration, closely match the frequency dependence of the analytical relaxation absorption model. Even though the absorption obtained using the typical k -space configuration (CFL = 0.5) exhibits greater deviation from linear frequency depen-

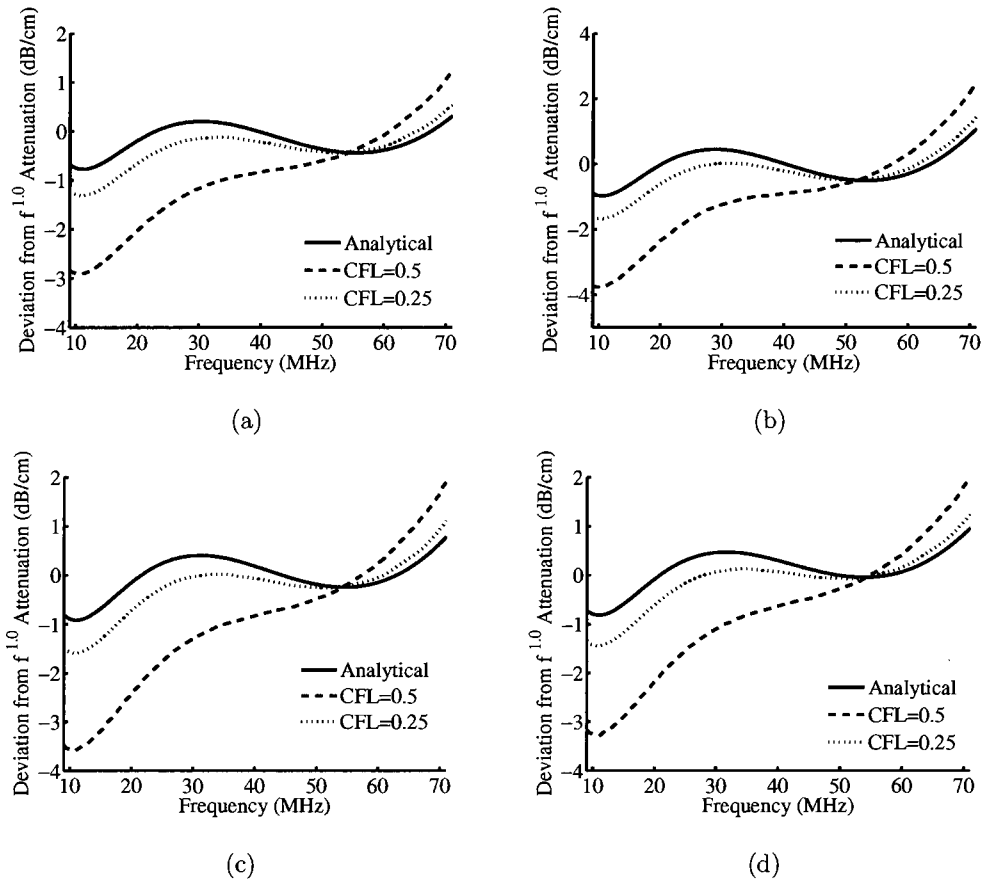


Fig. 2.6: Difference between the desired linear frequency-dependent absorption and the analytical and simulated relaxation absorptions for (a) liver, (b) kidney, (c) myocardium, and (d) whole cells with acoustic properties given in Table 2.1.

dence, this performance is judged satisfactory for B-mode imaging simulations. The discrepancy between relaxation absorption simulated at CFL numbers of 0.25 and 0.5 is at most 1.28 dB/cm at frequencies between 30 and 50 MHz where most of the pulse energy is concentrated. Note that 1 cm is a long propagation distance at 30 to 50 MHz.

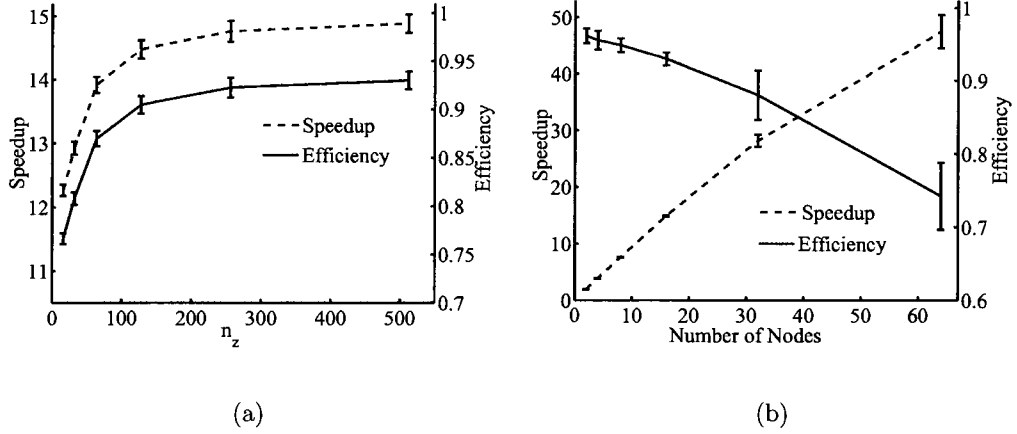


Fig. 2.7: Performance results achieved by partitioning the simulation grid of a single scan line. Speedup (dashed lines) and efficiency (solid lines) as functions of (a) the number of grid points along the z -axis with $N_x = N_y = 512$ using 16 nodes, and (b) the number of nodes for a $512 \times 512 \times 512$ grid.

2.5.3 Parallel simulation performance

Fig. 2.7(a) shows both the speedup and efficiency of simulating a single scan line in parallel as functions of grid size when the number of nodes is fixed at 16. The speedup and efficiency increase as the size of the simulation grid increases. Using 16 nodes, the maximum speedup of 14.88 ± 0.14 and efficiency of 0.930 ± 0.009 are achieved with the largest simulation grid ($512 \times 512 \times 512$ points).

The average speedup and efficiency of a single scan line with respect to number of nodes are shown in Fig. 2.7(b) for the case when the grid size is fixed at $512 \times 512 \times 512$ points (i.e., computational complexity held constant). When the size of the simulation grid is fixed, the speedup value increases as the number of nodes increases, but the efficiency tends to decrease as the number of nodes increases. This observation can be explained by the fact that, as the number of nodes increases, the computation grid is distributed among a larger number of nodes, leading to greater values of speedup, but the resulting higher communication overhead decreases the efficiency. Using a $512 \times 512 \times 512$ point grid, the maximum speedup of 47.52 ± 2.93 is obtained using

the maximum number of nodes tested (64), while the maximum efficiency of 0.961 ± 0.010 is achieved using two nodes.

The overall speedup values of B-mode imaging simulations are presented in Table 2.2 when the available number of nodes is equal to 64. Each cell in Table 2.2 shows the speedup of computing a B-mode image composed of the number of scan lines shown in the leftmost column when the minimum number of nodes per single scan line is equal to the value in the top row. When the product of the number of scan lines and the minimum number of nodes per single scan line is less than the total number of nodes, all scan lines can be run concurrently. In this case, the minimum number of nodes per single line does not affect the speedup because the scan-line allocation algorithm assigns a number of nodes greater than the user-specified minimum to each scan line. As the number of scan lines increases, the computation grid of each individual line is assigned to fewer nodes, leading to greater values of efficiency for each scan line and hence greater values of overall speedup.

As the number of scan lines increases further such that the number of available nodes is less than or equal to the product of the number of scan lines and the minimum number of nodes per scan line, the number of scan lines that can be run concurrently depends only on the user-specified minimum number of nodes per single line. This scenario applies to most B-mode imaging simulations unless the number of available nodes is very large. In this case, the overall speedup for a B-mode simulation is equal to the number of available nodes multiplied by the efficiency of computing a single scan line. For example, consider the effect of increasing the total number of scan lines from 4 to 8 when the minimum number of nodes per line is 16 and the number of available nodes is 64 as in Table 2.2. In the former case, all four lines execute concurrently with an efficiency of 0.930, so the overall speedup is $64 \times 0.930 = 59.52$. In the latter case, the total parallel execution time doubles (i.e., lines 1-4 execute concurrently, then lines 5-8 execute concurrently). Since the serial execution time also doubles when computing 8 lines compared to 4 lines, the total speedup achieved

Table 2.2: Speedup values of B-mode image simulations

| Number of scan lines | Minimum number of nodes per scan line | | | | |
|----------------------|---------------------------------------|-------|-------|-------|-------|
| | 1 | 2 | 4 | 8 | 16 |
| 4 | 59.52 | 59.52 | 59.52 | 59.52 | 59.52 |
| 8 | 60.72 | 60.72 | 60.72 | 60.72 | 59.52 |
| 16 | 61.17 | 61.17 | 61.17 | 60.72 | 59.52 |
| 32 | 61.52 | 61.52 | 61.17 | 60.72 | 59.52 |
| ≥ 64 | 64 | 61.52 | 61.17 | 60.72 | 59.52 |

by the parallel cluster relative to the serial computer is unchanged.

2.5.4 B-mode imaging simulations

The simulated B-mode images for the tissue mimicking phantom are shown in Fig. 2.8, where each panel presents a B-mode image plane obtained at a different elevation along the z -axis. The B-mode images show realistic 3-D refraction artefacts that appear as shadow regions below the spherical lesions. These artefacts are produced by the change in direction of the wave at the top and bottom of each lesion when the wave is obliquely incident to the sphere. Such 3-D artefacts cannot be obtained using 2-D simulations. The serial execution time required to compute each B-mode image was 357.50 hours, compared to the parallel execution time of 18.61 hours using 20 cluster nodes. These results suggest that the parallel 3-D k -space method can be used to perform realistic 3-D imaging studies with short running times.

2.6 Discussion

This chapter explores the issue of whether fully 3-D simulations of ultrasound imaging are practical using current computer technology. Tabei *et al.* [9] have shown that the 2-D total-pressure solver version of the first-order k -space method achieves high numerical accuracy using the typical configuration of CFL number equal to 0.5 with spatial sampling of 4 points per minimum wavelength when the propaga-

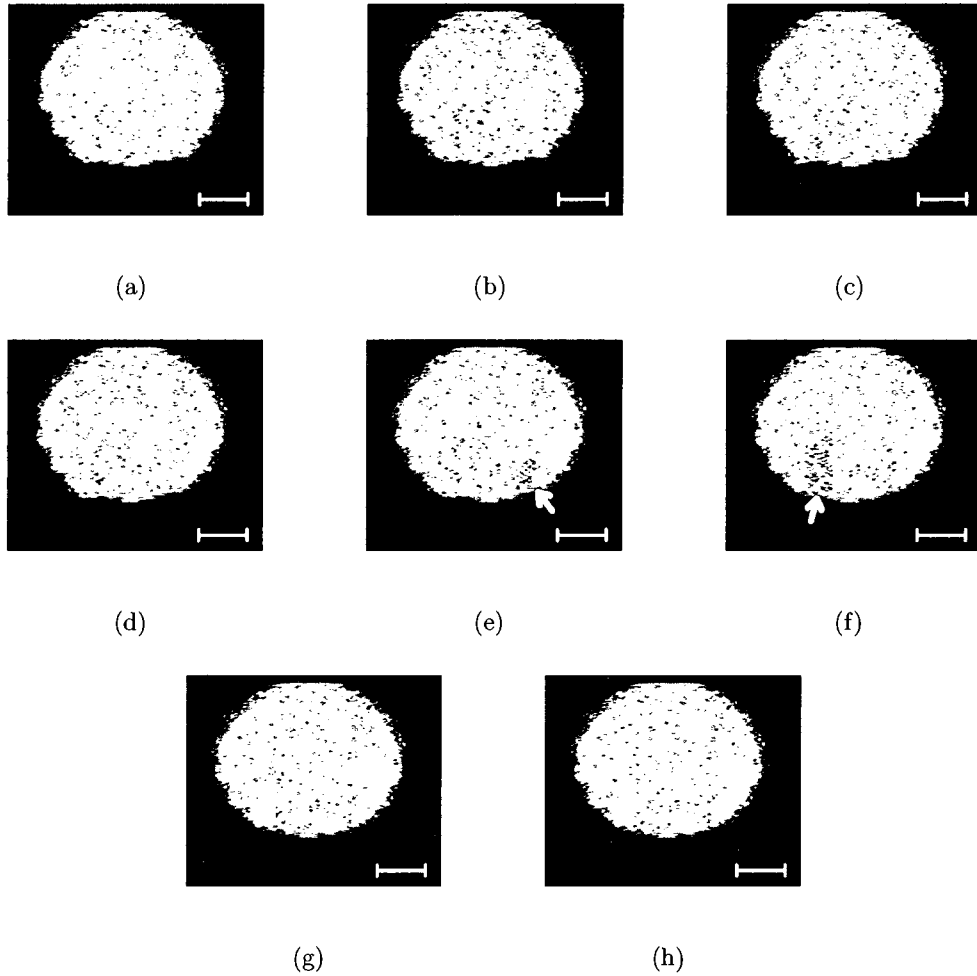


Fig. 2.8: Simulated B-mode images of a 3-D tissue mimicking phantom containing two spherical lesions of diameters 0.5 and 0.4 mm acquired when the focus of the transducer is located at $x = 0$, $y = 0$, and (a) $z = 0$, (b) $z = 0.05$, (c) $z = 0.10$, (d) $z = 0.15$, (e) $z = 0.20$, (f) $z = 0.25$, (g) $z = 0.30$, and (h) $z = 0.35$ mm. Panels (e) and (f) contain a shadow region with reduced brightness indicated with a white arrow. Scale bar = 0.5 mm.

tion medium is filtered using a half-band filter. The first-order k -space method is extended in section 2.2 to compute 3-D total pressure propagation. Numerical evaluations presented in section 2.5.1 show that the 3-D total-pressure solver with the typical configuration of spatial and time steps achieves a low error value of 2.6%

when the medium is filtered using a Gaussian filter. A Gaussian filter provides a practical method for smoothing the propagation medium in an imaging simulation, which typically includes structures with irregular geometries. Furthermore, section 2.5.1 demonstrates that the increase in computational complexity that results from using spatial and time steps finer than the typical configurations can be dramatic, especially when a grid spacing finer than 4 points per minimum wavelength is chosen. Moreover, using a finer grid spacing than the typical configuration greatly increases the memory requirements of a 3-D k -space simulation. Even when the typical configuration is used, the memory requirements for computing a single scan line in 3-D, as illustrated by the example outlined in the section 2.1, still exceed the capabilities of most contemporary serial computers and thus make a parallel implementation necessary.

In the context of B-mode imaging simulations, parallel computing provides the added benefit of enabling several scan lines to be computed concurrently. Parallel performance results summarized in Table 2.2 demonstrate that the most efficient use of parallel computing resources is to partition the computation grid for a single scan line among the smallest group of nodes that provides sufficient memory and employ multiple groups of nodes to run independent pulse-echo simulations concurrently. The parallel efficiency results shown in Fig. 2.7(b) for a single scan line demonstrate that the efficiency is high (close to 1) when four or fewer nodes are used, but the efficiency begins to decrease when more than four nodes are used. This result is attributed to the architecture of the interconnection network, in which the communication cost among each group of four processors is lower than the inter-group communication cost. The dynamic scan-line allocation algorithm introduced in Fig. 2.3 performs the recommended allocation automatically when the user sets the minimum number of nodes per scan line equal to the smallest number of nodes with sufficient total memory. High efficiency was achieved in the B-mode simulations in part because it was possible to allocate a minimum of only two nodes per scan line.

If simulated images with a small field of view are sufficient for the user's application, the size of the computation grid can be further reduced by using the aperture-projection technique outlined in section 2.4.4. This approach was applied to synthesize the images in Fig. 2.8. Each of those images, which consist of 65 scan lines, was synthesized in about 19 hours using a 20-node cluster with large memory (32 GB per node) in which the minimum number of nodes per scan line is set to two. The benefits of computing 3-D wave propagation, illustrated in Fig. 2.8 by the refraction artefacts from the spherical lesions, can be appreciable even in a small field of view simulation.

The linear frequency dependence of attenuation modeled in this paper is an approximation that is commonly used at clinical frequencies. Maruvada *et al.* [28] have shown that this approximation can be extended to the high-frequency band. As at clinical frequencies, a more accurate treatment of attenuation would include an f^x frequency dependence, where $1 < x < 2$ [34]. More complicated frequency dependence can be obtained in the k -space method by including higher order processes in the relaxation absorption model. Each additional relaxation process would require storage of three additional state variables and the associated medium parameters at each grid point as well as additional operations to update the pressure field at each time step.

Viewed collectively, the results presented in this chapter demonstrate that fully 3-D simulations of ultrasound imaging are practical provided the application does not require synthesis of a large number of images with fields of view comparable to a complete B-mode image. A reduced field of view should be perfectly acceptable for applications such as developing lesion detection or classification algorithms. Other applications, such as simulations of aberration and aberration correction, where it is essential to compute propagation over the entire distance from the transducer to the imaging target, can be performed using the 3-D k -space method, but the number of scan lines computed concurrently would be substantially restricted. In such cases,

the user may face a choice between synthesizing only a small number of images or reverting to calculations of 2-D propagation to reduce the grid size.

The B-mode execution times reported in this paper were achieved using a spatial step of about 4 points per minimum wavelength. Some applications may require finer spatial sampling to better preserve the detailed features of the medium. Quantitative high-frequency scattering simulations using models of the cellular-scale microstructure of tissue (e.g., chapter 3 of this thesis) are one example of an application where the spatial step may be dictated by the characteristics of the medium rather than the minimum requirements for k -space propagation accuracy.

2.7 Conclusion

This chapter extends the first-order k -space method to compute 3-D acoustic propagation and explores practical issues related to the use of the k -space method for 3-D ultrasound imaging simulations. The importance of 3-D simulations is illustrated by the refraction artefacts obtained in the B-mode images of Fig. 2.8. An algorithm was introduced to automatically allocate scan lines to the nodes of a computer cluster. Effective use of the scan-line allocation algorithm requires consideration of the computational resources available at each node. The parallel performance results demonstrate that 3-D simulations of B-mode imaging are most practical when the number of scan lines computed concurrently can be maximized. The finite resources of each cluster node impose a trade-off between the spatial step size, the dimensions of the field of view, and the running time of the simulation. Therefore, when determining the numerical accuracy desired for a specific application, the available computational resources, the desired field of view, and the spatial sampling necessary to preserve important features of the medium should be considered.

References

- [1] A. P. Sarvazyan, F. L. Lizzi, and P. N. Wells, “A new philosophy of medical imaging,” *Med. Hypotheses*, vol. 36, no. 4, pp. 327–35, 1991.
- [2] J. Demongeot, J. Bezy-Wendling, J. Mattes, P. Haigron, N. Glade, and J.L. Coatrieux, “Multiscale modeling and imaging: the challenges of biocomplexity,” *Proc. IEEE*, vol. 91, no. 10, pp. 1723–37, 2003.
- [3] A. Sarvazyan, “Model-based imaging,” *Ultrasound Med. Biol.*, vol. 32, no. 11, pp. 1713–20, 2006.
- [4] J. A. Jensen, “Field: a program for simulating ultrasound systems,” in *Med & Biol Eng & Comp.*, 1996, vol. 34, Suppl. 1, Part 1, pp. 351–3.
- [5] J.A. Jensen and I. Nikolov, “Fast simulation of ultrasound images,” in *Proc IEEE Ultrason Symp*, 2000, vol. 2, pp. 1721–4.
- [6] T. D. Mast, L. P. Souriau, D.-L. Liu, M. Tabei, A. I. Nachman, and R. C. Waag, “A k -space method for large-scale models of wave propagation in tissue,” *IEEE Trans. Ultrason. Ferroelectr. Freq. Control*, vol. 48, no. 2, pp. 341–54, 2001.
- [7] B. T. Cox, S. Kara, S. R. Arridge, and P. C. Beard, “ k -space propagation models for acoustically heterogeneous media: application to biomedical photoacoustics,” *J. Acoust. Soc. Am.*, vol. 121, no. 6, pp. 3453–64, 2007.
- [8] T. Douglas Mast, “Two- and three-dimensional simulations of ultrasonic propagation through human breast tissue,” *Acoust. Res. Lett. Online*, vol. 3, no. 2, pp. 53–58, 2002.
- [9] M. Tabei, T. D. Mast, and R. C. Waag, “A k -space method for coupled first-order acoustic propagation equations,” *J. Acoust. Soc. Am.*, vol. 111, no. 1, pp. 53–63, 2002.

- [10] M. Tabei, T. D. Mast, and R. C. Waag, "Simulation of ultrasonic focus aberration and correction through human tissue," *J. Acoust. Soc. Am.*, vol. 113, no. 2, pp. 1166–76, 2003.
- [11] M. I. Daoud and J. C. Lacefield, "Parallel three-dimensional simulation of ultrasound imaging," in *Proc. 22nd Intl. Symp. High Perform. Comp. Sys. Appl.*, 2008, pp. 146–152.
- [12] J. C. Tillett, M. I. Daoud, J. C. Lacefield, and R. C. Waag, "A k -space method for acoustic propagation using coupled first-order equations in three dimensions," *J. Acoust. Soc. Am.*, In Press.
- [13] E. Turkel, "On the practical use of high-order methods for hyperbolic systems," *J. Comp. Phys.*, vol. 35, no. 3, pp. 319–40, 1980.
- [14] A. Sulistio, C. S. Yeo, and R. Buyya, "A taxonomy of computer-based simulations and its mapping to parallel and distributed systems simulation tools," *Softw. Pract. Exper.*, vol. 34, no. 7, pp. 653–73, 2004.
- [15] M. I. Daoud, Y.-T. Shen, and J. C. Lacefield, "A scalable parallel implementation of a k -space method for large-scale ultrasound imaging simulations," in *Proc. IEEE Ultrason. Symp.*, 2006, pp. 2194–97.
- [16] A. D. Pierce, "The wave theory of sound," in *Acoustics : An Introduction to Its Physical Principles and Applications*, chapter 1. Acoustical Society of America, Woodbury, N.Y., 2 edition, 1989.
- [17] B. Fornberg, *A practical guide to pseudospectral methods*, Cambridge University Press, Cambridge, 1996.
- [18] X. Yuan, D. Borup, J. Wiskin, M. Berggren, and S. A. Johnson, "Simulation of acoustic wave propagation in dispersive media with relaxation losses by using

- FDTD method with PML absorbing boundary condition,” *IEEE Trans. Ultrason. Ferroelectr. Freq. Control*, vol. 46, no. 1, pp. 14–23, 1999.
- [19] A. I. Nachman, J. F. Smith, and R. C. Waag, “An equation for acoustic propagation in inhomogeneous media with relaxation losses,” *J. Acoust. Soc. Am.*, vol. 88, no. 3, pp. 1584–95, 1990.
- [20] X. Yuan, D. Borup, J. W. Wiskin, M. Berggren, R. Eidens, and S. A. Johnson, “Formulation and validation of Berenger’s PML absorbing boundary for the FDTD simulation of acoustic scattering,” *IEEE Trans. Ultrason. Ferroelectr. Freq. Control*, vol. 44, no. 4, pp. 816–22, 1997.
- [21] D. B. Skillicorn and D. Talia, “Models and languages for parallel computation,” *ACM Comput. Surv.*, vol. 30, no. 2, pp. 123–69, 1998.
- [22] M. Frigo and S. G. Johnson, “The design and implementation of FFTW3,” *Proc. IEEE*, vol. 93, no. 2, pp. 216–31, 2005.
- [23] Message Passing Interface Forum, “MPI: A message-passing interface standard version 2.1,” Tech. Rep., University of Tennessee, Knoxville, TN, 2008.
- [24] V. C. Anderson, “Sound scattering from a fluid sphere,” *J. Acoust. Soc. Am.*, vol. 22, no. 4, pp. 426–31, 1950.
- [25] T. D. Mast, L. M. Hinkelman, M. J. Orr, V. W. Sparrow, and R. C. Waag, “Simulation of ultrasonic pulse propagation through the abdominal wall,” *J. Acoust. Soc. Am.*, vol. 102, no. 2, pp. 1177–90, 1997.
- [26] K. C. Graham, L. A. Wirtzfeld, L. T. MacKenzie, C. O. Postenka, A. C. Groom, I. C. MacDonald, A. Fenster, J. C. Lacefield, and A. F. Chambers, “Three-dimensional high-frequency ultrasound imaging for longitudinal evaluation of liver metastases in preclinical models,” *Cancer Res.*, vol. 65, no. 12, pp. 5231–7, 2005.

- [27] R. L. Burden, J. D. Faires, and A. C. Reynolds, "Iterative techniques in matrix algebra," in *Numerical Analysis*, chapter 8. Prindle, Weber, and Schmidt, Boston, MA, 1978.
- [28] S. Maruvada, K. K. Shung, and S. H. Wang, "High-frequency backscatter and attenuation measurements of selected bovine tissues between 10 and 30 MHz," *Ultrasound Med. Biol.*, vol. 26, no. 6, pp. 1043–9, 2000.
- [29] L. R. Taggart, R. E. Baddour, A. Giles, G. J. Czarnota, and M. C. Kolios, "Ultrasonic characterization of whole cells and isolated nuclei," *Ultrasound Med. Biol.*, vol. 33, no. 3, pp. 389–401, 2007.
- [30] A. Grama, A. Gupta, G. Karypis, and V. Kumar, "Analytical modeling of parallel programs," in *Introduction to Parallel Computing*, chapter 5. Addison-Wesley, Harlow, England, 2nd edition, 2003.
- [31] S.-W. Huang and P.-C. Li, "Ultrasonic computed tomography reconstruction of the attenuation coefficient using a linear array," *IEEE Trans. Ultrason. Ferroelectr. Freq. Control*, vol. 52, no. 11, pp. 2011–22, 2005.
- [32] F. S. Foster, M. Y. Zhang, Y. Q. Zhou, G. Liu, J. Mehi, E. Cherin, K. A. Harasiewicz, B. G. Starkoski, L. Zan, D. A. Knapik, and S. L. Adamson, "A new ultrasound instrument for in vivo microimaging of mice," *Ultrasound Med. Biol.*, vol. 28, no. 9, pp. 1165–72, 2002.
- [33] D. A. Christensen, "Transducers, beam patterns, and resolution," in *Ultrasonic Bioinstrumentation*, chapter 5. Wiley, New York, N.Y., 1988.
- [34] N. Akashi, J. Kushibiki, N. Chubachi, and F. Dunn, "Acoustic properties of selected bovine tissues in the frequency range 20–200 MHz," *J Acoust Soc Am*, vol. 98, no. 6, pp. 3035–9, 1995.

Chapter 3

Stochastic Modeling of Normal and Tumour Tissue Microstructure for High-Frequency Ultrasound Imaging Simulations

The content of this chapter has been accepted for publication in IEEE Transactions on Biomedical Engineering with author list M. I. Daoud and J. C. Lacefield.*

3.1 Introduction

The ongoing development of high-resolution imaging technologies promises to advance the study of cancer biology and treatment in small-animal tumour models. Small-animal cancer models are imaged using many modalities [1], including high-frequency (20-60 MHz) ultrasound [2]. Preliminary progress has been made toward

*© 2009 IEEE. Reprinted, with permission, from IEEE Transactions on Biomedical Engineering, “Stochastic Modeling of Normal and Tumor Tissue Microstructure for High-Frequency Ultrasound Imaging Simulations” by M. I. Daoud and J. C. Lacefield.

using high-frequency ultrasound backscatter to quantify morphological variations of tissue microstructure that differentiate tumours derived from different cell lines [3] and accompany anti-cancer treatment responses [4]. Establishing relationships between tissue microstructure and high-frequency ultrasound backscattering would provide additional information about tumour growth and treatment response that complement conventional metrics such as tumour size and shape.

Previous studies have suggested that high-frequency ultrasound scattering in tissue can be predicted using scattering models that emphasize the morphology and spatial organization of cells and nuclei. For example, Baddour *et al.* [5] proposed analytical scattering models of single cells and showed that the high-frequency scattering response of a single cell can be computed by modeling the cell as a sphere. An idealized two-dimensional (2-D) scattering model proposed by Hunt *et al.* [6] treats tissue microstructure as a population of nuclei embedded in a homogeneous medium, with each nucleus represented as a group of point-like scatterers. Simulations performed with this model suggest that high-frequency backscattering from cell ensembles is correlated with the positions and structure of the nuclei. The assumption that the nuclei are the major scattering source at high frequency agrees with empirical results reported by Taggart *et al.* [7], which indicate that high-frequency backscattering from cell ensembles is dominated by the size of the nuclei. These concepts were combined by Doyle *et al.* [8], who proposed a three-dimensional (3-D) scattering model that represents tissue microstructure as an aggregation of spherical cells embedded in an extracellular matrix, where each cell is represented as a spherical nucleus surrounded with cytoplasm. This 3-D model was used to carry out high-frequency ultrasound scattering simulations with several hundred cells configured to produce random, clustered, and ordered cell packing with a variable ratio of cell diameter to nucleus diameter. The simulations show correlation between high-frequency ultrasound scattering and the spatial organization and internal structure of the cells.

This paper extends the foregoing concepts by developing tissue models for fu-

ture high-frequency ultrasound simulations in which simulated tissue is configured to quantitatively match histology data. A 3-D stochastic tissue model is presented that describes tissue microstructure based on stereological analyses of histology slides. The model is employed to represent healthy mouse liver and experimental liver metastasis specimens. Similar to the scattering model of Doyle *et al.* [8], tissue is treated as a population of spherical cells embedded in a homogeneous extracellular matrix. Each cell consists of a spherical nucleus surrounded by homogeneous cytoplasm. The ratio of cell diameter to nucleus diameter and the volume fraction and size distribution of nuclei estimated by stereological analysis are incorporated into the model. The 3-D spatial organization of cells is described by a Gibbs-Markov point process similar to the 2-D point process employed in [9] to model the spatial arrangement of red blood cells. The parameters of the Gibbs-Markov process are tuned to accurately reproduce the observed 3-D spatial arrangement of nuclei. Nuclear spatial arrangement is characterized using three spatial organization descriptors adopted from materials science [10] that are computed based on the 2-D spatial arrangement of nuclei sections in random histology slides through the tissue. The descriptors quantify the number density of nuclei, the deviation of the spatial arrangement of nuclei from a uniform distribution, and the separation between directly neighbouring nuclei. The model is run on a parallel computing facility to reduce the running time needed to create relatively large simulated tissue volumes. A preliminary version of this work has appeared in [11].

Other researchers have studied ultrasound scattering in tissue using analytical scattering models with tissue structural data extracted directly from histology [12, 13]. An alternative approach is to perform ultrasound simulations using simulated tissues generated with the proposed stochastic model configured to match the microstructural properties of a particular tissue specimen. One advantage of the stochastic model is that the number and dimensions of the simulated tissues are not limited by the available tissue specimen as long as a representative sample is analyzed. Moreover,

the stochastic model enables at least two potentially important types of studies. First, simulations can be performed to determine the importance of including or ignoring particular microstructural properties in ultrasound scattering calculations. Second, the stochastic tissue model can be used to investigate the effect on high-frequency ultrasound scattering of varying individual structural properties while the other model parameters are set to match a particular tissue specimen and held constant.

3.2 Materials and methods

3.2.1 Experimental characterization of tissue microstructure

Normal murine liver tissue and liver metastasis specimens were analyzed to determine their structural properties. The normal liver specimen was obtained from a healthy wildtype C57BL/6 mouse (Harlan, Indianapolis, IN). The tumour specimen was obtained from an experimental liver metastasis model prepared by injecting B16F1 murine melanoma [14] cells into the mesenteric vein of a C57BL/6 mouse as described in [15]. The metastasis model was monitored with 3-D ultrasound as described in [15] and sacrificed to obtain histology slides when tumours were ~ 1 mm diameter. Animal experiments were performed in accordance with a protocol approved by the University of Western Ontario Animal Use Subcommittee.

Mouse liver tissue was fixed in 10% neutral buffered formalin, embedded in paraffin, and sliced into $3\text{-}\mu\text{m}$ thick histology slices. Three randomly chosen histology slides from the normal liver specimen were stained with 4',6-diamidino-2-phenylindole (DAPI) to highlight the nuclei (Fig. 3.1(a)). Thirteen randomly located 0.43×0.32 mm² fields of view were obtained from the three DAPI-stained slides using an Axiovert 200M microscope (Carl Zeiss, Oberkochen, Germany) with $20\times$ magnification (the microscope field of view was much smaller than the tissue section on any one slide). The same procedure was applied to three histology slides from the experimental

metastasis specimen to obtain five fields of view from the interior of a single tumour. The fields of view of the experimental metastasis specimen are chosen to avoid any visibly necrotic regions because this tumour model undergoes liquefactive necrosis, so such regions produce negligible ultrasound backscatter and are easily interpreted by visual inspection of B-mode images [15]. The thirteen DAPI images of the normal liver specimen and the five DAPI images of the experimental metastasis specimen contained comparable numbers of nuclei (on the order of a few thousand) that, as will be discussed later, provided representative samples of each tissue specimen. The histology slides were restained with hematoxylin and eosin (H&E, Fig. 3.1(b)) to highlight the boundaries of both cells and nuclei. The H&E-stained slides were digitized using the Axiovert 200M to obtain fields of view that approximately matched the DAPI images. The DAPI and H&E were manually aligned via rigid registration with Adobe Photoshop CS2 (Adobe Systems Incorporated, San Jose, California). The digitized DAPI images were processed semi-automatically with CellProfiler [16] and then manually by a human operator to segment nuclei sections. ImageJ [17] was employed to compute the areas and the centre coordinates of the segmented nuclei sections.

The areas of nuclei in the digitized DAPI images are greater than the real areas of nuclei observed in the matching H&E images due to blurring artefacts in the DAPI images. However, segmenting the H&E images is a challenging task due to the relatively high variability of staining intensity in both the nuclei and background. In this study, the areas of nuclei are estimated using the segmented DAPI images after correcting for the blurring artefact. The correction is performed by multiplying the area of each segmented nucleus by a scaling factor computed for the DAPI image from which the nucleus was segmented. The scaling factor is defined as the sum of the areas of 50 randomly chosen nuclei in a DAPI image divided by the sum of the areas of the same nuclei in the matching H&E image.

Two types of structural properties are used to evaluate tissue microstructure: morphological properties and the spatial organization of cells and nuclei within the

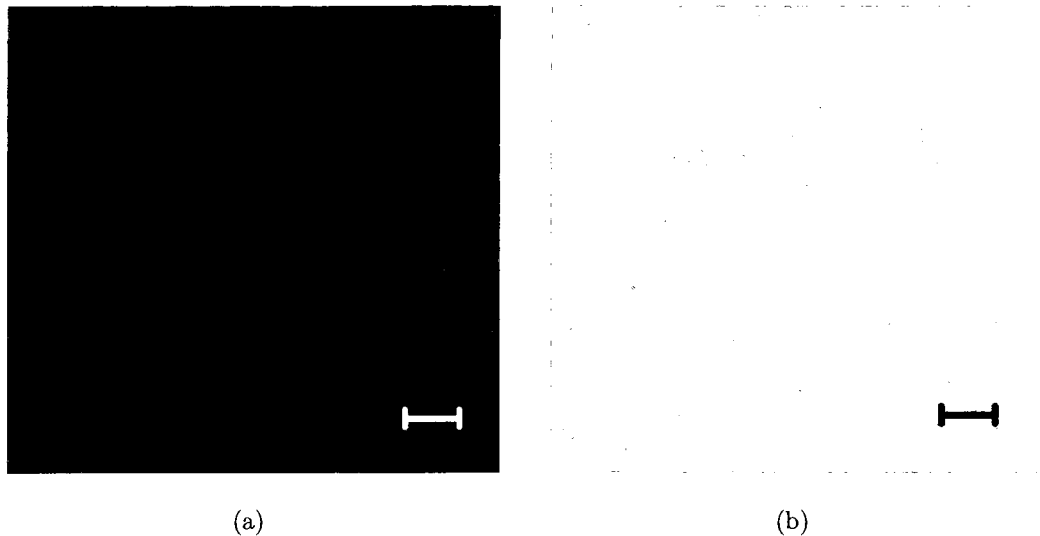


Fig. 3.1: Digitized images at $20\times$ magnification of healthy mouse liver stained with (a) DAPI and (b) H&E. Scale bar = $30\ \mu\text{m}$.

tissue volume. The morphological properties are the volume fraction (V_v) of the nuclei, the size distribution of the nuclei, and the maximum ratio of cell diameter to nucleus diameter. The nuclear volume fraction is defined as the sum of all nuclei volumes in the tissue divided by the total tissue volume. The volume fraction of the nuclei is estimated from the nuclear area fraction in random sections through the tissue using the stereological analysis technique [18] described in section 1.5. The nuclear area fraction is computed from the segmented nuclei in the DAPI images after correcting for the Holmes effect [19]. The nuclear size distribution, which is the histogram of nuclei diameters normalized by the total number of nuclei, is estimated from the sizes of the nuclei observed in the DAPI images using the Schwartz-Saltykov method [20] summarized in section 1.5 with nine groups of nuclei sizes. The maximum ratio of cell diameter to nucleus diameter is estimated from the H&E-stained slides by analyzing 50 cells that are relatively large with respect to the size of their nuclei. The nuclear size distribution parameter enables the simulated tissue to include a range

of nuclei sizes, the combination of the nuclear size distribution and nuclear volume fraction determines the number of nuclei in a tissue volume, and the maximum ratio of nuclear to cell size enables the size of each cell to be chosen from an assumed distribution independently from the size of its nucleus.

The spatial organization of cells and nuclei, meaning the positions of the cells and nuclei within the larger tissue volume, is quantified using three descriptors of the 2-D spatial arrangement of nuclei computed in random planes through the tissue: the K-function, the radial distribution function, and the nearest neighbour distribution function [21]. Only nuclei were analyzed in this paper because we assumed cells and nuclei have the same centre positions, although the model could easily be modified to relax this assumption. The K-function, $k(r)$, is the expected number of nuclei centres within a distance r from the centre of an individual nucleus. The radial distribution function, $g(r)$, is defined such that the expected number of nuclei centres within a ring from r to $r + dr$ away from the centre of an arbitrary nucleus is equal to the product of the average number of nuclei per unit area of tissue, the area of the ring, and $g(r)$. The nearest neighbour distribution function, $p(r)$, is defined such that the probability density function $p(r)dr$ is equal to the probability that one or more nuclei centres exist within a ring from r to $r+dr$ away from the centre of an arbitrary nucleus and no nuclei centres are closer than r from that nucleus. The K-function characterizes the average number density of nuclei over a range of volumes surrounding an individual nucleus. The radial distribution function tests for the presence of cell clustering because a value of $g(r)$ greater than one indicates that the ring from r to $r + dr$ contains more nuclei than would be expected if the nuclei were spread uniformly within the tissue. The two functions are related by $g(r) = \frac{1}{2\pi r N_A} \frac{dk(r)}{dr}$, where N_A is the average number of nuclei per unit area, so $k(r)$ also includes the effects of clustering. However, both functions are used in the analysis because $g(r)$ shows clearly any deviations from a uniform spatial distribution, while such deviations are difficult to interpret directly from $k(r)$. Finally, $p(r)$ shows the average spacing between adjacent cells.

In this study, the centre coordinates of the segmented nuclei are used to evaluate the local K-function, radial distribution function, and nearest neighbour distribution function for each individual field of view in the DAPI images. The value of r is varied from 0 to $65.93 \mu\text{m}$ to evaluate the K-function and from 0 to $62.46 \mu\text{m}$ to evaluate the radial distribution and nearest neighbour distribution functions. In both cases, an increment, dr , of $3.47 \mu\text{m}$ is employed. Following [10], the maximum value of r used to compute the spatial descriptors is on the order of ten times the $6.4 \mu\text{m}$ diameter that is the average diameter of both healthy liver and liver metastasis nuclei. The increment, dr , was approximately half the average nucleus diameter. The spatial descriptors are computed using nuclei whose centres are farther than $65.93 \mu\text{m}$ from the edges of the field of view. The mean and standard deviation of $k(r)$, $g(r)$, and $p(r)dr$ for each type of tissue are computed from the local spatial descriptors obtained from the individual fields of view. Approximately 3000 nuclei in each type of tissue were analyzed to compute the spatial descriptors, nuclear volume fraction, and nuclear size distribution. This number of nuclei is comparable to the number of spherical particles used to analyze the microstructure of polymer materials in [10].

3.2.2 Modeling the spatial arrangement of cells

The 3-D coordinates of cell centres are modeled as a realization of a Gibbs-Markov point process [22] similar to the 2-D point process employed in [9] to represent the spatial arrangement of red blood cells. For a tissue with a fixed number of cells, M , the arrangement of cell centres can be expressed as a vector $\vec{X} = \{\vec{x}_1, \dots, \vec{x}_M\}$, where \vec{x}_i is the centre coordinate of the i th cell. The Gibbs-Markov point process employed in our model assigns an energy to a configuration of cell positions, \vec{X} , based on inter-cell interactions:

$$U(\vec{X}) = \sum_{j=2}^M \sum_{i=1}^{j-1} \theta(i, j) \quad (3.1)$$

where $U(\vec{X})$ is the energy of \vec{X} and $\theta(i, j)$ is the pair potential that describes positive and negative energies resulting from hypothetical repulsive and attractive forces, respectively, between the i th and j th cells. Configurations of cell centres that have low energy are preferred to configurations with greater energy. Therefore, the spatial arrangement of cells is controlled by the form and parameter values of the pair potential function $\theta(i, j)$.

The model is designed to produce non-overlapping cells and to produce cell clustering if clustering is appropriate. Overlapping cells are avoided by using a pair potential function that assigns high positive (repulsive) energy to overlapping cells. For tumour tissue, cell clustering is modeled by defining a spherical attractive zone around each cell and employing a pair potential function that returns negative (attractive) energy for cells with overlapping attractive zones. An empirical pair potential formula that satisfies these two requirements is:

$$\theta(i, j) = V_{rep}I\left(\frac{\|\vec{x}_i - \vec{x}_j\|}{b_i + b_j}\right)e^{-2\left(\frac{\|\vec{x}_i - \vec{x}_j\|}{b_i + b_j}\right)} - V_{att}I\left(\frac{\|\vec{x}_i - \vec{x}_j\|}{c_i + c_j}\right)\varphi(i, j) \quad (3.2)$$

where V_{rep} is the maximum repulsive energy between two overlapping cells, $\|\vec{x}_i - \vec{x}_j\|$ is the distance between the centres of the i th and j th cells, b_i and b_j are the radii of the i th and j th cells, V_{att} is the maximum attractive energy between two cells with overlapping attractive zones, c_i and c_j are the radii of the attractive zones of the i th and j th cells, $I(y)$ is the indicator function that returns 1 if the positive real number y is less than 1 and 0 otherwise, and $\varphi(i, j)$ is the intersection volume between the attractive zones of the i th and j th cells normalized by the volume of the smallest cell included in the simulated tissue. The magnitude of V_{rep} must be much greater than V_{att} to ensure that the repulsive energy of significantly overlapping cells dominates their attractive energy.

3.2.3 Synthesis of simulated tissue

A 3-D simulated tissue is initialized by creating a population of uniformly distributed cells within a periodic cuboid. The number of cells and the distribution of nuclei sizes are chosen to match the measured nuclear volume fraction and size distribution. The ratio of cell diameter to nucleus diameter for each cell is independently selected from a uniform distribution between 1 and the maximum ratio of cell to nucleus diameter. The magnitude of V_{rep} is set to $\sim 2 \times 10^5$ times greater than V_{att} . The exact value of V_{rep}/V_{att} is not important provided $V_{rep} \gg V_{att}$.

The Metropolis sampler [23] is used to create a realization, \vec{X} , of the Gibbs-Markov point process based on the procedure presented in Section II-C of [9]. In this procedure, the initial configuration of cell centres is iteratively altered to create a sequence of provisional cell arrangements that asymptotically reaches a realization of the Gibbs-Markov point process. Each step of the iterative procedure involves randomly selecting one cell and stochastically moving it a small distance from its initial position within the 3-D volume. If the energy, $U(\vec{X})$, decreases by more than a random threshold when the selected cell is moved, the selected cell is assigned the new position; otherwise the cell is returned to its previous position. The random threshold is altered at each step. Given M cells, the Metropolis sampler is run for $320M$ steps, which is assumed sufficient to enable each run of the model to reach a different random realization of the Gibbs-Markov point process.

The computational complexity of the tissue model can be reduced by employing the fact that, at each step of the Metropolis sampler, the difference in energy before and after moving the selected cell depends only on the change in energy for that single cell, so the computation of $U(\vec{X})$ after moving a cell is restricted to updating the pair potentials associated with that cell. This reduction of computational complexity is crucial in view of the fact that the total number of cell pairs in simulated tissue volumes needed for realistic 3-D imaging simulations can be extremely large. To further reduce the running time of the tissue model, the Metropolis sampler is run

on a shared-memory parallel computing facility using the OpenMP [24] programming model.

Graphical representations of 3-D simulated tissues are created using the OpenGL (<http://www.opengl.org>) standard. The functions provided by OpenGL can produce both full 3-D visualization of the simulated tissue and 2-D slices through the tissue.

3.2.4 Tuning the model

The tissue model was separately configured to represent the microstructures of the healthy liver and experimental metastasis specimens. The volume of the simulated tissue was set to $450 \mu\text{m} \times 450 \mu\text{m} \times 192 \mu\text{m}$. To simulate healthy liver tissue, the maximum ratio of cell to nucleus diameter, denoted as β_{max} , was set equal to the value estimated from the healthy liver slides. The model was then tuned by varying the ratio of the attractive zone diameter to nucleus diameter, denoted as α , and computing the K-function, radial distribution function, and nearest neighbour distribution function in a random $450 \mu\text{m} \times 450 \mu\text{m} \times 3 \mu\text{m}$ slab through the simulated tissue. The use of a single representative slab through the simulated tissue, instead of multiple slabs, for tuning reduces the human intervention required. The thickness of the slabs used to tune the model matched the thickness of the histology slides. During the tuning process, four values of α were tested: 0, 2.5, 3, and 3.5, where 2.5 was chosen because it was the measured value of β_{max} . Initial empirical testing revealed that the average spatial distribution of nuclei changed very little when α was varied between 0 and β_{max} . Large values of α produce visibly greater cell clustering than was observed in the healthy liver specimens, so the tuning process was limited to α values that were only modestly greater than β_{max} . The value of α that produced the greatest number of matching points between the radial distribution function of the simulated tissue and the mean \pm standard deviation of $g(r)$ of the healthy liver specimen was chosen. The radial distribution function was found to be most sensitive to the tuning parameters, so this approach also yielded good agreement between the experimental

and simulated K-function and nearest neighbour distribution function.

The values of both α and β_{max} were tuned to represent the experimental metastasis. Tuning both α and β_{max} was required to model the metastasis to compensate for the fact that the non-uniform shape of tumour cells degrades the accuracy of representing cells as spheres. Eleven values of β_{max} were tested, ranging from 0.5 less than its measured value of 1.5 to 0.5 greater than its measured value in increments of 0.05. Six values of α were tested for each value of β_{max} : 0, $\hat{\beta}_{max}$, 1.5, 2.0, 2.5, and 3.0, where $\hat{\beta}_{max}$ is the maximum ratio of cell to nucleus diameter employed in the current tuning trial. More values of both α and β_{max} were tested for the metastasis than for the healthy liver because the metastasis model proved more challenging to tune. The combination of α and β_{max} that produced the closest agreement between the radial distribution functions of the simulated tumour and the experimental metastasis was chosen, where agreement was assessed in the same manner as for the healthy liver.

To test the accuracy of using a single tissue slab to tune the model, the mean K-function, radial distribution function, and nearest neighbour distribution function computed on ten slabs through the simulated healthy and tumour tissues were compared with those of the healthy liver specimen and experimental metastasis, respectively. The comparison was performed by counting the number of matching points between the mean spatial descriptors of each simulated tissue and the mean \pm standard deviation of the spatial descriptors of the corresponding experimental specimen. The volume of each slab was the same as the slabs used to tune the model, and the spacing between two successive slabs was fixed at 45 μm .

The variability of the spatial organization of the simulated healthy tissue was compared to that of the healthy liver specimen by computing the standard deviations at each sample of r in the K-functions, radial distribution functions, and nearest neighbour distribution functions of ten slabs through the simulated healthy tissue and of all thirteen experimental healthy liver micrographs. The same procedure is employed to compare the variability of ten slabs through the simulated tumour tissue

to the five experimental liver metastasis micrographs. The model variability was evaluated using the same simulated tissue slabs that were employed to evaluate the tuning accuracy.

3.2.5 Model scalability for imaging simulations

A simulated tissue volume of $1.0 \text{ mm} \times 1.0 \text{ mm} \times 1.0 \text{ mm}$ with the structural properties of healthy liver was constructed to demonstrate the feasibility of synthesizing tissue volumes that are sufficiently large for use in 3-D imaging simulations. For example, such a tissue volume could be employed to perform high-frequency ultrasound imaging simulations with lesions of sizes that match the sizes of the smallest tumours detected using a high-frequency ultrasound scanner [15]. The large tissue model was separately synthesized using 20 and 40 processors of a SGI Altix shared-memory cluster at the Shared Hierarchical Academic Research Computing Network (SHARCNET, <http://www.sharcnet.ca>). The cluster has 128 Itanium2 1.6 GHz processors, 256 GB of global shared memory, and runs the SUSE Linux Enterprise Server 10.1 system and the SGI ProPack 5 high performance computing environment. The total time required to initialize the model and run the Metropolis sampler was recorded for each number of processors used.

3.3 Results

3.3.1 Healthy mouse liver

The measured nuclear volume fraction and maximum ratio of cell diameter to nucleus diameter of the healthy liver tissue are equal to 0.073 and 2.5, respectively. The measured distribution of nuclei sizes is shown as a normalized histogram in Fig. 3.2(a); the mean \pm standard deviation of nucleus diameter is $6.72 \pm 2.28 \mu\text{m}$.

The tuning procedure using single tissue slabs produces the highest number of

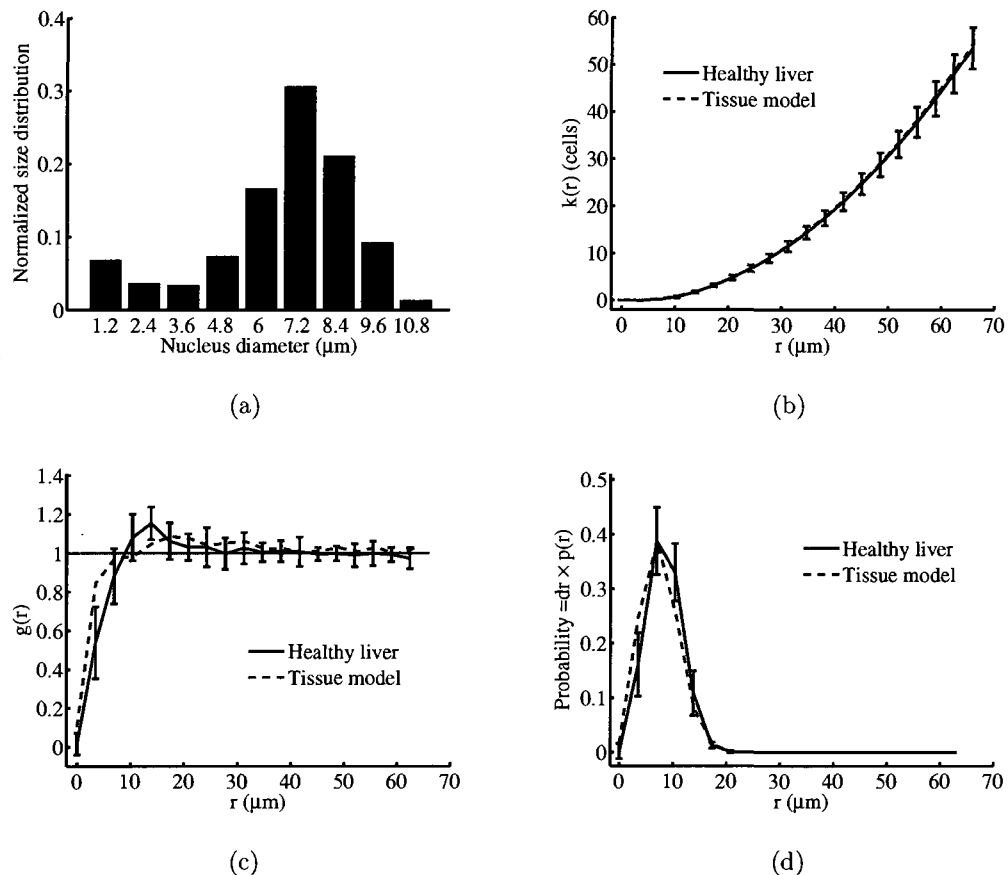


Fig. 3.2: Comparison of experimental and simulated microstructures of healthy mouse liver. (a) Histogram of the measured nuclear size distribution of healthy mouse liver; (b)-(d) 2-D descriptors of the spatial arrangement of nuclei centres in healthy murine liver slides and simulated healthy tissue slabs: (b) K-function, $k(r)$, (c) radial distribution function, $g(r)$, and (d) the probability density function $p(r)dr$ associated with the nearest neighbour distribution function, $p(r)$, are plotted as functions of distance, r , from an arbitrary nucleus centre. Error bars indicate mean \pm standard deviation of curves measured in thirteen digitized micrographs of the healthy liver specimen.

matching points between the 2-D spatial descriptors through the simulated liver tissue and the healthy liver when α is set to 0. The mean K-function, radial distribution function, and nearest neighbour distribution function computed on ten slabs through the tuned model are compared with those of the healthy liver specimen in Fig. 3.2(b),

Fig. 3.2(c), and Fig. 3.2(d), respectively. The K-functions of the simulated liver tissue and the healthy liver specimen are nearly identical. The mean K-function of the simulated liver and the liver tissue are separated by less than one standard deviation of the experimental data for all but one of the 20 values of r tested. The radial distribution function of the simulated tissue lies within one standard deviation of the mean radial distribution function of the liver specimen at 16 out of the 19 values of r analyzed. The difference between the nearest neighbour distribution function of the simulated tissue and the healthy liver tissue is less than one standard deviation at 17 out of the 19 values of r analyzed. These results demonstrate that the 3-D spatial arrangement of cells in the simulated liver tissue is very similar to that in the healthy liver specimen. The similarity of the simulated tissue to the liver specimens is illustrated by the schematic diagram of nuclei sections in a $250 \mu\text{m} \times 250 \mu\text{m} \times 3 \mu\text{m}$ slab through the simulated liver tissue and a comparable DAPI image of a healthy liver specimen in Fig. 3.3.

The standard deviations of the K-function, radial distribution function, and nearest neighbour distribution function evaluated for ten simulated tissue slabs are compared with those for the thirteen healthy liver micrographs in Fig. 3.4(a), Fig. 3.4(b), and Fig. 3.4(c), respectively. The variability of the simulated tissue's spatial descriptors is generally less than the variability of the spatial descriptors of the healthy liver specimen.

The total running time required to initialize and synthesize a sample simulated healthy tissue of volume $1.0 \text{ mm} \times 1.0 \text{ mm} \times 1.0 \text{ mm}$ is 34.7 days using 20 processors and 19.6 days using 40 processors. This sample tissue contains 3.6×10^5 cells, and hence the Metropolis sampler is run for 1.2×10^8 steps to create a random realization of the Gibbs-Markov point process.

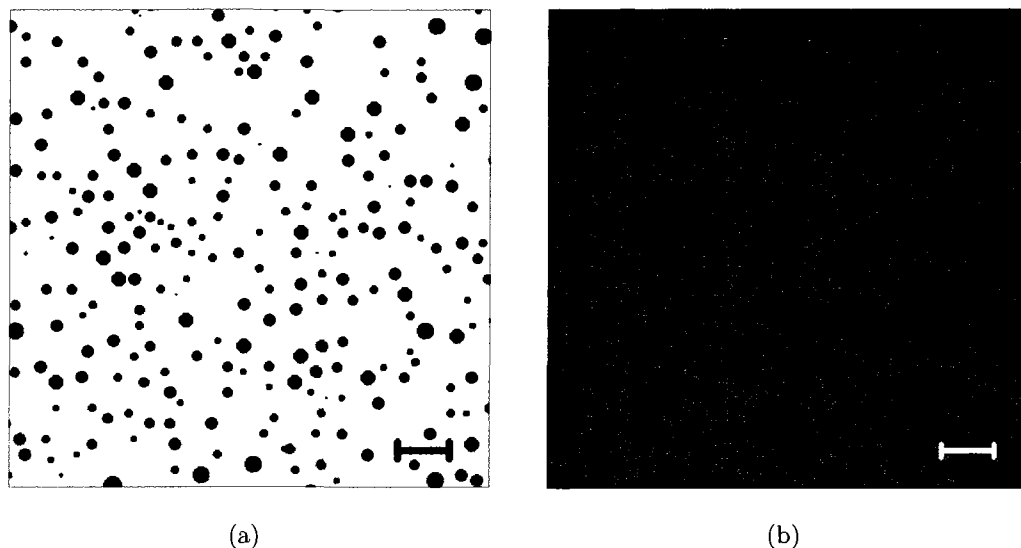


Fig. 3.3: (a) A $250 \mu\text{m} \times 250 \mu\text{m} \times 3 \mu\text{m}$ slab through the simulated liver tissue showing nuclei sections and (b) a comparable digitized DAPI-stained histology slide of a healthy mouse liver. The dark blue circles in (a) represent the size and positions of cell nuclei in the simulated tissue. Scale bar = $30 \mu\text{m}$.

3.3.2 Experimental liver metastasis

The measured values of nuclear volume fraction and maximum ratio of cell to nucleus diameter in the experimental liver metastasis are 0.179 and 1.5, respectively. The nuclear size distribution of the tumour specimen is shown in Fig. 3.5(a); the mean \pm standard deviation of nucleus diameter is $6.09 \pm 2.15 \mu\text{m}$.

The number of matching points between the spatial descriptors computed on a single slab through the simulated tumour tissue and the experimental liver metastasis is maximized when the model α and β_{max} are set to 2.0 and 1.4, respectively. The mean K-function, radial distribution function, and nearest neighbour distribution function computed on ten slabs through the tuned model are compared with those of the experimental liver metastasis specimen in Fig. 3.5(b), Fig. 3.5(c), and Fig. 3.5(d), respectively. The K-function of the simulated tumour lies within one standard deviation of the mean K-function of the experimental metastasis for all but

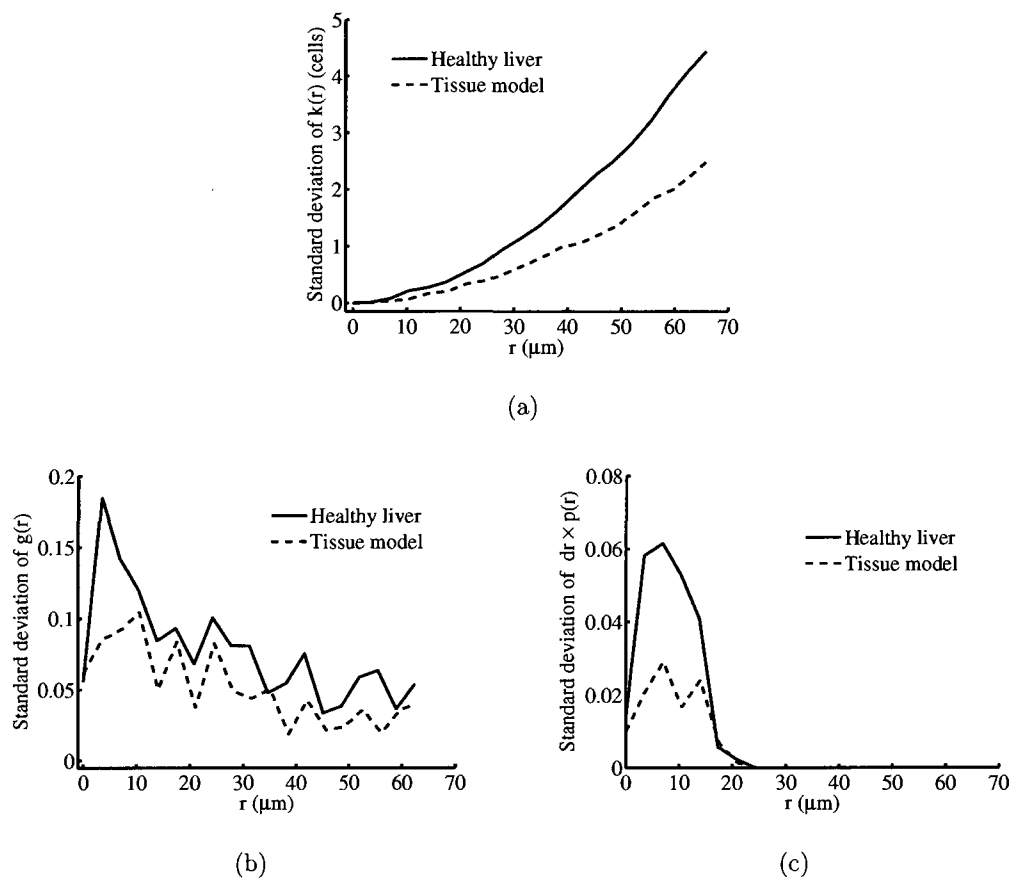


Fig. 3.4: Variability of experimental and simulated microstructures of healthy mouse liver. Standard deviation of the (a) K-function, $k(r)$, (b) radial distribution function, $g(r)$, and (c) nearest neighbour distribution function, $p(r)$, computed on thirteen digitized micrographs of the healthy liver specimen and ten simulated healthy tissue slabs are plotted as functions of distance, r , from an arbitrary nucleus centre.

one of the 20 values of r tested. The difference between the radial distribution function of the simulated tumour and the experimental liver metastasis is less than one standard deviation at 15 out of the 19 values of r analyzed. The nearest neighbour distribution function of the simulated tumour lies within one standard deviation of the mean nearest neighbour distribution function of the experimental metastasis at 18 out of the 19 values of r tested. The general similarity of the simulated tumour to

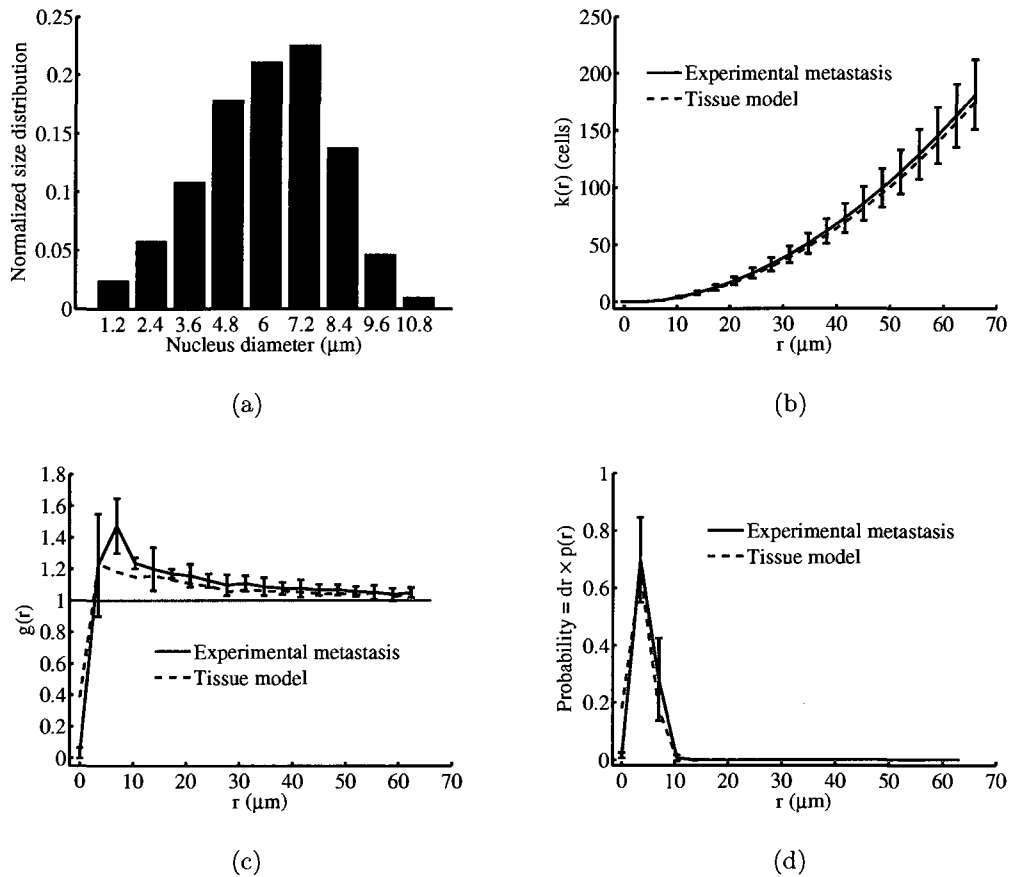


Fig. 3.5: Comparison of experimental and simulated microstructures of a murine B16F1 liver metastasis. (a) Histogram of the measured nuclear size distribution of the experimental liver metastasis; (b)-(d) 2-D descriptors of the spatial arrangement of nuclei centres in liver metastasis micrographs and simulated tumour slabs: (b) K-function, $k(r)$, (c) radial distribution function, $g(r)$, and (d) the probability density function $p(r)dr$ associated with the nearest neighbour distribution function, $p(r)$, are plotted as functions of distance, r , from an arbitrary nucleus centre. Error bars indicate mean \pm standard deviation of curves measured in five digitized micrographs of the liver metastasis specimen.

the experimental metastasis is illustrated by the schematic diagram of nuclei sections in a $250 \mu\text{m} \times 250 \mu\text{m} \times 3 \mu\text{m}$ slab through the simulated tumour and a comparable DAPI image of a liver metastasis specimen in Fig. 3.6(a) and Fig. 3.6(b), respectively.

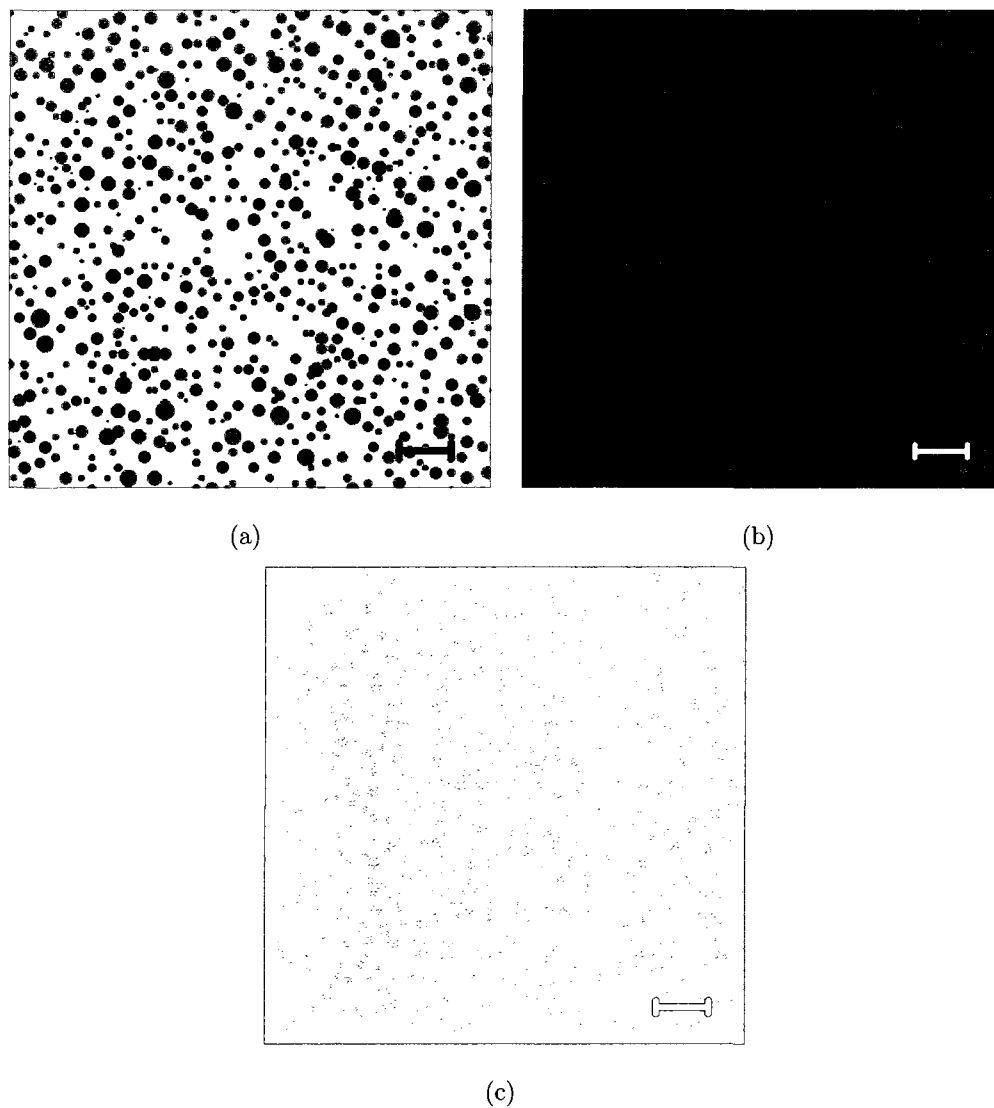
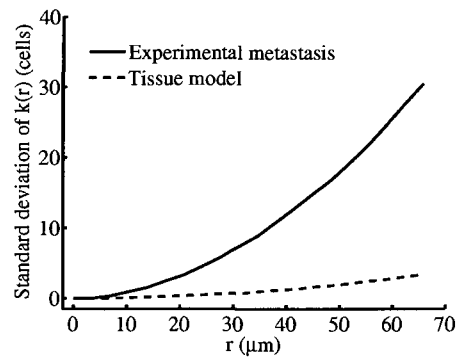


Fig. 3.6: (a) A $250 \mu\text{m} \times 250 \mu\text{m} \times 3 \mu\text{m}$ slab through the simulated tumour tissue showing nuclei sections such that each nucleus is represented as a dark blue circle, (b) a comparable digitized DAPI-stained histology slide from the interior of an experimental B16F1 metastasis in mouse liver, and (c) a schematic representation of the DAPI image in (b) such that each nucleus is modeled as a circle with the same centre coordinates as the nuclei in the DAPI image and an area equal to the product of the nucleus area in the DAPI image and a scaling factor to correct for DAPI blurring. Scale bar = $30 \mu\text{m}$.

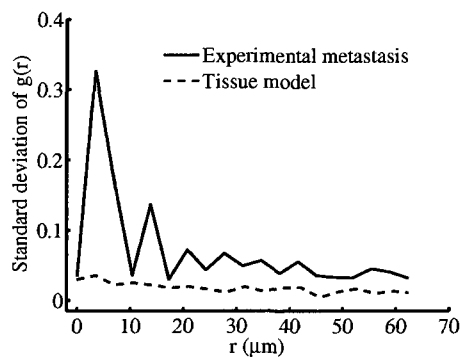
To facilitate visual comparison between the simulated tumour slab and the DAPI image, a schematic representation of the DAPI image is shown in Fig. 3.6(c). This representation is created by modeling each nucleus as a circle with the same centre coordinates as the segmented nuclei in the DAPI image. The circular representations of the nuclei each have an area equal to the product of the segmented nucleus area in the DAPI image and the scaling factor described in section 3.2.1 that compensates for blurring in the DAPI image. The simulated and experimental tumours are similar in that they both contain a higher number density of cell nuclei than the simulated and experimental healthy tissues and the simulated and experimental tumours both exhibit visible local clustering of nuclei. The most striking difference between the simulated and experimental tumours is that the global spatial distribution of nuclei is more heterogeneous in the experimental specimen. For example, the nuclei are densely packed in the centre of the DAPI image, have intermediate number density in the top left of the image, and lower number density in the bottom right of the image. The number density of nuclei in the simulated tumour is more consistent even with the inclusion of local clustering.

The mean radial distribution function of the liver metastasis specimen exhibits a peak of $g(r) = 1.47$ at $r = 6.94 \mu\text{m}$, which is higher than the peak of $g(r) = 1.15$ at $r = 13.88 \mu\text{m}$ in the healthy liver specimen. The radial distribution function of the liver metastasis specimen is greater than one for r values greater than or equal to $3.47 \mu\text{m}$, while the radial distribution function of the healthy liver oscillates above and below one for r values greater than or equal to $27.76 \mu\text{m}$.

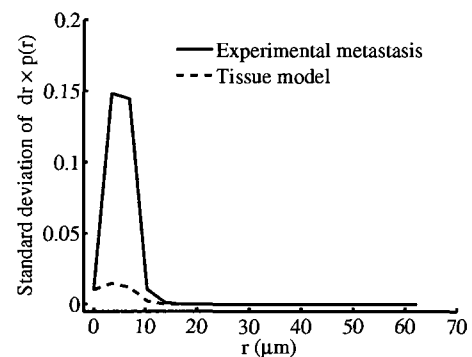
The standard deviations of the K-function, radial distribution function, and nearest neighbour distribution function evaluated on ten simulated tumour slabs are compared with those of the five experimental metastasis micrographs in Fig. 3.7(a), Fig. 3.7(b), and Fig. 3.7(c), respectively. The standard deviation of each spatial descriptor of the experimental liver metastasis is greater than that of the simulated tumour for all values of r analyzed. The variability of the spatial descriptors is also



(a)



(b)



(c)

Fig. 3.7: Variability of experimental and simulated microstructures of a murine B16F1 liver metastasis. Standard deviation of the (a) K-function, $k(r)$, (b) radial distribution function, $g(r)$, and (c) nearest neighbour distribution function, $p(r)$, computed on five digitized micrographs of the liver metastasis specimen and ten simulated tumour tissue slabs are plotted as functions of distance, r , from an arbitrary nucleus centre.

generally higher for the experimental metastasis than for the healthy liver specimen.

3.4 Discussion

In the process of developing the tissue model, it was important to consider the accuracy of the stereological techniques used to compute the nuclear volume fraction

and size distribution and tune the spatial arrangement of cells. The nuclear volume fraction can be estimated from the nuclear area fraction in 2-D sections through the tissue. However, the actual nuclear area fraction is smaller than the projected nuclear area fraction of the DAPI-stained slides because the slides have a finite thickness. The difference between the actual 2-D area fraction and the projected area fraction is called the Holmes effect [19]. The actual nuclear area fraction can be reliably estimated from the projected nuclear area fraction when the thickness of the DAPI slides is equal to or less than the average nucleus diameter [18]. Therefore, the 3- μm thickness of the DAPI slides was chosen to be smaller than the average nucleus diameter of both the healthy liver specimen and the experimental metastasis specimen, which are equal to 6.72 and 6.09 μm , respectively.

The stereological techniques used to estimate the nuclear size distribution and correct for the Holmes effect assume the nuclei are spherical. These techniques achieve high accuracy when they are applied to the healthy liver specimen because the healthy nuclei are approximately spherical. On the other hand, the non-uniform shape of the tumour nuclei degrades the accuracy of the nuclear volume fraction and size distribution estimated for the experimental liver metastasis.

The Schwartz-Saltykov method [20] that was used to estimate the nuclear size distribution samples the continuous distribution of nuclei diameters using discrete diameter bins. The method assumes all nuclei in each bin have the same diameter. The accuracy with which the nuclear size histogram estimated with the Schwartz-Saltykov method matches the continuous nuclear size distribution improves when a large number of bins are used. In this paper, the Schwartz-Saltykov method is implemented with nine bins. This discretization agrees with the general guidelines for the Schwartz-Saltykov method that suggest using 7 to 15 bins to estimate the size distribution of spherical particles [20].

The accuracy of the model depends on the feasibility of tuning the spatial organization of nuclei to obtain a 3-D distribution that matches the distribution in the

corresponding tissue specimen. Direct estimation of the 3-D positions of cell nuclei is a challenging task because it is difficult to obtain a complete set of histology slices at the $3\text{-}\mu\text{m}$ thickness needed for stereology and because it is difficult to register the slices to perform a 3-D reconstruction. Therefore, it is more practical to use stereological techniques to characterize the 3-D spatial organization of nuclei in tissue based on measurements of the 2-D distribution of nuclei in sample histology slides. For consistency, the same technique was used to characterize the spatial arrangement of nuclei in the 3-D simulated tissues based on sample 2-D slabs from the simulated tissues. The spatial arrangement of nuclei in the 3-D simulated tissues is tuned to obtain good agreement between the nuclear spatial distribution in sample 2-D slabs through the simulated tissue and the 2-D histology slides as shown in Fig. 3.2 and Fig. 3.5. Such agreement implies reasonable matching between the 3-D nuclear spatial arrangement in the simulated tissues and the tissue specimens. This tuning procedure is similar to the procedure employed in [10] using sample 2-D planes to compare the 3-D spatial arrangement of spherical particles in a simulated polymer microstructure with an experimentally determined polymer microstructure.

The model parameters obtained from the tuning process provide some insight about the microstructure of the experimental specimens and about the ability of the model to reproduce that microstructure. The healthy tissue results reported in Section 3.3.1 show good agreement between the nuclear spatial distribution in the simulated healthy tissue and that in the healthy liver specimen when the model's α is set to zero and β_{max} is set to the maximum ratio of cell to nucleus diameter estimated for the healthy liver specimen. The use of an α value of zero implies that there is no clustering between adjacent cells in the healthy liver specimen. The matching between the model's β_{max} and the corresponding value estimated for the healthy liver indicates that the cells in the healthy liver specimen can accurately be represented as spheres of similar volumes.

The tumour tissue results presented in Section 3.3.2 show reasonable matching

between the average nuclear spatial arrangement in the simulated tumour tissue and the experimental metastasis specimen when the model's α is set to 2.0 and β_{max} is set to 1.4. The model uses a β_{max} smaller than the value of 1.5 estimated for the experimental metastasis specimen to compensate for the non-uniform shape of tumour cells. At equal values of β_{max} , the non-uniformly shaped cells produce denser cell packing than the packing achieved in the model when cells are represented as spheres. The use of an α value greater than β_{max} ensures that, for all cells, the attractive zone in the pair potential extends beyond the repulsive zone, which is necessary to enable the model to produce cell clustering. The amount of cell clustering increases as the difference between α and β_{max} increases. The tuning result ($\alpha = 2.0, \beta_{max} = 1.4$) indicates that substantially greater cell clustering is observed in the experimental metastasis than in the healthy liver, where $\alpha = 0$.

The higher cell clustering and packing in the experimental metastasis specimen compared to the healthy liver specimen is further demonstrated by the measured morphological and spatial organization descriptors presented in Section 3.3.1 and Section 3.3.2. The nuclear volume fraction of the metastasis specimen is approximately 2.5 times greater than the healthy liver specimen. The mean K-function and radial distribution function of the experimental metastasis specimen is higher than the healthy liver specimen for all tested values of r , which indicates that, at a given distance from a particular cell, both the number of neighbouring cells and the incremental increase in the number of neighbouring cells with increasing r are higher in the tumour tissue compared to the healthy tissue. The peak of the nearest neighbour distribution function is narrower and shifted toward $r = 0$ for the experimental metastasis specimen compared to the healthy liver specimen, which implies smaller average spacing between adjacent cells in the metastasis compared to the healthy liver.

Significant deviations between the radial distribution function of the experimental metastasis specimen and that of the simulated tumour tissue (Fig. 3.5(c)) are observed

at r values of 0 and $6.94 \mu\text{m}$, in which the difference between the two functions is equal to -0.35 and 0.29 , respectively, where the negative value indicates that the model $g(r)$ is higher than the experimental $g(r)$ at $r = 0$. The heterogeneity in nuclear spacing observed visually in the experimental metastasis slides at $20\times$ magnification, in which the smallest nuclei (diameter $\sim 1.2 \mu\text{m}$) tend to occur mostly in sparsely populated areas, might be the source of the deviation at $r = 0$. The model allows two nuclei smaller than dr to be separated by less than dr , but this arrangement is observed less frequently in the experimental micrographs. The high value of the radial distribution function at $r = 6.94 \mu\text{m}$ is caused by the closely packed, non-uniform cells observed in the experimental metastasis specimen; such a high cell packing is not obtained in the spherical-cell model even when a β_{max} value of 1.4, which allows unrealistically small spacing of neighbouring nuclei, is used.

The tissue model employed in this paper does not include other anatomical structures such as blood vessels. Therefore, the spatial arrangement of nuclei in the simulated tissues is generally less variable than the corresponding experimental tissue specimens. This lower variability in the simulated tissues is demonstrated by the lower standard deviations of the spatial descriptors of the simulated healthy tissue compared to the liver specimen (Fig. 3.4) and of the simulated tumour tissue compared to the experimental metastasis specimen (Fig. 3.7).

Abnormal growth of cells in a tumour presumably increases the structural heterogeneity of the experimental metastasis compared to the experimental healthy liver. The high heterogeneity of the metastasis specimen is not fully described by the model parameters, which explains the consistently higher standard deviations of all three spatial descriptors of the experimental metastasis compared to the simulated tumour tissue. This result is consistent with the visible differences in the global spatial distribution of nuclei in the simulated and experimental tumours shown in Fig. 3.6. The standard deviation of the spatial descriptors of the simulated healthy tissue and the healthy liver specimen are closer because the healthy liver is more homogeneous.

Fixing the healthy and cancerous liver specimens shrinks the tissue due to the dehydration process. Since the nucleus is mainly composed of DNA and protein, the shrinkage artefact is not expected to significantly affect the estimated values of nuclear size distribution, but the measured spacings between the nuclei and diameters of the cells are expected to be smaller than they are in the liver specimens before formalin fixing.

Implementing the tissue model on a shared-memory computer cluster reduces the cost of inter-processor communications compared to a distributed-memory cluster. Therefore, the running time of the model is expected to be inversely proportional to the number of processors used. This expectation was confirmed by the comparison of the running time required to initialize and synthesize a $1 \text{ mm} \times 1 \text{ mm} \times 1 \text{ mm}$ simulated healthy tissue, which was 19.6 days using 40 processors compared to 34.7 days using 20 processors. The extensive number of iterations of the Metropolis sampler used to simulate the spatial arrangement of cells and nuclei is responsible for the high computational complexity of the tissue model. The importance of including the spatial organization of cells and nuclei in high-frequency ultrasound scattering studies has been demonstrated at 50 MHz by Hunt *et al.* [25]. For simulations where it is sufficient to describe cell and nuclei spatial arrangement using approximate formulas, the tissue model can be readily modified to produce simulated tissues with much shorter running times by positioning the cells using an assumed probability density function rather than running the Metropolis sampler.

3.5 Conclusion

A 3-D stochastic tissue model is proposed that incorporates microscopic structural properties representing morphological and spatial variations, such as cell number density, cell and nucleus size, and cell clustering and packing, that are hypothesized to be significant determinants of high-frequency ultrasound backscattering. The nu-

clear volume fraction and distribution of nuclei sizes are quantified using stereological techniques and the spatial organization of nuclei is quantified using three spatial descriptors adopted from materials science. These descriptors effectively characterize differences in nuclear spatial arrangement between healthy liver and experimental liver metastasis. The spatial descriptor functions demonstrate quantitatively that the experimental metastasis is more heterogeneous than healthy liver and is characterized by substantial cell clustering. The proposed model accurately reproduces the microstructure of the relatively homogeneous healthy liver. The model also accurately reproduces the average cell clustering observed in the metastasis, but it is less able to reproduce the heterogeneity of the metastasis because it assumes spherical cells and does not include any other anatomical structures. The model is nevertheless expected to be useful in combination with ultrasound simulators that compute 3-D acoustic propagation and scattering to investigate relationships between tissue microanatomy and high-frequency backscattering, since published studies indicate that cell nuclei are a prominent source of scattering in the 20-60 MHz band.

References

- [1] R. Weissleder, "Scaling down imaging: molecular mapping of cancer in mice," *Nat. Rev. Cancer*, vol. 2, pp. 1–8, 2002.
- [2] D. H. Turnbull, J. A. Ramsay, G. S. Shivji, T. S. Bloomfield, L. From, D. N. Sauder, and F. S. Foster, "Ultrasound backscatter microscope analysis of mouse melanoma progression," *Ultrasound Med. Biol.*, vol. 22, pp. 845–53, 1996.
- [3] M. L. Oelze, W. D. O'Brien Jr, J. P. Blue, and J. F. Zachary, "Differentiation and characterization of rat mammary fibroadenomas and 4T1 mouse carcinomas using quantitative ultrasound imaging," *IEEE Trans. Med. Imaging*, vol. 23, pp. 764–71, 2004.
- [4] B. Banihashemi, R. Vlad, B. Debeljevic, A. Giles, M. C. Kolios, and G. J. Czarnota, "Ultrasound imaging of apoptosis in tumor response: novel preclinical monitoring of photodynamic therapy effects," *Cancer Res.*, vol. 68, pp. 8590–6, 2008.
- [5] R. E. Baddour and M. C. Kolios, "The fluid and elastic nature of nucleated cells: implications from the cellular backscatter response," *J. Acoust. Soc. Am.*, vol. 121, pp. EL16–22, 2007.
- [6] J. W. Hunt, A. E. Worthington, A. Xuan, M. C. Kolios, G. J. Czarnota, and M. D. Sherar, "A model based upon pseudo regular spacing of cells combined with the randomisation of the nuclei can explain the significant changes in high-frequency ultrasound signals during apoptosis," *Ultrasound Med. Biol.*, vol. 28, pp. 217–26, 2002.
- [7] L. R. Taggart, R. E. Baddour, A. Giles, G. J. Czarnota, and M. C. Kolios, "Ultrasonic characterization of whole cells and isolated nuclei," *Ultrasound Med. Biol.*, vol. 33, pp. 389–401, 2007.

- [8] T. E. Doyle, K. H. Warnick, and B. L. Carruth, "Histology-based simulations for the ultrasonic detection of microscopic cancer in vivo," *J. Acoust. Soc. Am.*, vol. 122, pp. EL210–6, 2007.
- [9] D. Savery and G. Cloutier, "Effect of red cell clustering and anisotropy on ultrasound blood backscatter: a monte carlo study," *IEEE Trans. Ultrason. Ferroelectr. Freq. Control*, vol. 52, pp. 94–103, 2005.
- [10] P. Louis and A. M. Gokhale, "Computer simulation of spatial arrangement and connectivity of particles in three-dimensional microstructure: Application to model electrical conductivity of polymer matrix composite," *Acta Mater.*, vol. 44, pp. 1519–28, 1996.
- [11] M. I. Daoud and J. C. Lacefield, "Stochastic modeling of tissue microstructure for high-frequency ultrasound imaging simulations," in *Proc. SPIE*, vol. 7262, 2009, p. 72620P.
- [12] J. Mamou, M. L. Oelze, W. D. O'Brien Jr., and J. F. Zachary, "Identifying ultrasonic scattering sites from three-dimensional impedance maps," *J. Acoust. Soc. Am.*, vol. 117, pp. 413–23, 2005.
- [13] R. C. Waag, J. O. Nilsson, and J. P. Astheimer, "Characterization of volume scattering power spectra in isotropic media from power spectra of scattering by planes," *J. Acoust. Soc. Am.*, vol. 74, pp. 1555–1571, 1983.
- [14] I. J. Fidler, "Selection of successive tumour lines for metastasis," *Nat. New Biol.*, vol. 242, pp. 148–9, 1973.
- [15] K. C. Graham, L. A. Wirtzfeld, L. T. MacKenzie, C. O. Postenka, A. C. Groom, I. C. MacDonald, A. Fenster, J. C. Lacefield, and A. F. Chambers, "Three-dimensional high-frequency ultrasound imaging for longitudinal evaluation of liver metastases in preclinical models," *Cancer Res.*, vol. 65, pp. 5231–7, 2005.

- [16] A. E. Carpenter, T. R. Jones, M. R. Lamprecht, C. Clarke, I. H. Kang, O. Friman, D. A. Guertin, J. H. Chang, R. A. Lindquist, J. Moffat, P. Golland, and D. M. Sabatini, "Cellprofiler: image analysis software for identifying and quantifying cell phenotypes," *Genome Biol.*, vol. 7, pp. R100+, 2006.
- [17] M. D. Abramoff, P. J. Magelhaes, and S. J. Ram, "Image processing with imagej," *Biophotonics International*, vol. 11, pp. 36–42, 2004.
- [18] R. T. DeHoff and F. N. Rhines, "Measurement of volume in volume," in *Quantitative Microscopy*. New York: McGraw-Hill, 1968, ch. 3.
- [19] A. H. Holmes, *Petrographic Methods and Calculations*. London: Murby and Company, 1927.
- [20] R. T. DeHoff and F. N. Rhines, "Particle size distribution," in *Quantitative Microscopy*. New York: McGraw-Hill, 1968, ch. 6.
- [21] P. Louis and A. M. Gokhale, "Application of image analysis for characterization of spatial arrangements of features in microstructure," *Metall. Mater. Trans.*, vol. 26A, pp. 1449–56, 1995.
- [22] M. N. M. Van Lieshout, "Markov point processes," in *Markov Point Processes and Their Applications*. London: Imperial College Press, 2001, ch. 2.
- [23] N. Metropolis, A. W. Rosenbluth, M. N. Rosenbluth, A. H. Teller, and E. Teller, "Equation of state calculations by fast computing machines," *J. Chem. Phys.*, vol. 21, pp. 1087–92, 1953.
- [24] A. Grama, A. Gupta, G. Karypis, and V. Kumar, "Programming shared address space platforms," in *Introduction to Parallel Computing*, 2nd ed. Harlow, England: Addison-Wesley, 2003, ch. 7.

- [25] J. W. Hunt, A. E. Worthington, and A. T. Kerr, “The subtleties of ultrasound images of an ensemble of cells: simulation from regular and more random distributions of scatterers,” *Ultrasound Med. Biol.*, vol. 21, pp. 329–41, 1995.

Chapter 4

Three-Dimensional Computational Modeling of High-Frequency Ultrasound Imaging of a Mouse Liver Metastasis Model

The content of this chapter is in preparation to be submitted to IEEE Transactions on Biomedical Engineering with author list M. I. Daoud and J. C. Lacefield.

4.1 Introduction

High-frequency (20-60 MHz) ultrasound imaging can be used to detect tissue microanatomical changes that occur during tumour growth [1] and anti-cancer treatment response [2] in preclinical cancer models. Investigating the relationships between high-frequency ultrasound backscattering and tissue microanatomy is a challenging problem that would extend the use of high-frequency ultrasound imaging to provide information about tumour microstructure. Spectral analyses [3] of high-frequency ultrasound backscattered signals were used to obtain preliminary estimates of the

microstructure of skin tissue [4], various tumour types [5], and the microscopic variations associated with cell death [6] and anti-cancer radiotherapy [7] in cell ensembles. An alternative approach to relate high-frequency ultrasound scattering to tissue microanatomy is to use ultrasound scattering models that solve the forward scattering problem, defined as computing acoustic scattering given a description of the incident wave and the propagation medium.

Several scattering models have been reported in the literature that suggest the morphology and spatial organization of cells and nuclei as the main determinants of ultrasound scattering at the high-frequency band. For example, Baddour *et al.* [8] showed that the high-frequency scattering response of a single cell can be predicted using analytical models that treat the cell as a sphere. Idealized one-dimensional and two-dimensional (2-D) scattering models proposed by Hunt *et al.* [9] represented tissue microstructure as a group of weakly scattering point-like nuclei embedded in a lossless homogeneous medium. The 2-D scattering model of [9] was extended in [10] to include morphological properties of the nucleus by representing each nucleus as a group of point-like scatterers. Simulations performed with these models suggest that variations of the spatial arrangement and structure of nuclei can significantly change the characteristics of high-frequency ultrasound backscattering. These concepts were combined by Doyle *et al.* [11], who presented a three-dimensional (3-D) scattering model that treats tissue microstructure as a group of spherical cells embedded in an extracellular matrix, where each cell is represented as a spherical nucleus surrounded with cytoplasm. High-frequency ultrasound scattering simulations were performed using the 3-D model with several hundred cells configured to produce a variable ratio of cell to nucleus diameter and various spatial arrangements of cells. In these simulations, 3-D acoustic propagation was computed using a multiple-scattering method [12] without incorporating attenuation. The simulations showed that high-frequency ultrasound scattering in tissue may be correlated with the structure and spatial organization of cells and nuclei.

Ultrasound scattering models derived from histology data are crucial to validate modeling results because histology-based models enable simulations performed with the scattering models to be compared with matching experimental ultrasound measurements. This approach was used by Mamou *et al.* [13], who presented a 3-D computational tissue model that was constructed by mapping tissue microscopic structures to corresponding acoustic impedance values. The mapping process was achieved by fixing, slicing, and staining a tissue volume to obtain a group of adjacent 2-D histology slides in which each colour corresponds to a specific tissue type. The 2-D histology slides were digitized, aligned, and processed to construct a 3-D impedance matrix of the tissue volume. The impedance-based tissue model was used to estimate the average scatterer size and acoustic concentration of two mammary tumours. The estimation is performed by deriving an analytical formula to compute the backscattered intensity based on the impedance matrix. Comparisons with ultrasound data showed good matching between the estimated scatterer size and the scatterer size obtained ultrasonically. However, significant deviation was observed between the estimated acoustic concentration and the acoustic concentration obtained with ultrasound data.

An alternative approach to study high-frequency ultrasound scattering in tissue based on histology data is to carry out ultrasound scattering simulations using simulated tissue volumes with microscopic morphological and spatial arrangement statistics that match experimental tissue specimens. Such simulated tissue volumes can be created using the 3-D stochastic tissue model [14] proposed by Daoud and Lacefield. To use the stochastic tissue model to create a simulated tissue volume with the microstructural properties of a given tissue specimen, random histology slides obtained from the specimen were stained to highlight cells and nuclei. The stained slides were digitized at $20\times$ magnification and analyzed to estimate morphological properties that include the nuclear volume fraction, the size distribution of nuclei, and the maximum ratio of cell to nucleus diameter. The simulated tissue volume was initialized by creating a population of uniformly distributed cells embedded in

a homogeneous extracellular matrix, where each cell was represented as a spherical nucleus surrounded by homogeneous cytoplasm. The nucleus size, cell size, and the total number of cells in the tissue volume were determined based on the morphological properties estimated for the specimen. The 3-D spatial arrangement of cells in the tissue volume was controlled by a Gibbs-Markov point process. The parameters of the Gibbs-Markov process were tuned to accurately reproduce the spatially varying number density and centre-to-centre spacing of cells in the tissue specimen. The spatial arrangement of cells in both the tissue specimen and the simulated tissue was characterized using spatial descriptors adopted from materials science. The tissue model was used in [14] to create simulated healthy and tumour tissues with the structural properties of normal and cancerous murine liver specimens, respectively. In this paper, the phrase *simulated tissues* will refer specifically to simulated tissues created with the stochastic tissue model.

Large-scale high-frequency ultrasound scattering simulations with propagation volumes on the order of tens or hundreds of wavelengths require 3-D ultrasound simulators that achieve high accuracy with reasonable running time. One ultrasound simulator that enables accurate and fast acoustic propagation in large-scale tissue volumes is the parallel 3-D simulator presented in [15, 16]. The parallel simulator uses a 3-D formulation of a k -space method [17] to compute linear propagation of the total pressure in fluid media. This k -space method solves first-order wave equations, and hence multiple scattering is implicitly incorporated. Acoustic propagation obtained using the first-order k -space method with coarse spatial and time steps is exact for homogenous media and highly accurate for weakly scattering inhomogeneous media such as soft tissue. Linear frequency-dependent absorption is included in the simulator using a second-order relaxation model [18]. The implementation of the simulator supports parallel computing using distributed-memory computer clusters, and hence large-scale simulations can be performed with short running times. The simulator was used in [19] to perform B-mode imaging simulations with a focused high-frequency

transducer. The simulated B-mode images showed realistic 3-D refraction artefacts that cannot be obtained using 2-D simulations. These artefacts demonstrate the importance of computing 3-D ultrasound propagation to achieve realistic simulations.

Other studies [9–11, 20, 21] have suggested that the microstructural features incorporated in the stochastic tissue model, including the cell number density, the cell and nucleus sizes, and the spatial arrangement of cells, are major determinants of high-frequency ultrasound scattering in tissue. However, the accuracy of ultrasound scattering models that include only these structural features has not been investigated. This paper explores the issue of whether ultrasound simulations performed using the stochastic tissue model can estimate high-frequency ultrasound scattering in normal and cancerous murine liver tissues. The study is carried out by computing high-frequency ultrasound scattering in simulated healthy and tumour tissues configured using the stochastic model to match the microstructure of healthy mouse liver and an experimental liver metastasis, respectively. Ultrasound propagation in the simulated tissues is performed using the parallel 3-D ultrasound simulator and the computed backscattered signals are processed to synthesized B-mode images of each simulated tissue. The complexity of the simulation is reduced by assigning the extracellular matrix the acoustic properties of cell cytoplasm, and hence tissue microstructure is treated as a population of nuclei embedded in homogeneous background. The simulations show good matching between the first-order speckle statistics of the B-mode images synthesized for the simulated healthy tissue and experimental B-mode images of healthy murine liver. Reasonable matching is achieved between the first-order speckle statistics of the synthesized B-mode images of the simulated tumour and experimental images of the matching liver metastasis when nucleus sound speed and mass density values are used that are different from the values assumed for healthy tissue.

4.2 Methods

4.2.1 Experimental ultrasound imaging

An experimental liver metastasis model was prepared by injecting 3×10^5 B16F1 murine melanoma [22] cells into the mesenteric vein of a female C57BL/6 mouse (Harlan, Indianapolis, IN) as described in [23] to target the liver. Tumour growth was monitored with 3-D high-frequency ultrasound as described in [23]. When tumours of ~ 1 mm diameter were observed, the part of the abdominal wall that covers a tumour located at the liver surface was removed, and the liver lobe that includes the tumour was imaged. Animal experiments were performed in accordance to the Canadian Council on Animal Care under a protocol approved by the University of Western Ontario Animal Use Subcommittee.

Ultrasound imaging was carried out using a Vevo 770 (VisualSonics, Toronto, Canada) high-frequency ultrasound scanner. A previous generation of this ultrasound system was described in [24]. The scanner employed a VisualSonics RMV704 scanhead that has a mechanically-scanned, single-element, spherically focused transducer with a 6.0-mm focal distance, a 3.0-mm aperture diameter, a 40-MHz centre frequency, a f -number of 2.0, and a measured [25] -6 -dB fractional bandwidth of 80%. The resolution at the focus is 40 (axial) \times 80 (lateral) \times 80 (elevation) μm^3 with a 1.5-mm depth of field. The axial direction is along the axis of the ultrasound beam, the lateral direction is perpendicular to the axis of the ultrasound beam, and the elevation direction is along the out of plane axis. The transducer was positioned such that the region of interest could be defined that extended from 0.14 to 0.29 mm above the focus across the width of the tumour. The same scanning set-up was used to image a healthy region of the liver. Parallel 2-D B-mode images with a 8.0×8.0 mm² field of view were acquired by stepping the transducer in 31.8- μm intervals along the elevation dimension. A 3-D B-mode image of volume $8.0 \times 8.0 \times 4.0$ mm³ was reconstructed from the 2-D images using the algorithm described in [26]. Each voxel

in the 3-D B-mode image has a size of $15.6 \times 15.6 \times 31.8 \mu\text{m}^3$ and a gray level value between 0 and 255.

4.2.2 Modeling tissue microstructure

Tissue specimens were obtained from the region of interest of the liver metastasis model's imaged tumour and a healthy C57BL/6 mouse's liver to simulate their microstructures using the stochastic tissue model summarized in the introduction and described fully in [14]. Each tissue specimen was analyzed as described in section II.A in [14] to determine its microstructural properties, including the nuclear volume fraction, size distribution of nuclei, ratio of cell to nucleus diameter, and spatial arrangement of nuclei within the tissue. A simulated healthy tissue and a simulated tumour with the microstructural properties of the healthy liver specimen and the experimental metastasis specimen, respectively, were synthesized as described in sections II.C and II.D in [14]. Similar to [14], each simulated tissue included nine groups of nuclei with diameters between 1.2 and 10.8 μm , with an increment of 1.2 μm . The volume of each simulated tissue is $720 \times 600 \times 600 \mu\text{m}^3$, which provides a reasonable propagation volume to perform high-frequency B-mode imaging simulations. The stochastic tissue model was run on 64 nodes of a shared-memory computer cluster.

Cell cytoplasm in both simulated tissues is assigned a sound speed that matches the value of a whole cell, 1535 m/s [20], and a mass density of 1044 kg/m³ [27]. The sound speed and mass density of nuclei in the simulated healthy tissue are set to 1503 m/s [20] and 1430 kg/m³ [28]. Eight combinations of nucleus sound speed and mass density are tested for the simulated tumour that are between the values assumed for healthy tissue nuclei, (1503 m/s, 1430 kg/m³), and values close to cell cytoplasm, (1531 m/s, 1092 kg/m³), with an increment of (4.0 m/s, -48.3 kg/m³). The complexity of the simulated tissues is reduced by assigning the extracellular matrix the acoustic properties of cell cytoplasm. Therefore, tissue microstructure is

treated as a population of nuclei embedded in a homogeneous background.

4.2.3 Ultrasound imaging simulation

The parallel 3-D ultrasound simulator described briefly in the introduction and presented fully in [15, 16] was used to simulate ultrasound pulse-echo acquisitions. Computing round-trip ultrasound propagation over the actual 6-mm distance from the transducer to the focal zone at each scan line simulation would require extensive computational resources. The simulation complexity was reduced using the aperture projection technique presented in [19] that restricts the simulation to a field of view around the focus. The reduction of the field of view is achieved by modeling the VisualSonics RMV704 transducer as a small spherically focused aperture with a short focal distance of $0.472 \mu\text{m}$ and an f -number, a centre frequency, and -6 -dB fractional bandwidth that match the modeled transducer. The incident pulse used in the simulation has a Gaussian envelope that is low-pass filtered using a finite impulse response filter based on the window method with a cut-off frequency of 32 MHz to avoid overlap between the positive and negative frequencies of the incident pulse that otherwise occurs due to the large bandwidth employed. A scan line is computed by transmitting the incident pulse from the projected aperture into the propagation medium and recording the echoes received by the aperture as a radio-frequency (RF) signal. Matching the f -number and centre frequency enables the projected aperture to have the same lateral and elevation resolution and depth of field as the RMV704 transducer [19]. The axial resolution of a focused spherical transducer is inversely proportional to the bandwidth [24], and hence matching the bandwidth allows the projected aperture to have the same axial resolution as the modeled transducer.

Four parallel B-mode image planes are obtained for the simulated healthy tissue when the centre of the transducer is located at z (elevation) coordinates of 0.138, 0.246, 0.354, and 0.462 mm. Each image is composed of 13 scan lines that are equally-spaced by $36 \mu\text{m}$ along the x (lateral) dimension. Similar images are separately

obtained for the simulated tumour using each combination of nucleus sound speed and mass density tested. The scan lines are acquired when the projected aperture is located in a plane at y (axial) = -0.46 mm so that the focus will be on the xz plane ($y = 0$). The field of view of each scan line extends 0.492 mm along the axial dimension, which approximates the axial range of the B-mode images of the regions of interest of the healthy liver and experimental metastasis.

The simulation of each scan line is performed using a computation grid of $256 \times 512 \times 256$ points with a spatial step of $1 \mu\text{m}$. The k -space method employed by the simulator requires four points per minimum wavelength, or a spatial step of $4.7 \mu\text{m}$ for the incident pulse described above in a background medium with the sound speed of cell cytoplasm, to carry out accurate imaging simulations [19]. The fine spatial step of $1 \mu\text{m}$ is required to achieve a small discretization error between 0.5% and 9.5% of the diameter of each nucleus that is produced by representing the nine nuclei groups using a finite number of voxels. The time step is set to 0.326 ns based on the recommended configuration [19] of the k -space method to perform realistic imaging simulations. Accuracy analysis reported in [19] suggests that the ultrasound simulator with the spatial and time step configurations employed in this study achieves a propagation error smaller than 0.6% . The ultrasound simulator is configured to model linear frequency-dependent absorption with the absorption coefficient of a whole acute myeloid leukemia cell [29] of 0.805 dB/cm/MHz [20].

The simulated B-mode images are synthesized by processing the RF scan lines through envelope detection, logarithmic compression, and quantization in a manner similar to the Vevo 770 scanner. The logarithmic compression and signal quantization of the Vevo 770 scanner are described by [30]:

$$DG = 369.36 \ln(EV) + 371.86 \quad (4.1)$$

where EV is the normalized envelope of an RF scan line and DG is an 11-bit digital output signal.

A B-mode image is synthesized in the Vevo 770 scanner by linearly mapping the values of its scan lines' DG signals, which have an absolute range of $[0, 2047]$, to gray level values with an absolute range of $[0, 255]$. This display dynamic range compression is applied to create the simulated B-mode images after multiplying the RF signals of all scan lines by a scaling factor. The scaling factor is required to compensate for the gains of the transducer and the receive electronics that are not included in the simulation. The value of the scaling factor is computed such that the nominal maximum gray level value observed in the experimental B-mode images of both the healthy liver and the experimental metastasis matches the maximum gray level value of all synthesized B-mode images.

4.2.4 B-mode image analysis

The four synthesized B-mode images of the simulated healthy tissue are compared using first-order speckle statistics with six B-mode images of a healthy region in the mouse's liver. The out-of-plane spacing between B-mode images is $127.2 \mu\text{m}$ for the experimental images and $108 \mu\text{m}$ for the simulated images. These spacings ensure independent B-mode images because they are coarser than the elevational resolution of the Vevo 770 scanner. Similar statistical comparisons are separately performed between each set of four B-mode images synthesized for the simulated tumour using different combinations of nucleus sound speed and mass density tested and the same four B-mode regions of interest of the experimental metastasis.

The four synthesized B-mode images of the simulated healthy tissue are sampled using a grid with $62.1 \mu\text{m}$ axial spacing and $108 \mu\text{m}$ lateral spacing to obtain 25 independent samples from each image. Sample spacing coarser than the ultrasound imaging resolution is employed to obtain pixels from independent scattering sites. A histogram with 13 gray level bins, which have mean gray level values between 10 and 250 with an increment of 20, is computed for each set of 25 pixels. The mean histogram of the simulated healthy tissue is computed by averaging the pixel counts

of the corresponding four B-mode images' histograms at each gray level bin. Similar averaged histograms are computed for each set of four B-mode images synthesized for the simulated tumour.

The six B-mode images of the healthy liver are sampled using a grid with $62.5 \mu\text{m}$ axial spacing and $109.4 \mu\text{m}$ lateral spacing to obtain a sample of 50 pixels from each image. The four B-mode images of the liver metastasis are sampled in a similar manner to obtain 80, 40, 29, and 11 pixels, respectively, from the region of interest of the imaged tumour. The variable number of pixels obtained from the B-mode images of the experimental metastasis is due to the spherical shape of the tumour. The pixels obtained from the liver metastasis are arranged into four groups of 40 pixels each by dividing the pixels of the first B-mode image into two groups and combining the pixels of the last two images into one group. A histogram with 13 gray level bins, similar to the histograms of the simulated B-mode images, is computed for each 40-pixel group. The mean \pm standard deviation histograms of gray levels in the healthy liver and the tumour region of interest are determined by computing the average and standard deviation of the pixel counts of the corresponding histograms of the 40-pixel groups at each gray level bin.

4.3 Results

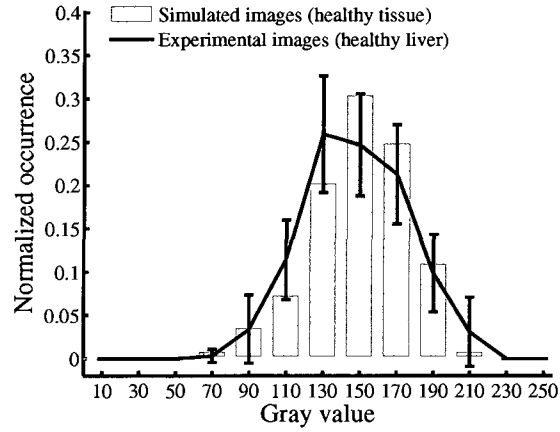
4.3.1 Healthy mouse liver

The averaged gray level histogram of the synthesized B-mode images of the simulated healthy tissue is compared in Fig. 4.1(a) with the mean \pm standard deviation histogram of the B-mode images of the healthy liver. The mean \pm standard deviation gray level values of the histograms of the simulated and experimental images are 150 ± 26.5 and 148 ± 27.9 , respectively. The normalized occurrence in each gray level bin for the simulated healthy tissue lies within one standard deviation of the mean

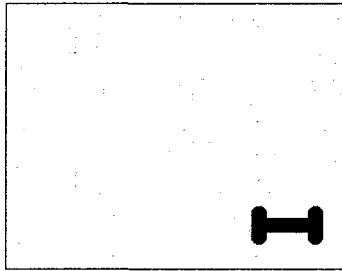
normalized occurrence data for the experimental images for all of the 13 gray level bins computed. The gray-level histograms for the simulated and experimental images have the same number of gray level bins with non-zero counts. Fig. 4.1(a) demonstrates that the first-order speckle statistics of the simulated healthy tissue is similar to the healthy liver. An example $328 \mu\text{m} \times 453 \mu\text{m}$ experimental B-mode image of healthy liver and a comparable synthesized B-mode image of the simulated healthy tissue are shown in Fig. 4.1(b) and Fig. 4.1(c), respectively. For display purposes, the example simulated B-mode images presented here are axially downsampled and linearly interpolated across the lateral dimension to obtain a $15.5 \times 15.5 \mu\text{m}^2$ pixel size that approximates the pixel size of the experimental images of $15.6 \times 15.6 \mu\text{m}^2$.

4.3.2 Experimental liver metastasis

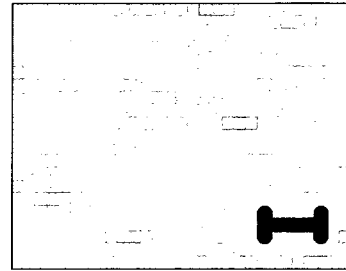
The averaged gray level histogram of the B-mode images synthesized for the simulated tumour with nucleus sound speed and mass density that match the values assumed for healthy tissue is compared in Fig. 4.2(a) with the mean \pm standard deviation histogram of the experimental images of the liver metastasis. The mean \pm standard deviation gray level values of the histograms of the simulated and experimental images are 145.9 ± 25.8 and 107.1 ± 28.5 , respectively. Substantial deviation is observed between the histograms of the simulated and experimental tumour images, where the normalized occurrence in each gray level bin for the simulated images lies within one standard deviation of the mean normalized occurrence data for the experimental images for only 7 out of the 13 gray level bins analyzed. The highest gray level bin with non-zero counts for the experimental and simulated tumours is located at 190, which is lower than the highest gray level bin with non-zero counts, at 210, observed for the simulated healthy tissue and the healthy liver. Example $328 \mu\text{m} \times 453 \mu\text{m}$ B-mode images of the liver metastasis and the simulated tumour with the acoustic properties assumed for healthy tissue are shown in Fig. 4.2(b) and Fig. 4.2(c), respectively.



(a)



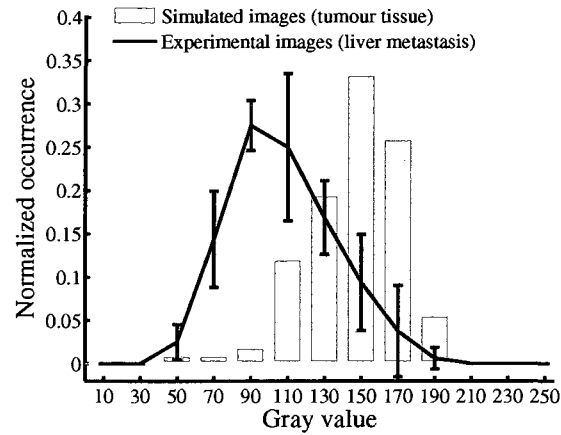
(b)



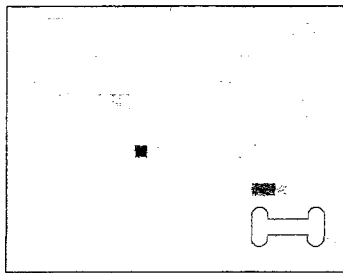
(c)

Fig. 4.1: Comparison of experimental B-modes images of healthy murine liver tissue and synthesized B-mode images of simulated healthy tissue. (a) Gray level histograms of six B-mode images of healthy liver tissue and four synthesized B-mode images of simulated healthy tissue; (b) an experimental B-mode image of healthy liver; (c) a synthesized B-mode image of simulated healthy tissue. Error bars indicate mean \pm standard deviation of the gray level histograms of the six experimental B-mode images. Scale bar = $94 \mu\text{m}$.

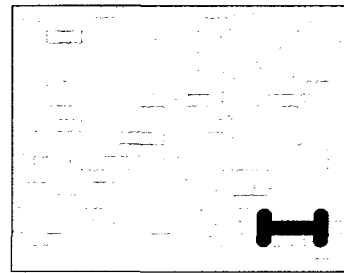
The number of matching normalized occurrence counts between the gray level histogram of the images of the simulated tumour and the mean \pm standard deviation of the histogram of the images of the experimental metastasis is maximized when the nucleus sound speed and mass density of the simulated tumour are set to 1527 m/s and 1140.5 kg/m^3 .



(a)



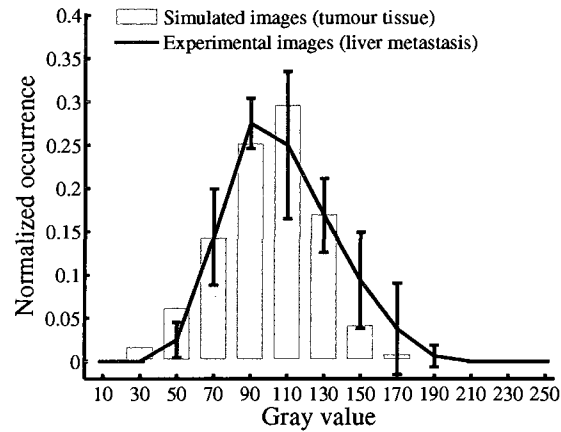
(b)



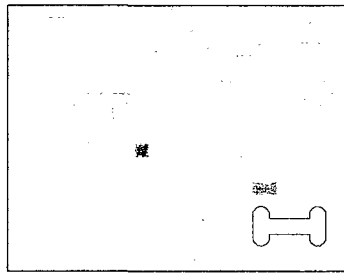
(c)

Fig. 4.2: Comparison of experimental B-modes images of a liver metastasis and simulated B-mode images synthesized for a simulated tumour with the nucleus sound speed and mass density values assumed for healthy tissue. (a) Gray level histograms of four B-mode images of an experimental liver metastasis and four B-mode images synthesized for a simulated tumour using the acoustic properties assumed for healthy tissue; (b) an experimental B-mode image of an experimental liver metastasis; (c) a B-mode image synthesized for a simulated tumour using the acoustic properties assumed for healthy tissue. Error bars indicate mean \pm standard deviation of the gray level histograms of the four experimental B-mode images. Scale bar = $94 \mu\text{m}$.

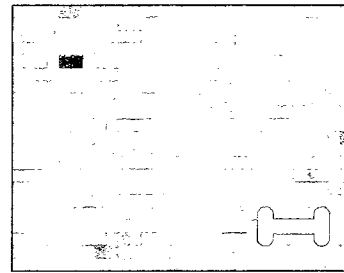
The averaged histogram of the B-mode images synthesized for the simulated tumour using the optimized nucleus sound speed and mass density values is compared in Fig. 4.3(a) with the mean \pm standard deviation histogram of the experimental B-mode



(a)



(b)



(c)

Fig. 4.3: Comparison of experimental B-modes images of a liver metastasis and simulated B-mode images synthesized for a simulated tumour using nucleus sound speed and mass density of 1527 m/s and 1140.5 kg/m³ that are different from the values assumed for healthy tissue. (a) Gray level histograms of four B-mode images of an experimental liver metastasis and four B-mode images synthesized for a simulated tumour using nucleus acoustic properties different from the values assumed for healthy tissue; (b) an experimental B-mode image of an experimental liver metastasis; (c) a B-mode image synthesized for a simulated tumour using nucleus acoustic properties different from the values assumed for healthy tissue. Error bars indicate mean \pm standard deviation of the gray level histograms of the four experimental B-mode images. Scale bar = 94 μ m.

images of the liver metastasis. The mean \pm standard deviation gray level values of the histograms of the simulated and experimental images are 99.6 ± 27.2 and 107.1 ± 28.5 , respectively. The normalized occurrence in each gray level bin for the simulated tumour lies within one standard deviation of the mean normalized occurrence data for the experimental metastasis for 11 of the 13 bins computed. The peak of the histogram of the simulated tumour images is located at a gray level bin of 110 that is close to the peak of the histogram of the experimental images at 90. Fig. 4.3(a) demonstrates that the first-order speckle statistics obtained for the simulated tumour with acoustic properties different from the values assumed for healthy tissue is very similar to the experimental metastasis. An example $328 \mu\text{m} \times 453 \mu\text{m}$ experimental B-mode image of the liver metastasis and a comparable synthesized B-mode image of the simulated tumour are shown in Fig. 4.3(b) and Fig. 4.3(c), respectively.

4.4 Discussion

In the process of modeling high-frequency ultrasound scattering in tissue, it is crucial to compute accurate ultrasound propagation with a simulation arrangement that approximates the experimental scanning set-up. The ultrasound simulator employed in this study computes linear acoustic propagation in a fluid medium and uses a relaxation model to include linear frequency-dependent absorption. The simulator provides high modeling accuracy because the incorporated physical processes are the major determinants of high-frequency ultrasound propagation in tissue. The fine spatial and time spacings of $1 \mu\text{m}$ and 0.326 ns enable a low propagation error of less than 1%, which is judged sufficient for B-mode imaging simulations. The representation of the spherical nuclei using $1\text{-}\mu\text{m}^3$ isotropic voxels produces a discretization error between 0.5% for the largest nuclei and 9.5% for the smallest nuclei. Finer spatial steps are avoided because the computational resources required by the ultrasound simulator are inversely proportional to the fourth power of the spatial step size [19].

The healthy liver and the experimental metastasis are imaged such that the regions of interest are located above the transducer's focus within the focal zone to avoid the large drop in B-mode images brightness observed below the focus. Small regions of interest are used in the analysis to reduce the effect of tissue-scale structures, such as liver lobules and blood vessels, and the heterogeneity of the experimental metastasis that are not included in the stochastic tissue model [14]. The experimental scanning set-up is modeled by employing the aperture projection technique of [19] to compute scan lines with fields of view that approximate the axial range of the B-mode images of the regions of interest of the healthy liver and experimental metastasis. One difference between the experimental and simulated B-mode images is the number of scan lines per unit distance, where the lateral spacing between the simulated scan lines is equal to $36 \mu\text{m}$ compared to a spacing of $21.2 \mu\text{m}$ between the lines of the experimental images [25].

The ultrasound simulator and the tissue model have high computational complexity, and therefore only four simulated B-mode images of small size are synthesized to study high-frequency ultrasound scattering in each tissue specimen. The simulated tissues used in the analyses do not include a simulated tumour surrounded with simulated healthy tissue, which mimics the anatomy of the liver of the metastasis mouse model, because at each simulation run the tissue model can be tuned to match the average microstructural properties of only one type of tissue specimen (liver or metastasis).

Ultrasound simulations performed using the simulated healthy and tumour tissues, in which tissue is treated as a population of spherical nuclei embedded in a background with the acoustic properties of cytoplasm, provide some information about high-frequency ultrasound scattering in tissue. The simulation results presented in Fig. 4.1 show good matching between the first-order speckle statistics of the synthesized B-mode images of the simulated healthy tissue and experimental B-mode images of a healthy region in the mouse's liver. The good matching between the first-order speckle

statistics of the simulated and experimental images is consistent with the hypothesis that cell nuclei are major sources of high-frequency ultrasound scattering in tissue. Moreover, these results agree with the empirical study of [20] that showed correlation between ultrasound backscattering from cell ensembles and the sizes of the nuclei.

The simulated tumour results presented in Fig. 4.2 show substantial deviation between the gray level histogram of the B-mode images synthesized for the simulated tumour using the nucleus sound speed and mass density assumed for healthy tissue and the histogram of the experimental metastasis. This result shows that modeling the number density, size distribution, and spatial arrangement of nuclei does not fully describe tissue microscopic variations that determine the characteristics of ultrasound B-mode images of an experimental metastasis. However, the histograms of the simulated tumour and the experimental metastasis have the same highest gray level bin with non-zero counts, at 190, that is lower than the highest gray level bin with non-zero counts, at 210, obtained for the simulated and experimental healthy tissues. This reduction in the amplitude of the backscattered ultrasound signals is produced by the difference in microstructural properties of the healthy liver and experimental metastasis [14].

Good agreement is shown in Fig. 4.3 between the first-order speckle statistics of the synthesized B-mode images of the simulated tumour and the experimental images of the liver metastasis when the tumour tissue nuclei are assumed to have sound speed and mass density values of 1527 m/s and 1140.5 kg/m³ that are not equal to the values of 1503 m/s and 1430 kg/m³ assumed for healthy tissue nuclei. The difference between the acoustic properties assumed for tumour tissue nuclei and the values assumed for cell cytoplasm, 1535 m/s and 1044 kg/m³, is smaller than the difference between the acoustic properties assumed for healthy tissue nuclei and cell cytoplasm. These simulations suggest that changes in both the acoustic and microstructural properties of tissue are responsible for variations in first-order speckle statistics between healthy liver and the experimental metastasis.

Since the simulated healthy and tumour tissue model includes only cell nucleus and cytoplasm, the effect of other cellular-scale structures such as cell membranes and extracellular matrix is not included in the simulations. Anatomic structures such as liver lobules and blood vessels are not incorporated in the tissue model, and hence the spatial arrangement of nuclei in the simulated tissues is presumably less structured than the experimental tissues.

Visual comparison between the synthesized B-mode images of the simulated healthy and tumour tissues and the experimental images of the healthy region in the mouse's liver and the liver metastasis, respectively, show less structured patterns in the simulated images than the experimental images. This difference in image texture might be due to the cellular- and tissue-scale structures that are not included in the simulated tissues. Moreover, abnormal structural variations in the healthy region of the metastasis model's liver might be the source of some structured patterns in the experimental images of the liver tissue. Such abnormal variations are not included in the simulated healthy tissue that is configured to match the microstructure of a liver specimen obtained from a healthy mouse.

4.5 Conclusion

Ultrasound scattering simulations have been performed using simulated healthy and tumour tissues that are configured to produce the number density, size distribution, and spatial arrangement of nuclei in healthy liver and an experimental liver metastasis specimen. The results show good agreement between the first-order speckle statistics of the synthesized B-mode images of the simulated healthy tissue and experimental images of healthy liver. This agreement is consistent with the hypothesis that the nuclei are major sources of high-frequency ultrasound scattering. Moreover, the results show good matching between the first-order speckle statistics of the B-mode images synthesized for the simulated tumour and images of the experimental metas-

tasis when nucleus sound speed and mass density values are used that are different from the values assumed for healthy tissue. These simulations suggest that changes in both tissue acoustic and microstructural properties are responsible for variations in the first-order speckle statistics of high-frequency ultrasound B-mode images that accompany tumour growth.

References

- [1] D. H. Turnbull, J. A. Ramsay, G. S. Shivji, T. S. Bloomfield, L. From, D. N. Sauder, and F. S. Foster, "Ultrasound backscatter microscope analysis of mouse melanoma progression," *Ultrasound Med. Biol.*, vol. 22, pp. 845–53, 1996.
- [2] B. Banihashemi, R. Vlad, B. Debeljevic, A. Giles, M. C. Kolios, and G. J. Czarnota, "Ultrasound imaging of apoptosis in tumor response: novel preclinical monitoring of photodynamic therapy effects," *Cancer Res.*, vol. 68, pp. 8590–6, 2008.
- [3] F. L. Lizzi, M. Ostromogilsky, E. J. Feleppa, M. C. Rorke, and M. M. Yaremko, "Relationship of ultrasonic spectral parameters to features of tissue microstructure," *IEEE Trans. Ultrason. Ferroelectr. Freq. Control*, vol. 34, pp. 319–329, 1987.
- [4] C. Guittet, F. Ossant, L. Vaillant, and M. Berson, "*In vivo* high-frequency ultrasonic characterization of human dermis," *IEEE Trans. Biomed. Eng.*, vol. 46, pp. 740–6, 1999.
- [5] M. L. Oelze, W. D. O'Brien Jr, J. P. Blue, and J. F. Zachary, "Differentiation and characterization of rat mammary fibroadenomas and 4T1 mouse carcinomas using quantitative ultrasound imaging," *IEEE Trans. Med. Imaging*, vol. 23, pp. 764–71, 2004.
- [6] M. C. Kolios, G. J. Czarnota, M. Lee, J. W. Hunt, and M. D. Sherar, "Ultrasonic spectral parameter characterization of apoptosis," *Ultrasound Med. Biol.*, vol. 28, pp. 589–97, 2002.
- [7] R. M. Vlad, N. M. Alajez, A. Giles, M. C. Kolios, and G. J. Czarnota, "Quantitative ultrasound characterization of cancer radiotherapy effects *in vitro*," *Int. J. Radiat. Oncol. Biol. Phys.*, vol. 72, pp. 1236–43, 2008.

- [8] R. E. Baddour and M. C. Kolios, "The fluid and elastic nature of nucleated cells: implications from the cellular backscatter response," *J. Acoust. Soc. Am.*, vol. 121, pp. EL16–22, 2007.
- [9] J. W. Hunt, A. E. Worthington, and A. T. Kerr, "The subtleties of ultrasound images of an ensemble of cells: simulation from regular and more random distributions of scatterers," *Ultrasound Med. Biol.*, vol. 21, pp. 329–41, 1995.
- [10] J. W. Hunt, A. E. Worthington, A. Xuan, M. C. Kolios, G. J. Czarnota, and M. D. Sherar, "A model based upon pseudo regular spacing of cells combined with the randomisation of the nuclei can explain the significant changes in high-frequency ultrasound signals during apoptosis," *Ultrasound Med. Biol.*, vol. 28, pp. 217–26, 2002.
- [11] T. E. Doyle, K. H. Warnick, and B. L. Carruth, "Histology-based simulations for the ultrasonic detection of microscopic cancer in vivo," *J. Acoust. Soc. Am.*, vol. 122, pp. EL210–6, 2007.
- [12] T. E. Doyle, "Iterative simulation of elastic wave scattering in arbitrary dispersions of spherical particles," *J. Acoust. Soc. Am.*, vol. 119, pp. 2599–2610, 2006.
- [13] J. Mamou, M. L. Oelze, W. D. O'Brien Jr., and J. F. Zachary, "Identifying ultrasonic scattering sites from three-dimensional impedance maps," *J. Acoust. Soc. Am.*, vol. 117, pp. 413–23, 2005.
- [14] M. I. Daoud and J. C. Lacefield, "Stochastic modeling of normal and tumor tissue microstructure for high-frequency ultrasound imaging simulations," *IEEE Trans. Biomed. Eng.*, In Press.
- [15] M. I. Daoud and J. C. Lacefield, "Parallel three-dimensional simulation of ul-

- trasound imaging,” in *Proc. 22nd Intl. Symp. High Perform. Comp. Sys. Appl.*, 2008, pp. 146–152.
- [16] M. I. Daoud, *Development and validation of parallel three-dimensional computational models of ultrasound propagation and tissue microstructure for preclinical cancer imaging*, Ph.D. thesis, chapter 2, The University of Western Ontario, London, ON, Canada, 2009.
- [17] M. Tabei, T. D. Mast, and R. C. Waag, “A k -space method for coupled first-order acoustic propagation equations,” *J. Acoust. Soc. Am.*, vol. 111, pp. 53–63, 2002.
- [18] A. I. Nachman, J. F. Smith, and R. C. Waag, “An equation for acoustic propagation in inhomogeneous media with relaxation losses,” *J. Acoust. Soc. Am.*, vol. 88, pp. 1584–95, 1990.
- [19] M. I. Daoud and J. C. Lacefield, “Distributed three-dimensional simulation of B-mode ultrasound imaging using a first-order k -space method,” *Phys. Med. Biol.*, In Press.
- [20] L. R. Taggart, R. E. Baddour, A. Giles, G. J. Czarnota, and M. C. Kolios, “Ultrasonic characterization of whole cells and isolated nuclei,” *Ultrasound Med. Biol.*, vol. 33, pp. 389–401, 2007.
- [21] G. J. Czarnota, M. C. Kolios, J. Abraham, M. Portnoy, F. P. Ottensmeyer, J. W. Hunt, and M. D. Sherar, “Ultrasound imaging of apoptosis: high-resolution non-invasive monitoring of programmed cell death in vitro, in situ and in vivo,” *Br. J. Cancer*, vol. 81, no. 3, pp. 520–7, 1999.
- [22] I. J. Fidler, “Selection of successive tumour lines for metastasis,” *Nat. New Biol.*, vol. 242, pp. 148–9, 1973.

- [23] K. C. Graham, L. A. Wirtzfeld, L. T. MacKenzie, C. O. Postenka, A. C. Groom, I. C. MacDonald, A. Fenster, J. C. Lacefield, and A. F. Chambers, "Three-dimensional high-frequency ultrasound imaging for longitudinal evaluation of liver metastases in preclinical models," *Cancer Res.*, vol. 65, pp. 5231–7, 2005.
- [24] F. S. Foster, M. Y. Zhang, Y. Q. Zhou, G. Liu, J. Mehi, E. Cherin, K. A. Harasiewicz, B. G. Starkoski, L. Zan, D. A. Knapik, and S. L. Adamson, "A new ultrasound instrument for in vivo microimaging of mice," *Ultrasound Med. Biol.*, vol. 28, pp. 1165–72, 2002.
- [25] Z. Khan, D. R. Boughner, and J. C. Lacefield, "Anisotropy of high-frequency integrated backscatter from aortic valve cusps," *Ultrasound Med. Biol.*, vol. 34, pp. 1504–12, 2008.
- [26] A. Fenster, D. B. Downey, and H. N. Cardinal, "Three-dimensional ultrasound imaging," *Phys. Med. Biol.*, vol. 46, pp. R67–99, 2001.
- [27] K. C. Vinnakota and J. B. Bassingthwaighite, "Myocardial density and composition: a basis for calculating intracellular metabolite concentrations," *Am. J. Physiol. Heart Circ. Physiol.*, vol. 286, pp. H1742–9, 2004.
- [28] R. E. Baddour, M. D. Sherar, J. W. Hunt, G. J. Czarnota, and M. C. Kolios, "High-frequency ultrasound scattering from microspheres and single cells," *J. Acoust. Soc. Am.*, vol. 117, pp. 934–43, 2005.
- [29] C. Wang, P. Koistinen, G. S. Yang, D. E. Williams, S. D. Lyman, M. D. Minden, and E. A. McCulloch, "Mast cell growth factor, a ligand for the receptor encoded by c-kit, affects the growth in culture of the blast cells of acute myeloblastic leukemia," *Leukemia*, vol. 5, pp. 493–499, 1991.
- [30] VisualSonics Inc., Toronto, ON, Canada, *VisualSonics white paper - linearizing*

contrast mode video data on the Vevo 770 high-frequency ultrasound imaging system, June 2007.

Chapter 5

Summary and Future Work

5.1 Summary

A three-dimensional (3-D) parallel ultrasound simulator and a 3-D computational model of tissue microstructure were developed to investigate the relationships between tissue microanatomy and high-frequency ultrasound backscattering. Preliminary simulations have been performed to demonstrate the feasibility of using this software to relate first-order speckle statistics of ultrasound B-mode images to acoustic and structural properties of tissue microanatomy. The research contributions and results described in each chapter of this thesis are summarized below.

5.1.1 Chapter 2: Distributed three-dimensional simulation of B-mode ultrasound imaging using a first-order k -space method

A parallel ultrasound simulator is presented based on a 3-D formulation of a k -space method that incorporates relaxation absorption and nonreflecting boundary conditions. The simulator, which runs on distributed-memory computer clusters, partitions the computation grid of a single scan line between a group of cluster nodes

and employs multiple groups of nodes to compute independent lines concurrently. The accuracy of the simulator is demonstrated by computing scattering from a fluid sphere and comparing the results with a matching analytical solution. Accuracy results show that the simulator, with a coarse spatial step of four points per wavelength and a CFL number of 0.5, achieves a low error value of 2.6% when the medium is filtered using a Gaussian filter. An aperture-projection technique is presented to minimize the computational resources of imaging simulations with a focused transducer by restricting the simulation to a small field of view around the focus. This technique is employed to synthesize B-mode images of a tissue-mimicking phantom that show realistic 3-D refraction artefacts. Parallel computing using 20 nodes reduced the execution time for each image to 18.6 hours, compared to a serial execution time of 357.5 hours. The results demonstrate that fully 3-D imaging simulations are practical using contemporary computing technology.

5.1.2 Chapter 3: Stochastic modeling of normal and tumour tissue microstructure for high-frequency ultrasound imaging simulations

A 3-D microanatomical model is introduced in which tissue is treated as a population of stochastically positioned spherical cells consisting of a spherical nucleus surrounded by homogeneous cytoplasm. The model is used to represent the microstructure of healthy mouse liver and an experimental liver metastasis. Normal and cancerous tissue specimens stained with DAPI and H&E are digitized at 20 \times magnification and analyzed to specify values of the model parameters. The spatial organization of cells is controlled in the model by a Gibbs-Markov point process whose parameters are tuned to maximize the similarity of experimental and simulated tissue microstructure, which is characterized using three descriptors of nuclear spatial arrangement adopted from materials science. The model can accurately reproduce the

microstructure of the relatively homogeneous healthy liver and the average cell clustering observed in the experimental metastasis, but it is less effective at reproducing the spatial heterogeneity of the experimental metastasis. The tissue microstructural properties included in the model are hypothesized to be significant determinants of ultrasound scattering in the high-frequency band.

5.1.3 Chapter 4: Three-dimensional computational modeling of high-frequency ultrasound imaging of a mouse liver metastasis model

The 3-D ultrasound simulator is used to synthesize B-mode images of simulated healthy and tumour tissues configured with the tissue model to match the microstructure of either health mouse liver or an experimental mouse liver metastasis. In these simulations, tissue microstructure is treated as a population of spherical nuclei surrounded by homogeneous cytoplasm. The first-order speckle statistics of the simulated images are compared with matching experimental images. The simulations show good matching between the first-order speckle statistics of the images synthesized for the simulated healthy tissue and experimental images of healthy murine liver. Furthermore, good matching is achieved between the first-order speckle statistics of the simulated tumour and experimental images of the corresponding liver metastasis when nucleus sound speed and mass density values are used that are different from the values assumed for healthy tissue. These preliminary results suggest that variations in the first-order speckle statistics between healthy and cancerous tissue are related to changes in tissue acoustic and microstructural properties.

5.2 Future work

The preliminary scattering results reported in chapter 4 characterize the first-order speckle statistics of the B-mode images synthesized for the simulated healthy and tumour tissues using the 3-D ultrasound simulator. The analyses can be extended to include comparison between the spatial distribution of the gray level values in the simulated B-mode images and the matching experimental images. The second-order analyses can be performed using a co-occurrence matrix [1] that can be computed for a B-mode image at predefined axial and lateral offsets, ρ and ς , respectively, such that the element in its i^{th} row and j^{th} column characterizes the joint probability of occurrence of gray levels i and j at two different pixels separated by axial spacing, ρ , and lateral spacing, ς , where the values of i and j are between 0 and 255. Therefore, the co-occurrence matrix is a discrete function analogous to the autocorrelation function [2] used in ultrasound signal processing. Co-occurrence matrices with various offsets can be computed for the images synthesized for each simulated tissue, and then the matrices can be analyzed to extract second-order features. The features of each simulated tissue can be compared with corresponding features computed for B-mode images of the matching experimental tissue specimen.

The high-frequency ultrasound scattering simulations presented here can be extended to use spectral analysis [3] to compare the radio-frequency (RF) signals acquired using the 3-D ultrasound simulator for the simulated healthy and tumour tissues with matching experimental RF signals. Such a comparison is crucial in view of the ability of high-frequency ultrasound scanners to provide quantitative estimates of tissue microanatomy based on spectral analysis of backscattered ultrasound signals [4, 5] to complement conventional B-mode images.

The 3-D ultrasound simulator computes linear acoustic propagation in an inhomogeneous fluid medium, and hence it does not incorporate nonlinear and shear propagations. Linear propagation is a valid approximation for imaging studies because the

amplitude of the waves transmitted by ultrasound scanners is relatively small. Ultrasound shear propagation in fluid-like soft tissue at mega-Hertz frequencies is highly attenuated and therefore can be neglected. However, some studies suggest that substantial elastic scattering of high-frequency ultrasound can occur in single cells [6] and tissue microanatomy [7]. Extensions of the mathematical formulation of the k -space method as suggested in [8] to include nonlinear and shear propagation can enable the use of the ultrasound simulator to perform scattering simulations that include elastic properties of tissue microanatomy and support applications in which nonlinear propagation is crucial, such as tissue harmonic imaging and contrast-enhanced imaging.

The ultrasound simulator and the stochastic tissue model can be used to study the effect on high-frequency ultrasound backscattering of varying individual microstructural properties. Such studies can be performed by computing ultrasound scattering in simulated tissues produced by varying the features under investigation and setting the other structural properties to match a particular tissue type. In addition, such studies could involve adding more cellular- and tissue-scale features to the cell nuclei, cytoplasm, and extracellular compartments included in the present tissue model. Such extensions would enable investigation of the contributions of cellular-scale features such as the cytoskeleton [9] by assigning different acoustic properties to the cytoplasm and extracellular compartments. Tissue-scale features such as blood vessels, liver lobules, and the acellular necrotic regions observed in the B16F1 experimental metastases could be added by including geometrically defined structures in the tissue model (e.g., treating blood vessels as a branching network of hollow cylinders). The high heterogeneity of the experimental metastasis could be incorporated by using the present tissue model as a component of a high-order stochastic process modeling the heterogeneity. These modifications should also enable the tissue model to mimic tumour types other than the experimental liver metastasis studied here.

The above discussion has focused on the applicability of the ultrasound simulator

and the tissue model to study scattering in the high-frequency (20-60 MHz) range. The present software could also be used as the basis for simulations at lower ultrasound frequencies. Simulations at acoustic microscopy frequencies > 100 MHz may require the inclusion of additional subcellular detail in the tissue model.

If the suggested extensions of the tissue model and the ultrasound simulator are fully implemented, the simulation software can be used to propose metrics based on high-frequency ultrasound backscattering to characterize tumour growth. Histology slides obtained from tumours at different stages of progression would be analyzed to determine their microstructural properties, and the tissue model would be separately configured to represent the microstructure of each tumour. The acoustic properties of each tumour would be estimated by using the ultrasound simulator to compute high-frequency ultrasound scattering in the simulated tumour with various combinations of acoustic properties of tissue microanatomy, and selecting the combination that maximizes the matching between the simulated ultrasound backscattered signals and corresponding experimental ultrasound signals. The simulated ultrasound backscattered signals computed using the optimized acoustic properties of each simulated tumour and matching experimental ultrasound signals would be analyzed to determine characteristics of high-frequency ultrasound backscattering that are sensitive to specific variations in tissue acoustic and microstructural properties that accompany tumour growth. The same approach can be applied to propose high-frequency ultrasound metrics to characterize anti-cancer treatment response and biological processes related to cancer such as invasion and apoptosis.

5.3 Closing

The parallel 3-D ultrasound simulator and the stochastic tissue model provide a computational framework to study high-frequency ultrasound scattering in tissue. Preliminary ultrasound scattering simulations reported in this thesis demonstrate that

the software can be used to relate the first-order speckle statistics of B-mode images of healthy and cancerous mouse liver to tissue acoustic and microstructural properties. Extensions of the software as described above could enable better understanding of the relationships between tissue microanatomy and characteristics of high-frequency ultrasound backscattering.

References

- [1] R. M. Haralick, K. Shanmugam, and I. Dinstein, "Textural features for image classification," *IEEE Trans. Syst. Man and Cybern.*, vol. 3, no. 6, pp. 610–21, 1973.
- [2] R. F. Wagner, M. F. Insana, and D. G. Brown, "Statistical properties of radio-frequency and envelope-detected signals with applications to medical ultrasound," *J. Opt. Soc. Am. A*, vol. 4, no. 5, pp. 910–22, 1987.
- [3] F. L. Lizzi, M. Ostromogilsky, E. J. Feleppa, M. C. Rorke, and M. M. Yaremko, "Relationship of ultrasonic spectral parameters to features of tissue microstructure," *IEEE Trans. Ultrason. Ferroelectr. Freq. Control*, vol. 34, pp. 319–329, 1987.
- [4] M. L. Oelze, W. D. O'Brien Jr, J. P. Blue, and J. F. Zachary, "Differentiation and characterization of rat mammary fibroadenomas and 4T1 mouse carcinomas using quantitative ultrasound imaging," *IEEE Trans. Med. Imaging*, vol. 23, pp. 764–71, 2004.
- [5] M. C. Kolios, G. J. Czarnota, M. Lee, J. W. Hunt, and M. D. Sherar, "Ultrasonic spectral parameter characterization of apoptosis," *Ultrasound Med. Biol.*, vol. 28, pp. 589–97, 2002.
- [6] R. E. Baddour and M. C. Kolios, "The fluid and elastic nature of nucleated cells: implications from the cellular backscatter response," *J. Acoust. Soc. Am.*, vol. 121, pp. EL16–22, 2007.
- [7] T. E. Doyle, K. H. Warnick, and B. L. Carruth, "Histology-based simulations for the ultrasonic detection of microscopic cancer in vivo," *J. Acoust. Soc. Am.*, vol. 122, pp. EL210–6, 2007.

- [8] T. D. Mast, L. P. Souriau, D.-L. Liu, M. Tabei, A. I. Nachman, and R. C. Waag, “A k -space method for large-scale models of wave propagation in tissue,” *IEEE Trans. Ultrason. Ferroelectr. Freq. Control*, vol. 48, no. 2, pp. 341–54, 2001.
- [9] M. L. Oelze and W. D. O’Brien Jr, “Application of three scattering models to characterization of solid tumors in mice,” *Ultrason. Imaging*, vol. 28, no. 2, pp. 83–96, 2006.

Appendix A

Permissions to Reproduce Published Work

Permissions/IOPP
Sent by: Jill Membrey
06/08/2009 14:36

To
cc
bcc
Subject Re: Fw: Including the paper (PMB/304775/PAP/220999) in my thesis

Johnathan Keen/Journals/IOPP
--- Forwarded by Johnathan Keen/Journals/IOPP on 05/08/2009 17:03 ---



"Mohammad Daoud"
04/08/2009 18:40

To
cc
Subject Including the paper (PMB/304775/PAP/220999) in my thesis

Dear Editor,

I am planning to use the paper entitled "Distributed three-dimensional simulation of B-mode ultrasound imaging using a first-order k-space method" (Article ID: PMB/304775/PAP/220999) that is accepted for publication in Physics in Medicine and Biology (PMB) as a chapter of my PhD thesis. Since the copyright of the paper has been transferred to PMB, I am wondering if you can send me an email stating that I can include the paper in my thesis.

Thank you,
Mohammad Daoud

--
Mohammad Daoud, M.A.Sc.
PhD Candidate,
Electrical and computer Eng. Dept.
The University of Western Ontario
Imaging Research Laboratories
Robarts Research Institute
100 Perth Drive, P.O. Box 5015
London, On, Canada N6A 5K8
Ph.:

PERMISSION TO REPRODUCE AS REQUESTED
IS GIVEN PROVIDED THAT:

- ~~(a) the consent of the author(s) is obtained~~
(b) the source of the material including author/editor,
title, date and publisher is acknowledged.*

IOP Publishing Ltd
Dirac House
Temple Back
BRISTOL
BS1 6BE

6/8/09
Date

.....
Rights & Permissions

* Please include the IOP Copyright line, mention the journal's homepage at:

www.iop.org/journals/pmb

and provide a link back to the article's abstract on our website from the electronic version of your thesis (if applicable).

Thank you.

Subject: Re: Including the manuscript (TBME-00192-2009.R1) in my thesis
From:
Date: Tue, August 4, 2009 3:13 pm
To:
Cc:
Priority: Normal
Options: View Full Header | View Printable Version | View as HTML

Dear Mohammad Daoud :

We are happy to grant you this permission to reprint this IEEE copyrighted paper in your thesis and, if you wish, to have it placed on your university's website. We have only two requirements that must be satisfied before we can consider this permission final:

(1) The following copyright/credit notice must appear prominently on the first page of the reprinted paper, with the appropriate details filled in: © [year] IEEE. Reprinted, with permission, from [IEEE publication title, paper title, and author names]

(2) Additionally, if your thesis is to appear on the university's website, the following message should be displayed at the beginning of the credits or in an appropriate and prominent place on the website: This material is posted here with permission of the IEEE. Such permission of the IEEE does not in any way imply IEEE endorsement of any of the [university's name]'s products or services. Internal or personal use of this material is permitted. However, permission to reprint/republish this material for advertising or promotional purposes or for creating new collective works for resale or redistribution must be obtained from the IEEE by writing to pubs-permissions@ieee.org. By choosing to view this material, you agree to all provisions of the copyright laws protecting it.

If applicable, University Microfilms, Inc. or ProQuest may supply single copies of the dissertation.

To complete the permission process, could you please send this email back with the name of your university?

Thank you.

Sincerely,

Jacqueline Hansson
 IEEE Intellectual Property Rights Coordinator
 IEEE Intellectual Property Rights Office
 445 Hoes Lane
 Piscataway, NJ 08855-1331 USA
 +1
 +1
 e-mail:
 IEEE Fostering technological innovation and excellence for the benefit of humanity

From: "Mohammad Daoud"
 To:
 Date: 08/04/09 02:01 PM
 Subject: Including the manuscript (TBME-00192-2009.R1) in my thesis

Dear Mr. Henson,

I am planning to use the paper entitled "Stochastic Modeling of Normal and Tumor Tissue Microstructure for High-Frequency Ultrasound Imaging Simulations" (manuscript ID: TBME-00192-2009.R1) by M. I. Daoud and J. C. Lacefield that is accepted for publication in IEEE TBME as a chapter of my PhD thesis.

Since the copyright of the paper has been transferred to IEEE TBME, I am wondering if you can send me an email stating that I can include the paper in my thesis.

Thank you,
Mohammad I. Daoud

--
Mohammad Daoud, M.A.Sc.
PhD Candidate,
Electrical and computer Eng. Dept.
The University of Western Ontario
Imaging Research Laboratories
Robarts Research Institute
100 Perth Drive, P.O. Box 5015
London, On, Canada N6A 5K8
Ph.:

Vita

NAME Mohammad Ibrahim Daoud

PLACE OF BIRTH

DATE OF BIRTH

EDUCATION

PhD Candidate 2005 – 2009

*Department of Electrical and Computer Engineering
The University of Western Ontario, London, ON, Canada*

Advisor: Dr. James C. Lacefield

Thesis: Development and validation of parallel three-dimensional computational models of ultrasound propagation and tissue microstructure for preclinical cancer imaging

Master of Applied Science 2003 – 2005

*Department of Electrical and Computer Engineering
Concordia University, Montreal, QC, Canada*

Advisor: Dr. Nawwaf Kharma

Thesis: A hybrid heuristic-genetic scheduling algorithm for task scheduling on heterogeneous computing systems

Bachelor of Applied Science 1996 – 2001

*Department of Electrical Engineering
An-Najah National University, Nablus, Palestine*

Advisor: Dr. Raed Al-Qadi

Graduation Project: A computer controlled robot arm

FELLOWSHIPS AND AWARDS

Postgraduate Scholarship-Doctorate, Natural Sciences and Engineering Research Council of Canada (NSERC), 2007–2009 (CND\$21,000/yr).

Outstanding Presentation in Graduate Symposium 2007, Department of Electrical and Computer Engineering, The University of Western Ontario, London, ON, Canada, 2007.

Ontario Graduate Scholarship (OGS)-declined, 2007–2008 (CND\$15,000/yr).

Strategic Training Program in Cancer Research and Technology Transfer, Canadian Institute of Health Research (CIHR) and The University of Western Ontario, 2006–2008 (CND\$23,600/yr).

Western Engineering Scholarship, The University of Western Ontario, 2005–2009, (CND\$8,500 for 2005–2006, CND\$4,500 for 2006–2007, CND\$9,685 for 2007–2008, CND\$9,906 for 2008–2009).

Graduate Studies Scholarship, Hani Qaddumi Scholarship Foundation, Jordan, 2003–2005, (CND\$20,000/yr).

First Prize, Graduation Project Competition, Department of Electrical Engineering, An-Najah National University, Palestine, 2001.

Tuition Scholarship, An-Najah University, Palestine, 1997–2001, (US\$500/yr).

RESEARCH EXPERIENCE

Graduate Student – Doctorate Aug. 2005 – Present
Imaging Research Laboratories
Robarts Research Institute, London, ON, Canada

Programmer Analyst Aug. 2004 – May 2005
SoftSim Technologies Inc., Longueuil, QC, Canada

Graduate Student – Master of Applied Science Jan. 2003 – Jan. 2005
Department of Electrical and Computer Engineering
Concordia University, Montreal, QC, Canada

TEACHING AND PROFESSIONAL EXPERIENCE

Teaching Assistant – Programming Fundamentals Jan. 2009 – Apr. 2009
Department of Electrical and Computer Engineering Sep. 2007 – Dec. 2007
The University of Western Ontario, London, ON, Canada Sep. 2006 – Dec. 2006
 Sep. 2005 – Dec. 2005

Teaching Assistant – Programming Methodology Jan. 2004 – Apr. 2004
Department of Electrical and Computer Engineering
Concordia University, Montreal, QC, Canada

Cisco Certified Network Associate Instructor Sep. 2001 – Mar. 2002
Cisco Networking Academy
An-Najah National University, Nablus, Palestine

Network Engineer Mar. 2002 – Jan. 2003
Palestine Telecommunications Co., Nablus, Palestine

JOURNAL REVIEWING

Referee, IEEE Transactions on Computers, 2008 – Present.

Referee, Journal of Parallel and Distributed Computing, 2006 – Present.

PROFESSIONAL SOCIETY MEMBERSHIPS

Student Member, Institute of Electrical and Electronics Engineers (IEEE), 2004 – Present.

Student Member, IEEE Engineering in Medicine and Biology Society, 2009 – Present.

Student Member, IEEE Ultrasonics, Ferroelectrics, and Frequency Control Society, 2006 – Present.

Member, IEEE Engineering in Medicine and Biology Society Student Chapter, The University of Western Ontario, 2006 – Present.

Student Member, International Society for Optical Engineering (SPIE), 2009 – Present.

EXTRACURRICULAR ACTIVITIES

Judge, 39th Annual London District Science & Technology Fair, London, ON, Canada, 2009.

External Communications Coordinator, IEEE Engineering in Medicine and Biology Society (EMBS) Student Chapter, The University of Western Ontario, London, ON, Canada, 2006 – Present.

Member of the Social Committee, Network of Imaging Students, Robarts Research Institute, London, ON, Canada, 2006 – Present.

Website Administrator, Network of Imaging Students, Robarts Research Institute, London, ON, Canada, 2006 – Present.

Website Administrator, Second Annual Canadian Student Conference on Biomedical Computing (CSCBC 2007), The University of Western Ontario, London, ON, Canada, 2007.

PUBLICATIONS AND CONTRIBUTIONS

Refereed Journal Papers

Published and Accepted:

[1] **M. I. Daoud** and J. C. Lacefield, “Stochastic modeling of normal and tumor tissue microstructure for high-frequency ultrasound imaging simulations,” *IEEE Trans.*

Biomed. Eng., In Press.

[2] **M. I. Daoud** and J. C. Lacefield, “Distributed three-dimensional simulation of B-mode ultrasound imaging using a first-order k -space method,” *Phys. Med. Biol.*, In Press.

[3] J. C. Tillett, **M. I. Daoud**, J. C. Lacefield, and R. C. Waag, “A k -space method for acoustic propagation using coupled first-order equations in three dimensions,” *J. Acoust. Soc. Am.*, In Press.

[4] **M. I. Daoud** and N. Kharm, “A high performance algorithm for static task scheduling in heterogeneous distributed computing systems,” *J. Parallel Distrib. Comput.*, vol. 68(4), pp. 399–409, 2008.

Submitted:

[5] Y.-T. Shen, **M. I. Daoud**, and J. C. Lacefield, “Computational models of distributed aberration in ultrasound breast imaging,” *IEEE Trans. Ultrason. Ferroelectr. Freq. Control*, submitted Oct. 2008.

[6] **M. I. Daoud** and N. Kharm, “A hybrid heuristic-genetic algorithm for task scheduling in heterogeneous processor networks,” *Applied Soft Computing*, submitted Apr. 2008.

Refereed Conference Papers

[1] **M. I. Daoud** and J. C. Lacefield, “Stochastic modeling of tissue microstructure for high-frequency ultrasound imaging simulations,” SPIE Medical Imaging 2009, *Proc. SPIE*, vol. 7262, 72620P, Lake Buena Vista, FL, USA, Feb. 7–12, 2009 (Podium Presentation).

[2] **M. I. Daoud** and J. C. Lacefield, “Efficient three-dimensional simulation of ultrasound imaging using a parallel k -space method,” 31st Canadian Medical and Biological Engineering Conference (CMBEC31), Montreal, QC, Canada, Jun. 11–13, 2008 (Four Page Paper, Podium Presentation).

[3] **M. I. Daoud** and J. C. Lacefield, “Parallel three-dimensional simulation of ultrasound imaging,” 22nd International Symposium on High Performance Computing Systems and Applications (HPCS 2008), *Proc. 22nd Intl. Symp. High Perform. Comp. Sys. Appl.*, pp. 146–152, Quebec City, QC, Canada, Jun. 9–11, 2008 (Podium Presentation).

[4] **M. I. Daoud**, Y.-T. Shen, and J. C. Lacefield, “A scalable parallel implementation of a k -space method for large-scale ultrasound imaging simulations,” 2006 IEEE International Ultrasonics Symposium, *Proc. 2006 IEEE Intl. Ultrason. Symp.*, pp. 2194–2197, Vancouver, BC, Canada, Oct. 3–6, 2006 (Poster Presentation).

- [5] **M. I. Daoud** and N. Kharm, “An efficient genetic algorithm for task scheduling in heterogeneous distributed computing systems,” 2006 IEEE Congress on Evolutionary Computation (CEC 2006), *Proc. 2006 IEEE Cong. Evol. Comp.*, pp. 3258–3265, Vancouver, BC, Canada, Jul. 16–21, 2006 (Podium Presentation).
- [6] **M. I. Daoud** and N. Kharm, “Efficient compile-time task scheduling for heterogeneous distributed computing systems,” 12th International Conference on Parallel and Distributed Systems (ICPADS), *Proc. 12th Intl. Conf. Para. Dist. Sys.*, vol. 1, pp. 11–22, Minneapolis, MN, USA, Jul. 12–15, 2006 (Podium Presentation).
- [7] **M. Daoud** and N. Kharm, “GATS 1.0: a novel GA-based scheduling algorithm for task scheduling on heterogeneous processor nets,” 2005 Genetic and Evolutionary Computation Conference (GECCO 2005), *Proc. 2005 Gene. Evol. Comp. Conf.*, vol. 2, pp. 2209–2210, Washington, DC, USA, Jun. 25–29, 2005 (Poster Presentation).
- [8] **M. Daoud**, N. Kharm, A. Haidar, and J. Popoola, “Ayo, the Awari player, or how better representation trumps deeper search,” 2004 IEEE Congress on Evolutionary Computation (CEC 2004), *Proc. 2004 IEEE Cong. Evol. Comp.*, vol. 1, pp. 1001–1006, Portland, OR, USA, Jun. 19–23, 2004 (Podium Presentation).

Refereed Conference Abstracts

- [1] J. C. Lacefield, **M. I. Daoud**, S. Z. Pinter, L. A. Wirtzfeld, and A. Fenster “Tools for planning and performing longitudinal cancer studies in mice using high-frequency ultrasound,” 34th International Symposium on Ultrasonic Imaging and Tissue Characterization, *Ultrason. Imaging*, vol. 31, pp. 74, Arlington, VA, USA, Jun. 10–12, 2009 (**Invited Podium Presentation**).
- [2] **M. I. Daoud** and J. C. Lacefield, “Stochastic modeling of murine liver microanatomy for high-frequency ultrasound imaging simulations,” 6th International Conference on Ultrasonic Biomedical Microscanning, Malibu, CA, USA, Sep. 23–26, 2008 (Podium Presentation).

Selected Seminar, Symposium, and Workshop Presentations

- [1] **M. I. Daoud** and J. C. Lacefield, “Three-dimensional computer simulations to analyze high-frequency ultrasound B-mode images of preclinical tumour models,” London Imaging Discovery Forum (LID), London Convention Centre, London, ON, Canada, Jun. 5, 2008 (Poster Presentation).
- [2] **M. I. Daoud**, “Distributed three-dimensional simulation of B-mode ultrasound imaging,” 2008 Graduate Symposium, Department of Electrical and Computer En-

gineering, The University of Western Ontario, London, ON, Canada, May 28–29, 2008 (Podium Presentation).

[3] **M. I. Daoud** and J. C. Lacefield, “Three-dimensional modeling of ultrasound imaging,” Robarts Research Day, Robarts Research Institute, London, ON, Canada, Mar. 27, 2008 (Poster Presentation).

[4] **M. I. Daoud** and J. C. Lacefield, “Three-dimensional computational modeling of preclinical ultrasound cancer imaging,” Dept. of Oncology Research & Education Day, The Schulich School of Medicine & Dentistry, The University of Western Ontario, London, ON, Canada, Jun. 22, 2007 (Poster Presentation).

[5] **M. I. Daoud** and J. C. Lacefield, “Enhancing tumour evaluation in preclinical cancer models using high-frequency ultrasound imaging,” London Imaging Discovery Forum (LID), London Convention Centre, London, ON, Canada, Jun. 16, 2007 (Poster Presentation).

[6] **M. I. Daoud**, Y.-T. Shen, and J. C. Lacefield, “Parallel implementation of a k -space method for large-scale ultrasound imaging simulations,” Second Annual Canadian Student Conference on Biomedical Computing, London, ON, Canada, Mar. 16–18, 2007 (Poster Presentation).